DIPLOMARBEIT

Advanced dosimetry near metal implants using radiochromic films

zur Erlangung des akademischen Grades

Diplom-Ingenieurin

im Rahmen des Studiums

Biomedical Engineering

vorgelegt von

Valentina Francesca Bauer, BSc

Matr. No.: 01426213

unter Anleitung von
Univ.Prof. Dipl.-Ing. Dr.techn. Dietmar Georg
Dipl.-Ing. Wolfgang Lechner, PhD

ausgeführt am
Atominstitut der Fakultät für Physik
Technische Universität Wien

in Zusammenarbeit mit der
Universitätsklinik für Radioonkologie
Medizinische Universität Wien

Wien, 10. Februar 2025

Unterschrift Student*in Unterschrift Betreuer*in

Acknowledgements

I would like to thank Univ.Prof. Dipl.-Ing. Dr.techn. Dietmar Georg for giving me the opportunity to conduct my diploma thesis at the Department of Radiation Oncology, Medical University of Vienna. Not only did he supervise my thesis, but he also took my strengths and qualities into account and thus enabled me to find a fascinating project within the field of my interest, which is something I am very grateful for.

Furthermore, I would like to thank Dipl.-Ing. Wolfgang Lechner, PhD for providing me guidance and support throughout my entire work and always sharing his insights and wisdom whenever needed. I would also like to express my gratitude for Priv.-Doz. Mag. Peter Kuess, PhD who took part in the proton beam experiments and shared his ideas in its evaluation process.

While conducting my diploma thesis I was twice given the chance to present my work as part of a doctoral seminar, where doctorate students and professors were present. In the discussions that followed I received a lot of valuable input as well as interesting questions that I could then implement to further enhance the quality of this thesis. Therefore, I would like to thank all the people who were present and engaged in the conversations.

I would also like to thank my best friend Isabella, who suffered alongside me with the writing process of her own diploma thesis, which helped make the entire process more fun. Many thanks also go to my boyfriend Stephan who not only supports me unconditionally in the pursuit of my dreams but also fuels me with homemade dinners at the end of each writing day and many motivation cuddles together with our shared plush toys Berta, Uterich, Nori, Chanuki and Tenzo. Lastly, I would like to thank my family who helped me financially throughout my work and thus made it possible for me to put my focus and energy into this thesis.

Abstract

Purpose: Patients receiving radiation therapy often have metal implants in or near target volumes which increase the overall uncertainty in the radiotherapy process through interference with the applied dose calculation algorithms in the vicinity of the implant. Hence, this diploma thesis aimed to analyse edge effects caused by metal implants when irradiated with photon and proton beams using radiochromic films as well as to calibrate a new film scanner for enhanced film dosimetry measurements in order to improve future radiotherapy treatment planning in terms of accuracy near metal implants.

Methods: For the calibration procedure, 4×4 cm^2 GafChromic EBT3 films were irradiated with monitor units (MU) 0, 100, 200, 300 and 400 corresponding to 0, 1, 2, 3 and 4 Gy. Subsequently, they were scanned one by one in order to calculate a calibration curve as well as placed in equal distances along the scanner to assess the scanner inhomogeneity. Photon beam experiments took place at the Department of Radiation Oncology, Medical University of Vienna/University Hospital AKH Vienna. The dose distribution measurements with the metal phantom were conducted by irradiating 5.9×5.9 cm^2 GafChromic EBT3 films at 15° table angle using photon energies 6 MV, 6 MV flattening-filter free (FFF), 10 MV and 10 MV FFF and evaluated using the newly calibrated scanner. Furthermore, reference films were irradiated for the respective photon energies except for 6 MV to test the thickness of the active layer of different film sheets within one lot (manufacturer identification number). The equivalent proton beam experiments took place at MedAustron. Similarly, 5.9×5.9 cm^2 GafChromic EBT3 films were examined, but instead using a 20° table angle. Film evaluations were performed with the scanner provided at MedAustron. Dose verifications were executed in all dose distribution measurements except photon beam energy 10 MV FFF and the films were irradiated with doses of 2 Gy using three different treatment plans. The Hounsfield units (HU) plan used the original computed tomography (CT) numbers of the CT scan, the polystyrene plan assigned polystyrene density values for the phantom and the titanium plan was overwritten with the titanium density values of the metal screw as well as the polystyrene values of the phantom. Furthermore, two different phantom configurations, namely a metal screw insert and a polystyrene insert, were used. All films were scanned in portrait orientation and used the response from the red color channel. Film analysis was performed with VeriSoft (PTW

Dosimetry, Freiburg, Germany) and Python scripts. For meaningful comparison, the films were properly aligned with each other as well as the treatment plans using the pinholes on each film. Furthermore, the films and treatment plans were normalized, re-calibrated and a region of interest (ROI) was determined. At line dose profiles of interest, a mean and sample standard deviation were calculated from the line and its two neighboring lines as well as all the films irradiated with a specific treatment plan. The results were then compared with the treatment plans calculated with the clinical treatment planning system (TPS) RayStation (RaySearch, Stockholm, Sweden) as well as Monte Carlo (MC) simulations performed with the independent secondary dose calculation system SciMoCa (ScientificRT GmbH, Munich, Germany). Lastly, dose differences and a confidence interval (CI) of 95 % were determined for the analysis.

Results: The calibration curve and error analysis showed satisfactory results with a mean calibration error of 0.3 % and a standard deviation of 1.7 %. Examination of lateral scanner artefacts revealed discrepancies up to 13 % from the normalized pixel values when scanning films irradiated with 400 MUs in the lateral regions. Photon and proton beam experiments corresponded well with the RayStation and SciMoCa plans for polystyrene measurements, with dose differences generally contained within a 3 % margin. Photon beam experiments using HU-plans matched with MC simulations whereas comparisons with the RayStation plans exhibited dose differences up to approx. 13.6 % where the titanium screw and the tissue equivalent polystyrene material intersected. Meanwhile, Ti-plan simulations showed inaccuracies in the vicinity of the titanium screw for both plans with maximum dose differences around 13.4 % for the RayStation plans and even 25.3 % for the SciMoCa plans due to imprecise titanium screw density data. Regarding the proton beam experiments, increased variability was observed in line dose profiles for films irradiated under the HU- and Ti-plans, likely due to the fixed horizontal beamline and the lack of detailed geometrical data about the screw thread in the TPS. Overall, dose verification using an ionization chamber revealed dose differences ranging from 0.14 to 0.95 % post-output correction for photon beams, and from 0.3 to 1.0 % without such corrections for proton beams. Lastly, reference film measurements resulted in a 2.8 % standard deviation among radiochromic films within the same and across differing film sheets of the lot, as well as across different energy settings. Nonetheless, these variances were deemed negligible due to normalization applied to the line dose profiles.

Conclusions: The calibration of the new film scanner was successful - with the knowledge of the row scans a correction matrix can be calculated for future scanning processes. Both the results of the proton beam experiment as well as the photon beam experiment clearly show the influence of the metal screw. For the polystyrene measurements, both

the RayStation and SciMoCa plans show similarly good results. When the metal screw is present, MC simulations come much closer to the actual dose profile than the RayStation TPS. Therefore, MC can be a very useful tool in dose estimation.

Kurzzusammenfassung

Zielsetzung: Patient*innen, die eine Strahlentherapie erhalten, haben oftmals Metallimplantate in bzw. um das Zielvolumen, was die Gesamtunsicherheit im Strahlentherapieprozess durch Interferenzen mit den angewandten Dosisberechnungsalgorithmen nahe dem Implantat erhöht. Daher zielt diese Diplomarbeit darauf ab, Kanteneffekte unter Verwendung radiochromer Filme zu analysieren, die durch Metallimplantate bei Bestrahlung mit Photonen- und Protonenstrahlen verursacht werden, sowie einen neuen Filmscanner für verbesserte Filmdosimetriemessungen zu kalibrieren, um die zukünftige Strahlentherapieplanung hinsichtlich der Genauigkeit nahe Metallimplantaten zu verbessern.

Methoden: Für das Kalibrierungsverfahren wurden 4×4 cm^2 GafChromic EBT3-Filme mit MU 0, 100, 200, 300 und 400, welche 0, 1, 2, 3 und 4 Gy gleichgesetzt sind, bestrahlt. Anschließend wurden sie einzeln gescannt, um eine Kalibrierungskurve zu berechnen sowie in gleichen Abständen entlang der Scanneroberfläche platziert, um die Scanner-Inhomogenität zu ermitteln. Photonenstrahlexperimente fanden in der Universitätsklinik für Radioonkologie der Medizinischen Universität Wien/Universitätsklinikum AKH Wien statt. Die Dosisverteilungsmessungen am Metallphantom wurden mittels Bestrahlung von 5.9×5.9 cm^2 GafChromic EBT3-Filmen bei 15° Tischwinkel mit den Photonenenergien 6 MV, 6 MV FFF, 10 MV und 10 MV FFF durchgeführt und mit dem neu kalibrierten Scanner ausgewertet. Darüber hinaus wurden Referenzfilme mit den jeweiligen Photonenenergien (ausgenommen 6 MV) bestrahlt, um die Dicke der aktiven Schicht verschiedener Filmblätter innerhalb einer Lot (Hersteller-Identifikationsnummer) zu testen. Die entsprechenden Protonstrahlexperimente wurden bei MedAustron durchgeführt. In ähnlicher Weise wurden 5.9×5.9 cm^2 GafChromic EBT3-Filme untersucht, jedoch bei einem Tischwinkel von 20°. Die Filmauswertungen wurden mit dem von MedAustron bereitgestellten Scanner durchgeführt. Bei allen Dosisverteilungsmessungen, mit Ausnahme des Photonenstrahls bei 10 MV FFF, wurden Dosisverifikationen durchgeführt und die Filme wurden jeweils mit 2 Gy unter Verwendung von drei verschiedenen Bestrahlungsplänen bestrahlt. Der HU-Plan verwendete die ursprünglichen CT-Zahlen des CT-Scans, der Polystyrolplan wies Polystyroldichtewerte für das Phantom zu und der Titanplan wurde mit den Titandichtewerten der Metallschraube sowie den Polystyroldichtewerten des Phantoms überschrieben. Darüber hinaus wurden zwei verschiedene Phantomkonfigu-

rationen verwendet, nämlich ein Metallschraubeneinsatz und ein Polystyroleinsatz. Alle Filme wurden im Portrait-Modus gescannt und zur Auswertung wurde das Signal des roten Kanals verwendet. Die Filmanalyse wurde mit VeriSoft (PTW Dosimetry, Freiburg, Deutschland) und Python-Skripten durchgeführt. Für einen aussagekräftigen Vergleich wurden die Filme untereinander sowie mit den Isozentren der Bestrahlungspläne mithilfe der Pinlöcher auf jedem Film genauestens angeglichen. Darüber hinaus wurden die Filme und Bestrahlungspläne normiert, neu kalibriert und ein ROI bestimmt. Bei ausgewählten Liniendosisprofilen wurden der Mittelwert und die Probenstandardabweichung aus der gewählten Linie und ihren beiden Nachbarlinien sowie von allen mit einem bestimmten Bestrahlungsplan bestrahlten Filmen berechnet. Die Ergebnisse wurden anschließend mit den Bestrahlungsplänen verglichen, welche mithilfe des klinischen Bestrahlungsplanungssystems RayStation (RaySearch, Stockholm, Schweden) erstellt wurden, sowie auch mit MC Simulationen, die mit dem unabhängigen sekundären Dosisberechnungssystem SciMoCa (ScientificRT GmbH, München, Deutschland) durchgeführt wurden. Schließlich wurden Dosisdifferenzen und ein Konfidenzintervall von 95 % für die Analyse bestimmt.

Resultate: Die Kalibrierungskurve und die Fehleranalyse zeigten zufriedenstellende Ergebnisse mit einem mittleren Kalibrierungsfehler von 0,3 % und einer Standardabweichung von 1,7 %. Die Untersuchung lateraler Scannerartefakte ergab beim Scannen von Filmen, die zuvor mit 400 MUs bestrahlt wurden, im lateralen Scanbereich Abweichungen von den normierten Pixelwerten von bis zu 13 %. Photonen- und Protonenstrahlexperimente stimmten bei den Polystyrolmessungen gut mit den RayStation- und SciMoCa-Plänen überein, wobei die Dosisunterschiede im Allgemeinen innerhalb einer Spanne von 3 % blieben. Photonenstrahlexperimente unter Verwendung von HU-Plänen stimmten mit MC-Simulationen sehr gut überein, währenddessen im Vergleich mit den RayStation-Plänen starke Dosisunterschiede von bis zu etwa 13,6 % an der Grenzfläche zwischen der Titanschraube und dem gewebeäquivalenten Polystyrolmaterial festgestellt wurden. Unterdessen zeigten Ti-Plan-Simulationen Ungenauigkeiten in der Umgebung der Titanschraube für beide Bestrahlungsplanungssysteme mit maximalen Dosisunterschieden von etwa 13,4 % für die RayStation-Pläne, und sogar 25,3 % für die SciMoCa-Pläne aufgrund von ungenauen Titanschrauben-Dichteangaben. Bei den Protonenstrahlexperimenten wurde eine erhöhte Variabilität in Liniendosisprofilen für Filme, die mit HU- und Ti-Plänen bestrahlt wurden, festgestellt, was möglicherweise auf die feste horizontale Strahlführung und das Fehlen detaillierter geometrischer Daten über das Schraubengewinde im Bestrahlungsplanungssystem zurückzuführen ist. Insgesamt ergab die Dosisüberprüfung mithilfe einer Ionisationskammer Dosisunterschiede im Bereich von 0,14 bis 0,95 % nach der Output-Korrektur für Photonenstrahlen und von 0,3 bis 1,0 % ohne solche Korrekturen für Protonenstrahlen. Schließlich ergaben Referenzfilmmessungen eine Standardabwe-

ichung von 2,8 % für radiochrome Filme desselben Filmblattes, verschiedener Filmblätter sowie bei verschiedenen Energieeinstellungen. Die Unterschiede konnten jedoch vernachlässigt werden, da vor der Analyse eine Normierung der Liniendosisprofile durchgeführt wurde.

Schlussfolgerung: Die Kalibrierung des neuen Filmscanners war erfolgreich – mit der Information der Zeilenscans kann eine Korrekturmatrix für zukünftige Scanvorgänge berechnet werden. Sowohl die Ergebnisse des Protonenstrahlexperiments als auch jene des Photonenstrahlexperiments zeigen deutlich den Einfluss der Metallschraube. Für die Polystyrolmessungen zeigen sowohl die RayStation-Pläne also auch die SciMoCa-Pläne ähnlich gute Ergebnisse. Wenn sich die Metallschraube im Phantom befindet, kommen die MC Simulationen dem tatsächlichen Dosisprofil wesentlich näher als die RayStation-Bestrahlungsplanungssysteme. Daher kann MC ein sehr nützliches Hilfsmittel bei der Dosisabschätzung sein.

Contents

Abbreviations

3DCRT three-dimensional conformal radiation therapy

C/S convolution/superposition

CBCT cone-beam computed tomography

CC collapsed cone

CI confidence interval

CPE charged particle equilibrium

CSDA continuous slowing down approximation

CT computed tomography

DECT dual energy computed tomography

DPI dots per inch

EBRT external-beam radiotherapy

EM electromagnetic

FBP filtered back projection

FF flattening-filter

FFF flattening-filter free

HU Hounsfield units

IAEA International Atomic Energy Agency

IGRT image-guided radiotherapy

IMRT intensity-modulated radiation therapy

LET linear energy transfer

LINAC linear accelerator

MAR metal artifact reduction

MC Monte Carlo

MCS Multiple Coulomb scattering

MLC multileaf collimators

MU monitor units

NCR non-clinical research

OAR organs at risk

OD optical density

PTV planning target volume

PV pixel values

RBE relative biological effectiveness

RF radio frequency

ROI region of interest

SOBP spread-out Bragg peak

SSD source-to-surface distance

TP treatment planning

TPS treatment planning system

VM virtual monochromatic

VMAT volumetric modulated arc therapy

1 Introduction

1.1 Cancer worldwide

Cancer is the second leading cause of death [1] with almost 20 million new cases in 2022 and an estimate of up to 35 million new cases by the year of 2050 [2]. The ever-rising numbers lead to the assumption that cancer may replace cardiovascular diseases as the leading cause of death in most countries in the upcoming decades [3–5]. Bray et al. [2] summarizes the most common types of cancers for both sexes in 2022 to be lung cancer (12.4%), female breast cancer (11.6%), colorectum cancer (9.6%) and prostate cancer (7.3%). Amongst men the highest numbers of cancer deaths occured with lung cancer (22.7%) and liver cancer (9.6%), whereas mortality in women was mainly caused by breast cancer (15.4%) and lung cancer (13.6%) [2].

Cancer treatment is conventionally performed in form of surgery, radiotherapy and systemic therapy such as chemotherapy and immunotherapy [6] with radiotherapy being the applied treatment in about 50% of cancer patients [7, 8], either alone or in combination with other treatment options [9].

1.2 Radiotherapy

Radiotherapy is a highly precise and effective form of cancer treatment that has significantly evolved over the past century [10] and can be performed with either curative intent aiming at curing the patient of the disease or as palliative treatment helping the patient to relieve symptoms and improve the quality of life, depending on the anatomic staging of the cancer [8, 11]. In principle, radiotherapy uses ionizing radiation (see Section 1.2.1) to destroy or disable cancer cells while preserving the function of normal body cells within the area of treatment [9]. By following the principle of ALARA ("as low as reasonably achievable") the field of radiotherapy is subject to many guidelines and regulations [12], while also continuously pursuing improvement of increased local tumor control at reduced radiation toxicity through advances in computing, robotics, imaging, biology and omics as well as digital connectivity and clinical science [13].

Techniques in radiotherapy can generally be divided in external-beam radiotherapy (EBRT) and brachytherapy [14–16]. In brachytherapy sealed, radioactive sources are inserted in the patient and positioned in and around the tumor [16–19]. Commonly used low-dose-rate sources with half-lives between 16.96 to 74.17 days include iodine-125, palladium-10 and iridium-192 [17, 19, 20]. Here, the seeds remain in the patient after the procedure, whereas high-dose-rate sources are applied via a catheter and removed once the desired dose is administered [17, 19, 20]. While brachytherapy offers steep dose gradients and thus high local dose delivery, it is an invasive method and requires a high set of skills on the applicator side [17, 21]. Since EBRT is non-invasive it is the more frequently used treatment option in radiotherapy [16]. Abd et al. [22] describe how intensity-modulated radiation therapy (IMRT) has become the gold standard in EBRT as it grants the variation of beam intensity by changing the shape of the multileaf collimators (MLC) in the linear accelerator (LINAC) and thus allows for more precise dose delivery [22–24]. Another concept that can be incorporated in IMRT is volumetric modulated arc therapy (VMAT), which shortens the time of treatment by adapting the MLCs and dose rate while rotating the gantry of the LINAC [22, 25–27]. Common sources used in EBRT include photons (X-rays or γ-rays), electrons, protons or in some cases even neutrons or heavy ions [16]. Different beam sources require different setups which are going to be discussed in Sections 1.2.2, 1.2.3 and 1.2.6 for photon and proton beams. Moreover, there are further treatment planning (TP) options which will be explored in Section 1.5.

1.2.1 Ionizing radiation

The term "ionizing radiation" specifically denotes particles or X-rays that cause a neutral atom within a cell to become positively or negatively charged through their interaction [9, 28]. Damage from ionizing radiation occurs either directly or indirectly, with the latter being more prevalent in clinical radiotherapy [29]. In direct ionization, the energy is directly transferred to the DNA, whereas in indirect ionization, the ionizing radiation interacts with cellular water, leading to the formation of free radicals and resultant DNA damage [9]. While double-strand breaks are crucial, radiation can also significantly impact the cell cycle in terms of cell growth, cell senescence and cell death [29, 30].

1.2.2 Photon source

With the discovery by Willhelm Röntgen in 1895, X-rays soon became an integral part of the medical field for diagnostics and radiation treatment [31]. The photon energy determines the penetration depth of the beam and X-rays in the low energy range are typically produced by X-ray tubes [32]. In order to produce high-energy X-rays in the MV range, an accelerating waveguide is needed, requiring a more complex machinery

[31]. EBRT is most commonly applied using high-energy photons delivered by LINACs [33]. The principle of a LINAC is described by Falk [34] and Podgorsak [16]. At first, electrons are emitted from a cathode [34]. They then follow a straight trajectory in vacuum through a cylindrical waveguide where they are accelerated by non-conservative microwave radio frequency (RF) fields that create several identical low potential differences along the accelerating waveguide. These RF fields originate from magnetrons/klystrons and are produced in vacuum by the deceleration of electrons in retarding potentials. Their microwave frequency range can vary based on different bands but is mostly set to about 3,000 MHz in the S band [16]. After exiting the accelerating waveguide, the electrons enter a bending magnet which redirects the electron beam to hit the target, thus producing the X-ray photon beam that reaches the patient [34].

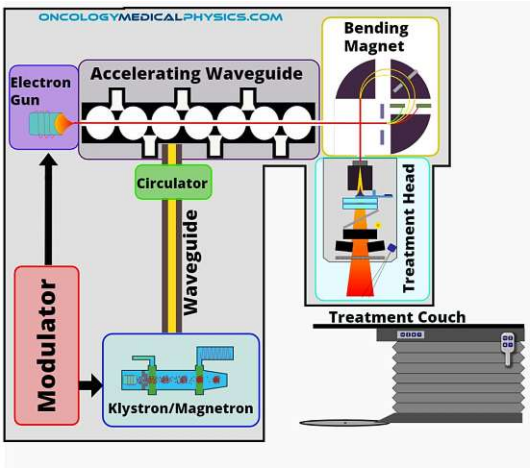

Fig. 1.1: Schematic of a LINAC typically used in clinical radiotherapy (left), with kind permission from Oncology Medical Physics LLC [35].

There are different types of LINACs in clinical operation with some only providing low energy X-rays while others can produce both X-rays and electrons in low and high energy ranges [16]. Clinically used photon beam energies typically range from 4 to 10 MV [34]. Furthermore, in clinical settings LINACs typically incorporate a cone-shaped flattening-filter (FF) within the beam path of the treatment head, creating a uniform dose distribution in the treated area of the patient [36–38]. The use of such filters originates from the historical development of TPSs which required flat dose profiles [38]. However, it is now understood that these FFs reduce dose rates [36–40], increase scattering within the treatment head [37, 38, 41–48] and contribute to higher out-of-field doses [38, 46, 49, 50]. Additionally, FFs cause increased energy variations with off-axis distances [37, 38] as well as discrepancies in the measured MUs when compared to FFF settings [38]. Advanced TPSs such as IMRT and stereotactic radiotherapy can benefit from specific characteristics of FFF beams and, consequently, modern LINACs have introduced FFF modes to enhance treatment effectiveness [38, 51–55].

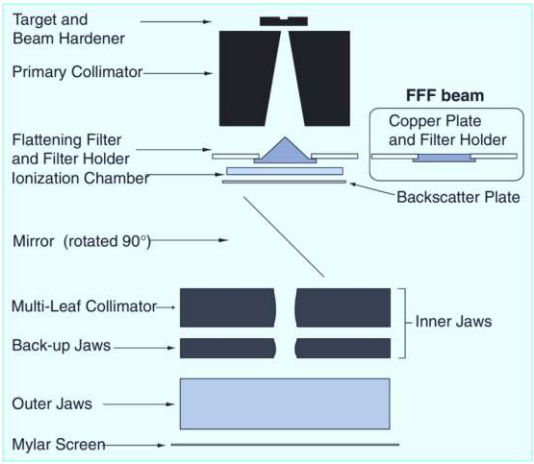

Fig. 1.2: Example of the treatment head components of a LINAC with the option of two modes: a FF mode and a FFF mode, adapted from [37].

1.2.3 Proton source

With the invention of the cyclotron by Lawrence in 1929 and the further development of the Harvard cyclotron by Wilson in 1946, proton therapy came into existence [14, 56–58]. The theory of a synchrocyclotron was independently presented by Veksler and McMillan in 1944 and 1945, respectively, but both the cyclotron and synchrocyclotron had energy limitations due to the required magnet size [59–61]. Hence, a more cost effective solution with a wider energy range was found in the synchrotron [59, 62]. In October 2022, 118 proton radiation therapy centers were operating around the world [63, 64].

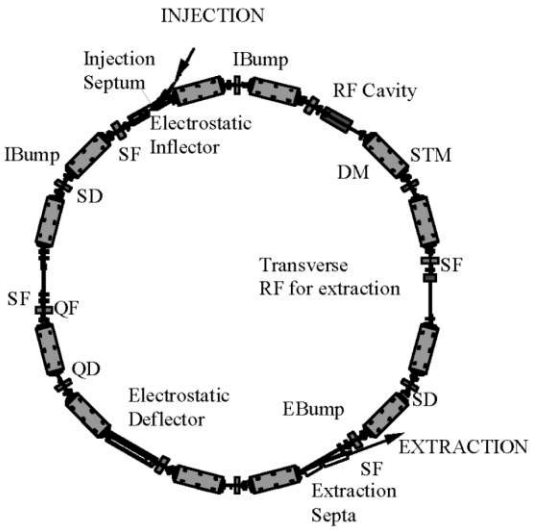

Fig. 1.3: Example schematic of a synchrotron using a dipole magnet (DM), a quadrupole magnet (QF/QD), a sextupole magnet (SF/SD), a steering magnet (STM) and incjection/extraction bump magnets (IBump/EBump). Taken from [65].

The principle of a synchrotron is based on Malouff and Trifiletti [59] and applied to light ions. Overall, a synchrotron is characterized by the synchronous variability of the magnetic with the proton energy as well as the synchronous variability of the electric field (RF) with the orbital frequency of the proton, which in turn depends on the proton energy and thus the magnetic field. A pulsed beam current enables the synchronicity between the electric and magnetic field. Furthermore, protons need to have an initial velocity and are thus pre-accelerated to a MeV range before being injected into the synchrotron. Inside the synchrotron, proton motions resemble a harmonic oscillator. In order to avoid any deviation from the path three types of magnets are used to focus and bend the proton beam: dipole magnets to bend the protons a certain angle, quadrupol magnets to focus the beam and sextupole magnets to refocus the protons which experienced an energy shift by the quadrupol magnets. Therefore, perturbation only occurs when a RF signal is introduced, which is used to extract the protons when desired [59].

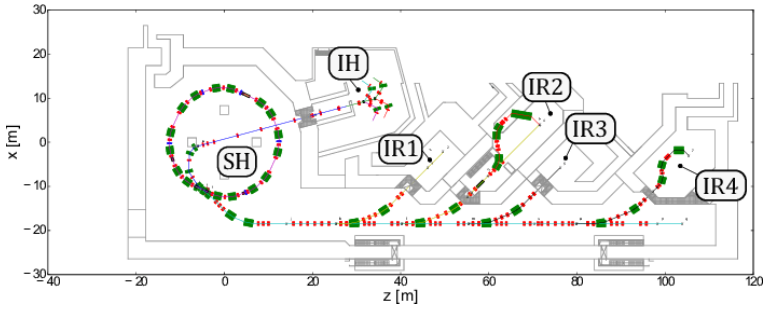

Fig. 1.4: Schematic of a proton therapy treatment facility using a synchrotron at the example of MedAustron with an injector hall (IH), a synchrotron hall (SH) and four irradiation rooms (IR1-IR4). Taken from [66].

In the context of proton therapy treatment facilities the role of the synchrotron can be described as previously outlined by Mohan and Grosshans [67] using MedAustron as an example [66, 68]. Here, the emitted ions (H_3^+ for protons) are pre-accelerated in a separate LINAC before passing a stripper foil and injecting the protons into the synchrotron [66]. The synchrotron then accelerates protons in batches (pulses) until the desired energy is reached [67]. Beam extraction is achieved by third-integer resonance excitation [66] and the use of a betatron core [66, 68]. The proton beam then travels along a beamline to the required irradiation room [66], where it passes a nozzle design that consists of beam monitors, an independent termination system, and further passive beam modifiers such as a range shifter and ripple filters [68].

1.2.4 Photon interactions with matter

When photons (X-rays or gamma rays) interact with matter it is classified as indirect ionization and this process lacks efficiency compared to electron ionization as photons are not electrically charged, thus allowing energy transfer only upon direct contact, which is infrequent given the small size of targets like orbital electrons and the nucleus compared to the atom's overall volume [69]. During the interaction the photon transfers (part of) its energy to the medium which leads to the attenuation, absorption, scattering or transmission of the photon [29]. In radiotherapy, there are three predominant forms of interaction between photons and matter: photoelectric effect, Compton scattering and pair production [16, 69]. Krieger [70] elaborates on each effect in detail in his book and will be the basis of this section.

Photoelectric effect

In the photoelectric effect, a photon collides with an electron from the inner K-, L- or M-shell of an atom, thereby transferring its entire energy to the electron and releasing it. The condition for the electron to leave the atom is that the photon energy is greater than the binding energy of the electron:

$$E_{kin} = E_\gamma - E_b(K, L, M, ...) > 0 \tag{1.1}$$

In the process, the photon gets absorbed and the remaining energy serves as the kinetic energy of the released electron. Photon absorption occurs with the highest probability when the energy of the photon coincides with the binding energy of the electron. A maximum in photon absorption is seen in the K-shell, also commonly referred to as K-edge. Around 80% of interactions take place with K-electrons.

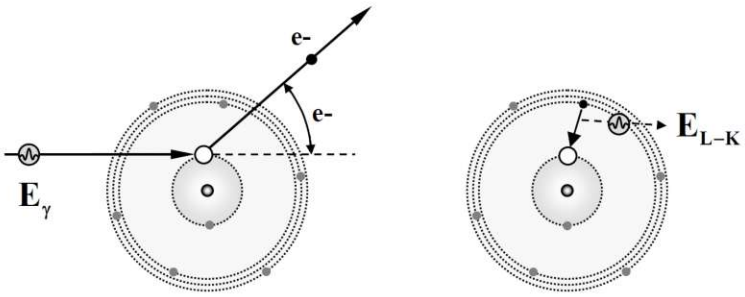

Fig. 1.5: Demonstration of the photoelectric effect causing the emission of a secondary electron (left) and further down a tertiary photon (right). Taken from [70].

Certain radiation protection measurements are mainly based on the photoelectric effect since the angle of the electron strongly depends on the energy of the absorbed photon. For low energies, most electrons are emitted perpendicular to the incoming photon beam, some even backward. Forward emission of the secondary electrons takes place in higher energy regions. Thus, the photoelectric effect plays an important role in diagnostics.

Following the secondary particles, further tertiary radiation is created as well. When an electron is freed, the hole is immediately filled by another electron from an outer shell, thereby releasing the energy difference in the form of a characteristic X-ray or, if another electron is ejected, an Auger electron.

Compton effect (also Compton scattering)

Compton scattering refers to an inelastic interaction between a photon and a weakly bound electron in the outer shell of an atom. Here, the photon transfers part of its energy and momentum to the electron, thus releasing it. Meanwhile, the photon is deflected.

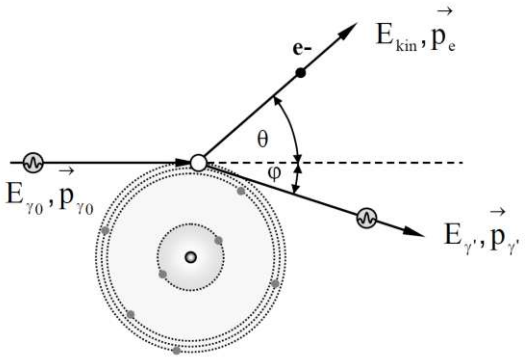

Fig. 1.6: Compton effect. Taken from [70].

In order to discuss the Compton effect mathematically, the concept of elastic collisions is used. From that the resting energy of the photon after collision can be derived and goes as follows:

$$E'_\gamma = \frac{E_\gamma}{1 + \frac{E_\gamma}{m_0 c^2}(1 - \cos\phi)} \tag{1.2}$$

This formula shows that the resulting energy of the scattered photon E'_γ depends on both the original photon energy E_γ and the scattering angle ϕ. This is influenced by the ratio of photon energy E_γ to resting energy of the electron $m_0 c^2$. In case of $E_\gamma \ll m_0 c^2$, the denominator gets close to 1 and E'_γ doesn't deviate too strongly from E_γ. In diagnostics, this is an important issue for radiation protection, since the scattered photon radiation is not much softer than the incoming photon beam. On the other hand, Compton electrons

are low in energy and thus only have a small range within the patient's body. Now for $E_\gamma \gg m_0c^2$, the factor containing the scattering angle gains much more importance, and as such the energy transferred to the Compton electron as well as its reach within the body leading to a dose-buildup effect strongly depends on the scattering angle of the photon. A maximum of the energy transfer from the photon to the secondary electron is reached when the photon backscatters ($\phi = 180°$) and the denominator becomes $1 + 2 \cdot \frac{E_\gamma}{m_0c^2}$. The energy distributions of Compton electrons are continuous with a sharp upper limit referred to as the Compton edge.

Pair production

Pair production describes the interaction of a photon with the strong Coulomb field of an atomic nucleus, from which the creation of electron-positron pairs can spontaneously take place. It can only occur, if the photon energy exceeds 1022 keV, since 511 keV equals the resting energy for each of the created particles. The photon is annihilated in the process and the remaining energy serves as kinetic energy split between the two particles, whereby the positron usually receives a larger portion due to being repulsed by the positively charged Coulomb field.

$$E_{kin} = E_\gamma - 2m_0c^2 = E_\gamma - 1022\,keV \tag{1.3}$$

The nucleus remains unchanged and only serves as the conservation of energy and momentum. Emission usually occurs in the original direction of the beam. Once the positron slows down due to interaction with the absorber material, it can recombine with another shell electron leading to annihilation radiation in the form of two photons being emitted at a 180° angle.

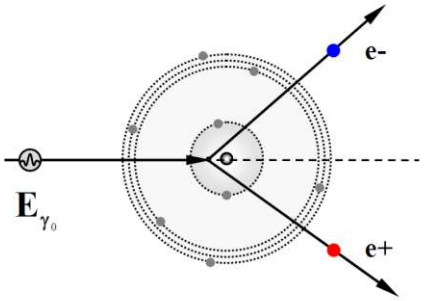

Fig. 1.7: Pair production showing the annihilation of a photon near the nucleus leading to electron-positron pair production. Adapted from [70].

Comparison of the interactions using the mass absorption coefficient

An effective method to compare the relevance of the three effects in clinical settings is given by the mass absorption coefficient $\frac{\mu}{\varrho}$, derived from the absorption coefficient μ and density ϱ. It represents the softening of photon beams through scattering and absorption. The mass absorption coefficient can graphically describe the predominant interaction(s) depending on the atomic number Z and the photon energy E_γ.

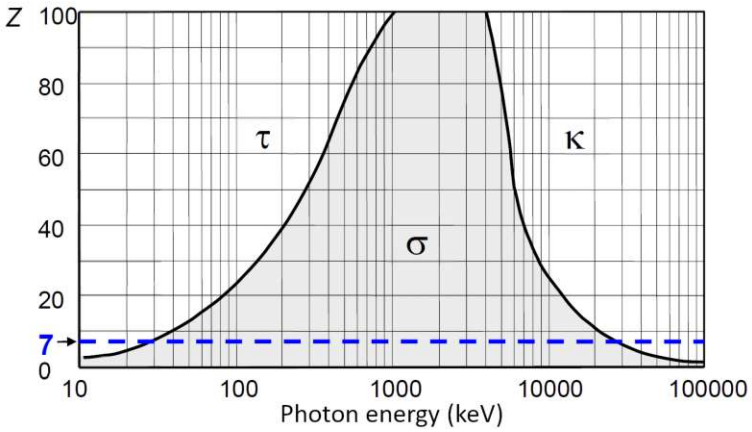

Fig. 1.8: Mass absorption coefficient of the photoelectric effect τ, Compton effect σ and pair production κ in dependence of atomic number Z and photon energy E_γ. $Z \cong 7$ represents water/tissue equivalent phantoms. Translated from [70].

For heavy elements in lower photon energy ranges (up to 1 MeV), the photoelectric effect is the predominant effect. The Compton effect dominates large energy ranges and mostly small atomic numbers, making it the biggest contributor in human tissue. Meanwhile, pair production can only take place when photon energies exceed 1022 MeV in high atomic numbers. For lower atomic numbers, even higher energies are needed [70].

1.2.5 Proton interactions with matter

The interactions of protons with matter were thoroughly discussed by Gottschalk [71] and thus this section will be based on his work. Three major ways describe proton interactions with matter in the context of radiotherapy: multiple collisions of protons with atomic electrons leading to energy loss up to a standstill of the proton (stopping) or multiple collisions of the protons with the atomic nuclei causing either slight scattering (multiple Coulomb scattering) or at times strong scattering which can lead to higher doses away from the beam (hard scatters).

Stopping

The majority of interactions in proton therapy involve the proton stopping after several electromagnetic (EM) collisions with atomically bound electrons. One way to describe this process is the continuous slowing down approximation (CSDA) theory. In 3-300 MeV protons, the CSDA range can be described as

$$\varrho R(T_{initial}) = \int_{T_{initial}}^{T_{final}} \left(\frac{1}{\varrho}\frac{dT}{dx}\right)^{-1} dT = \int_{T_{initial}}^{T_{final}} \frac{dT}{S/\varrho(T)} \tag{1.4}$$

with the initial energy $T_{initial}$ when entering the material, the resulting energy T_{final} (> 0) after the energy loss and the mass stopping power S/ϱ which amounts to the loss of energy T per unit path length x divided by the density ϱ, given in g/cm^2. Typical proton ranges in water include [72]:

kinetic energy [MeV]	3	10	30	100	300
range in water [cm]	0.015	0.125	0.896	7.793	51.87

Tab. 1.1: Proton ranges in water for various energies.

Range straggling occurs when protons are nearing a standstill as various discrete and random energy transfers can contribute to their stopping. As a result, protons will come to rest at slightly different depths (see the spread-out Bragg peak (SOBP) in Fig. 1.9).

Multiple Coulomb scattering

Multiple Coulomb scattering (MCS) refers to EM interactions between protons and atomic nuclei (also atomic electrons in the case of low-Z materials) causing the protons to deflect in random directions. In analogy to stopping power in stopping, the differential approach to MCS is achieved through the scattering power, which is defined as

$$T_{xx}(z) \equiv d < \theta_x^2 > /dz \tag{1.5}$$

which is the rate of increase with z of the variance of the projected MCS angle. $T_{xx}(z)$ is not to be confused with kinetic energy and can entail different formulas. For example, when integrating the scattering power over z in a full slab, the angle defined by the Moliére/Fano/Hanson theory [73] using a Gaussian approximation has to be applied. For various target thicknesses, the scattering power has to be nonlocal, which can be achieved by e.g. a correction factor towards the Gaussian approximation. Scattering power depends on both the conditions present at z and the protons' initial momentum and velocity. This is because many protons undergo numerous collisions, leading to a statistical approach to MCS.

Hard scatters

Many reactions can result in hard scatters since they can occur through either EM or nuclear force, can be an interaction with the whole nucleus (coherent) or a part of it (incoherent), and can furthermore be divided into elastic (conservation of kinetic energy), inelastic (no kinetic energy conservation, recoil nuclide is excited and the same as the target) and nonelastic (recoil nuclide might be excited, but differs from the target) scatters. Hard scatters cause problems concerning the dose distribution of a pencil beam as they distribute the dose over large radii creating a so-called *nuclear halo* [74].

Here, the *core* is formed by the compact central region of the primary protons, whereas the *halo* includes the dose from charged secondaries surrounding the core. There is also the *aura* which refers to a very large region caused by neutral secondary particles. Each region comes with distinct characteristics, but the regions overlap with each other. Depending on the beam design, there might also be a *spray* that describes an area of low dose outside the core. The halo and aura can take up a significant part of the proton energy (e.g. 15 % at 180 MeV). In order to outline the nuclear halo at a given energy, one can use a single pencil beam with selected radii and measure the depth dose with a small absolute beam monitor. Dose buildup depends on both beam and detector size, reaching full buildup only with small detectors and beam sizes that can provide equilibrium in the measured region [71, 75].

1.2.6 Photon vs. proton therapy

One way to compare photon and proton beams includes the depth-dose distribution shown in Figure 1.9. While protons have a finite depth range that is subject to their energy and the density of the electrons in matter, photons display an infinite depth range with exponentially decreasing doses [76]. In clinical applications, the photon energies typically lie in the range of 4-10 MeV with a dose maximum at around 1-3 cm depth, thus preserving skin tissue [34]. Meanwhile, proton beams can be applied in the form of a spectrum creating a SOBP within the target volume while sparing the tissue beneath [76].

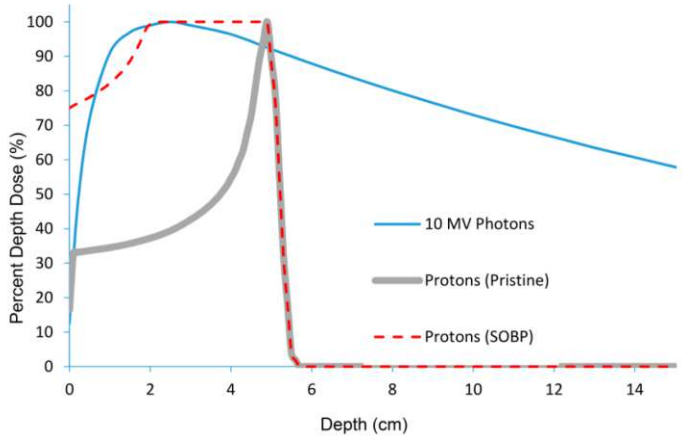

Fig. 1.9: Percent depth dose curve of photon beams and proton beams including an example for a SOBP. Taken from [77].

For another form of comparison, one can also look at the relative biological effectiveness (RBE) as discussed by Paganetti and Luijk [78]. Here, the RBE can be used to determine the dose needed in proton treatment in order to achieve the same biological effect as the reference dose used in photon treatment [78]. In practice, patients receiving proton therapy are subject to 10% less dose as compared to photon therapy patients [78, 79]. A parameter which correlates with the RBE is the linear energy transfer (LET) which is defined as

$$LET = \frac{dE}{dx} \tag{1.6}$$

with energy loss dE and unit path length dx [78]. As described by Gulliford and Prise [80], the higher ionization density of particles compared to photons translates to a higher LET for proton beam therapy. A higher LET, in turn, means more double-strand breaks take place which then increase the probability of cell death. Thus, the RBE for cell death increases with increasing LET until saturation is reached and increasing energy shows no further effect. Another important factor that is LET dependent and influences the RBE is

the oxygen composition of the tumor. Treatment forms with lower LET (like photons) have less effect on hypoxic tumor regions since oxygen plays an essential role in converting radicals to peroxy radicals which then cause DNA damage. This effect decreases with increasing LET [80].

Looking at the discussed factors, one could assume that proton therapy is more effective than photon therapy, which, in reality, is not the case as shown by Chen et al. in their recently published clinical review [63]. The enhanced dose distribution in proton beams may not provide clinically significant benefits since photon therapy uses tolerance doses for organs at risk (OAR). Additionally, there is minimal anatomical overlap of spared areas in studies comparing proton and photon beams. Another important aspect is the sensitivity of proton therapy to any changes in the patient (e.g. weight fluctuations, tumor changes, patient setup, patient motions) which result in higher doses in unwanted regions or lower doses in the target region. Also, the proton therapy treatment forms used for comparison play a role in the outcome. Active scanning proton therapy has shown better results than IMRT for cancers in the head and neck region, the thorax, the craniospinal region and pediatric regions of the central nervous system, while passive scattering proton therapy in prostate, lung and esophageal cancers shows no significant improvement. Hence, more research is necessary to come to a definite conclusion [63].

1.3 Dosimetry

To ensure successful cancer treatment with radiotherapy, the dose delivery accuracy must be assessed frequently [81]. Radiation dosimetry encompasses the measurements and calculations to ascertain the absorbed dose in a medium, giving insight into the effects caused by ionizing radiation [82]. The dosimetric procedure must consider relevant calibration coefficients and correction factors so that the measured value comes as close as possible to the true value within acceptable uncertainty bounds, while also ensuring that the results are reproducible and comparable to other institutions by recording all relevant quantities and parameters such as the absorbed dose [83].

1.3.1 Dosimetric quantities

The interaction of ionizing radiation with matter is described in Section 1.2.1. In the process of interactions, there is an energy transfer that can be characterized by dosimetric quantities [82, 84]. The following quantities are based on the handbooks by Podgorsak [16] and Mishra and Selvam [82] as well as the ICRU report published in 2011 [84].

Kerma

Kerma stands for "kinetic energy released per unit mass" and is defined as

$$K = \frac{dE_{tr}}{dm} \tag{1.7}$$

where dE_{tr} is the mean sum of initial kinetic energies transferred from the indirectly ionizing particles to all the charged particles that are then emitted within the irradiated mass dm of the medium, given in unit gray ($Gy = \frac{J}{kg}$). Thus, it includes any secondary electrons released through e.g. Photo-electric effect, Compton scatter, de-excitation of atoms/molecules/nuclei, and radioactive decay while excluding any energy required to overcome the binding energies of the secondary particles.

Cema

Cema is the "converted energy per unit mass" and the equivalent of Kerma when the incoming radiation stems from directly ionizing (charged) particles such as protons and electrons. Cema is defined as

$$C = \frac{dE_{el}}{dm} \tag{1.8}$$

with dE_{el} being the mean energy lost in electronic interactions within the mass dm of a medium. In contrast to Kerma, the energy in Cema accounts for the initial kinetic energy of the released electrons as well as the energy needed to overcome the binding energy of the electrons, while excluding any further energy lost by the secondary electrons after the initial release. The unit of Cema is gray (Gy).

Absorbed Dose

The absorbed dose handles both directly and indirectly ionizing radiation and describes the energy imparted to a medium. The definition is

$$D = \frac{d\bar{\varepsilon}}{dm} \tag{1.9}$$

where $d\bar{\varepsilon}$ stands for the mean energy imparted by ionizing radiation to mass dm within a medium in unit gray (Gy). The energy imparted $\bar{\varepsilon}$ gives the sum of all energy entering the volume of mass m minus any energy leaving it. This includes all kinds of mass-energy conversations, e.g. pair production (energy decrease) or electron-positron annihilation (energy increase).

Connecting the three quantities

All three quantities are non-stochastic, although the absorbed dose stands in relation to the energy imparted which is a stochastic quantity. In the case of charged particle equilibrium (CPE), both Kerma and Cema can be considered approximations for the absorbed dose, with the former applying for indirectly ionizing radiation such as photon beams, and the latter for directly ionizing radiation like proton beams.

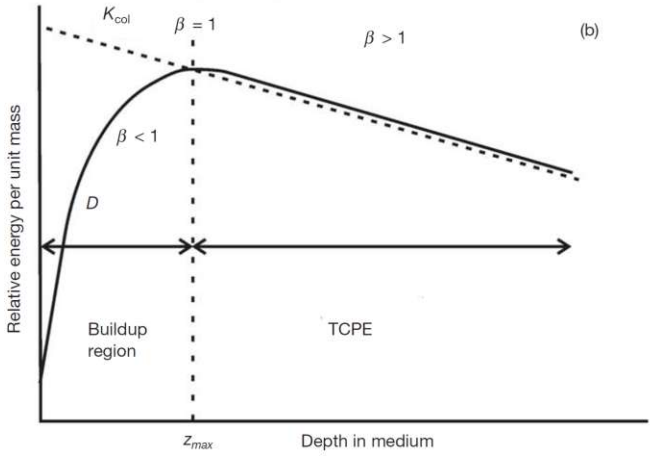

Fig. 1.10: Relationship between collision Kerma K_{col} and absorbed dose D. At the depth of maximum dose z_{max}, $\beta = 1$ and thus CPE is found. Taken from [16].

CPE, for example in photon beams, describes the equilibrium in which both the generation of charged particles through indirect ionization (=Kerma K) and the energy deposition of the released secondary electrons (=absorbed dose D) takes place. Usually, due to a finite range of the liberated electrons, these locations differ. Electrons can lose their energy when ionizing other atoms or when being deflected which leads to the production of bremssstrahlung. Collision Kerma K_{col}, which describes energy lost through ionization, is typically enough to describe the absorbed dose, since radiative Kerma K_{rad} takes place outside the volume of interest. It depends on the photon fluence present and since photon fluence decreases with depth, so does K_{col}. Absorbed dose D, on the other hand, will at first increase with depth since the released electrons from upper regions deposit their energies at deeper regions within the medium. Only after reaching a maximum dose, does the decreasing photon fluence also show an effect on the absorbed dose and thus decrease it. The point of intersection, where $\beta = \frac{D}{K_{col}} = 1$ applies, is the so-called CPE. Beyond CPE, only the photon energy and the medium itself determine the difference in D and K_{col} [16, 82, 84].

1.3.2 Cavity theory

When measuring the absorbed dose D in a medium, a radiation sensitive device such as a dosimeter needs to be placed inside the medium [16]. The sensitive medium is referred to as the cavity since it consists of a material that generally differs from the medium of interest it is planted in [16, 82]. The cavity can vary from solid materials (e.g. diode) to gaseous ones (e.g. ionization chamber) [82] and its size can be classified as small, intermediate and large when compared to the ranges of secondary charged particles [16]. The cavity theory offers a relation between the absorbed dose to the cavity (dosimeter) and the absorbed dose to the medium of interest [16, 82]. For photon beams, different cavity theories have been introduced including Bragg–Gray and Spencer–Attix cavity theories for a small cavity as well as the Burlin theory for an intermediate cavity size (which will not be covered here) [16]. Explanations of the different theories are summarized based on the work of Podgorsak [16] and Mishra and Selvam [82].

Bragg-Gray cavity theory

For the Bragg-Gray cavity theory [85–87], two conditions have to be met [88, 89]:

(a) The cavity's presence must not perturb the charged particle fluence in the medium. Therefore, the size of the cavity has to be small compared to the range of charged particles passing through.

(b) Charged particles are neither produced in the cavity, nor do they stop inside. The absorbed dose in the cavity only comes from charged particles passing through.

Since condition (a) requires equilibrium fluence, any perturbation needs to be corrected with a correction factor. Furthermore, the condition only applies from CPE onwards (see Figure 1.10). As for condition (b), secondary electrons or delta electrons produced inside the cavity are to be excluded.

If the conditions are met, the absorbed dose in the medium D_{med} is related to the absorbed dose in the cavity D_{cav} via the following equation:

$$D_{med} = D_{cav} \left(\frac{\bar{S}}{\rho} \right)_{cav}^{med} \tag{1.10}$$

$\left(\frac{\bar{S}}{\rho}\right)_{cav}^{med}$ gives the mean unrestricted mass collision stopping power ratio of medium to cavity.

Spencer-Attix cavity theory

The Spencer-Attix cavity theory [89–92] is an extension of the Bragg-Gray cavity theory for small cavities. While being subject to the same two conditions, the theory accounts for secondary particle fluence in addition to the primary particle fluence. An energy threshold Δ categorizes secondary electrons, according to their kinetic energy E_k, as slow electrons ($E_k < \Delta$) or fast electrons ($E_k > \Delta$). Slow secondary electrons deposit their energy locally while fast secondary electrons pass the cavity before depositing their energy and thus lie within the electron fluence spectrum. The doses between the medium and cavity are related as follows:

$$D_{med} = D_{cav} \left(\frac{\bar{L}_\Delta}{\rho} \right)_{cav}^{med} \tag{1.11}$$

The term $\left(\frac{\bar{L}_\Delta}{\rho}\right)_{cav}^{med}$ gives the mean restricted mass collision stopping power ratio of medium to cavity. An adapted version of the Spencer-Attix cavity theory [93] is typically applied when the absorbed dose in a medium is calculated from the absorbed dose in a wall-less detector [16, 82].

1.3.3 Phantom dosimetry

In phantom dosimetry, phantoms are used to measure dose distributions in simulated patient settings, having the advantage that the dosimeter can be placed in a region of interest within the phantom [81]. Phantoms can be classified as homogenous (simulating water only), heterogeneous (density rods can be inserted to simulate various tissues) and anthropomorphic (simulating the human body) [94]. The choice of materials strongly depends on their characteristics as the phantom needs to meet the requirements of its application field [95]. For example, a polystyrene phantom offers an electron density that is near water-equivalent [96, 97] and can be built in a way that leaves little to no air space between the polystyrene and the inserted dosimeters [96]. The various types of phantoms are displayed in Fig. 1.11.

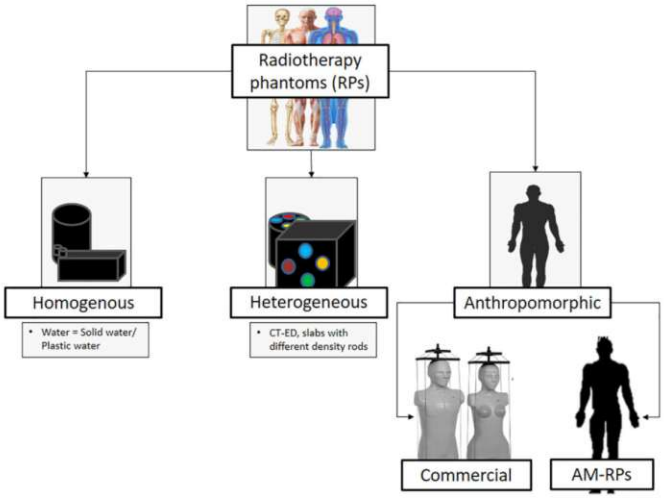

Fig. 1.11: Types of phantoms. Taken from [94].

1.4 Radiation detection

A radiation dosimeter is a tool used to measure or assess quantities of ionizing radiation such as Kerma and absorbed dose, either directly or indirectly, and its sensitive volume can consist of either a gaseous, liquid or solid medium [16]. Ionizing radiation detectors have continuously improved over the years and thus contributed significantly to the progress made in fields such as radiology, nuclear medicine and radiotherapy [98]. Each radiation dosimeter is characterized according to properties like accuracy, linearity, energy dependence etc. and the choice of the device depends on the measurement setting [16].

1.4.1 Radiochromic films

Radiochromic films are dosimeters with the characteristics of high spatial resolution [99, 100], near water equivalence [99–101] and low energy dependence [99–104]. Among those films, GafChromic films are widely used as they have near tissue equivalence and turn from colorless to a blue dye when irradiated [16]. The intensity of the dye directly relates to the absorbed dose of the medium and can be connected through a calibration equation [105]. Radiochromic films are self-developing, easy to use, and can be handled under normal room conditions [16]. Their main field of application comprises the measurement of two-dimensional dose distribution for dose verification in photon, electron and proton therapy treatments [105–109] which can be achieved with very high resolution [105]. Due to the minimal thickness of the films beam perturbations are practically negligible and, as relative dosimeters, radiochromic films can attain precision below 3% [16].

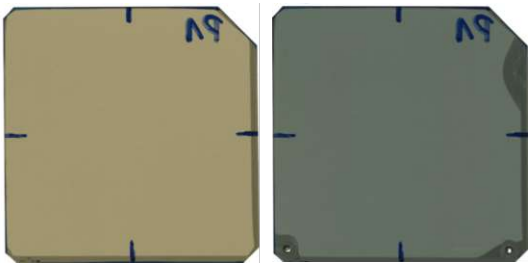

Fig. 1.12: Examples of radiochromic films pre-irradiation (left) and post-irradiation (right).

1.4.2 Ionization chambers

Ionization chambers are the most commonly used dosimeters for accurate machine output measurements in radiotherapy [16]. The verification process of IMRT plans is typically carried out by experiments using a phantom [110–113], where films are used for dose distribution measurements and the ionization chamber determines the absolute dose [110, 114, 115]. Before ionization chambers can be used for absolute dosimetry, they must undergo calibration at a standard dosimetry laboratory [116]. To gain a better understanding of ionization chambers, the following paragraphs are based on the comprehensive explanations in Podgorsak's handbook [16].

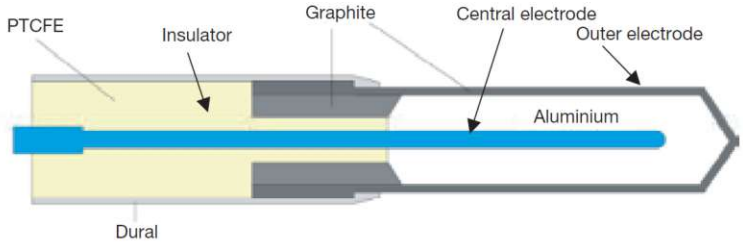

Fig. 1.13: Schematic of a cylindrical Farmer type ionization chamber, taken from [16].

The shapes and sizes of ionization chambers may vary depending on their use but they all share certain properties. For once, each ionization chamber consists of a gas-filled cavity with a collecting electrode in the center and a conductive outer wall. To minimize leakage current, a high quality insulator is placed between the wall and electrode. Furthermore, a guard electrode is placed in the chamber to direct the leakage current to ground instead of being collected by the collecting electrode. This leads to better field uniformity in the sensitive volume. Lastly, in case of open air ionization chambers, the room conditions and thus influence on the mass of air in the volume of the chamber are accounted for by applying temperature and pressure corrections.

Cylindrical chambers typically have a sensitive volume between $0.1 - 1cm^3$ as well as a buildup cap for calibration free in air when using ^{60}Co radiation, and they consist of tissue or air-equivalent material. The chamber built aims to be homogeneous and low energy dependence is achieved by placing a $1mm$ thick aluminium electrode in the center.
In contrast, a parallel-plate ionization chamber has two plane walls, where one electrode polarizes the incoming radiation beam and the other collects it, among other properties.

In order to convert the current or collected charge of the ionization chamber into a signal, the dosimeter is connected to an electrometer. The electrometer is an operational amplifier with a standard resistor or capacitor in the feedback path for measurements over a fixed time interval that provides high gain and negative feedback.

In dosimetry, the sensitive volume of an ionization chamber is typically ambient air and the dose D is derived from the measured ionization charge Q. With the use of the Bragg-Gray or Spencer-Attix cavity theory (previously discussed in Section 1.3.2), the air cavity dose D_{air} can be converted to the dose to a medium like water D_w. If reference conditions can't be met, a correction of the signal is needed in terms of room temperature, pressure and humidity, applied chamber voltage and polarity, chamber leakage currents, chamber stem effects and more.

The ionization chamber response (current I or charge Q) depends on the applied voltage V at a fixed dose rate or dose, respectively, and is demonstrated in the saturation curve (see Fig. 1.14).

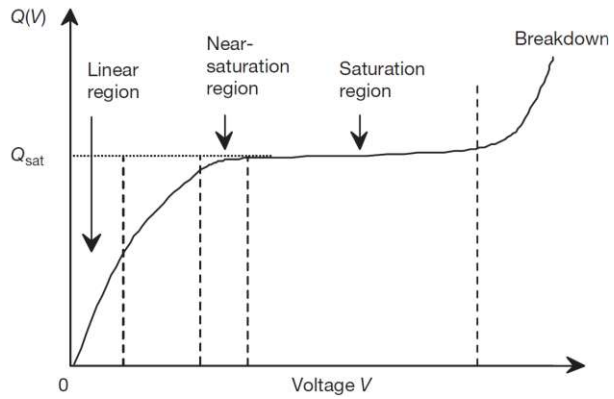

Fig. 1.14: Typical course of the ionization chamber saturation curve where the usual operating range of the chamber lies in the near-saturation region and the saturation point is marked by the saturation charge Q_{sat}, taken from [16].

At low voltages, there is a linear relationship between charge Q and applied voltage V, as some charges produced by radiation recombine before being collected and thus do not appear in the signal. At higher voltages, the chamber response reaches saturation and all produced charges reach the collecting electrode. When the voltage is increased even further, the ionization chamber reaches a breakdown due to charge multiplication. The typical operating region for radiation dosimetry lies in the near-saturation region [16].

1.4.3 Absolute, relative and reference dosimetry

Differentiation between absolute dosimetry, reference dosimetry and relative dosimetry can be difficult at times [83]. Therefore, the terms will be discussed in this section as done previously by Podgorsak [16]. An absolute dosimeter can provide information on the dose based on first principles without the need of calibration factors (e.g. calorimetry). Reference dosimetry is used to perform calibration in water under reference conditions using ionization chambers calibrated to primary standards (calorimeters) or secondary standards. If prior calibration in a reference field and/or normalization to a reference point are required, it refers to relative dosimetry. Radiochromic films are relative dosimeters while ionization chambers can serve as relative, reference or absolute dosimeters, although the latter is rarely practiced in clinical settings as the uncertainty of operating the ionization chamber as an absolute dosimeter would be larger than by using it as a reference dosimeter [16].

1.5 Treatment planning

With the wide accessibility of computers in the 1970s, CT developed alongside and thus transformed the field of radiotherapy TP by providing a full 3D representation of the anatomy [117, 118]. This step enabled the direct visualization of superimposed dose distributions over the patient's axial anatomy [118]. Overall, TP in radiation therapy is a multifaceted process that involves several key steps, beginning with simulation and imaging, followed by segmentation and the creation of technical plans [25]. As summarized by Hansen et al. [25], there are various approaches to TP which will be explored in the following paragraph.

One fast approach for simple targets not requiring OAR sparing (e.g. breast or extremities) is forward TP or three-dimensional conformal radiation therapy (3DCRT) [119]. Here, important parameters such as field directions and sizes are initially set by the treatment planner before the dose distribution is calculated, analyzed and further optimized. If the target conformity is more complex or there are OAR to be accounted for (e.g. head and

neck region) IMRT and VMAT are used. These methods use inverse TP [120]. Here, the planner first decides on the target dose objectives and OAR constraints, often combined with prioritization weights, before going through a computer-assisted iterative optimization process where the MLC positions, their accompanied MU, intermediate-dose distribution evaluations and, in case of VMAT, additional beam directions are used to reach the best achievable plan. For even more complex cases (e.g. multiple targets), human planners may reach a limit in their capacity [121] and automated planning can be a helpful tool in the selection process of different objectives for optimization. Automated plans can be either knwoledge-based using a library of high-quality plans [122–124] or protocol-based aiming for iterative optimization according to a pre-established protocol [125, 126]. Yet another TP approach uses mathematical models trained on previous plans [127, 128] or a dose kernel simulating the dose fall-off [129] to achieve dose prediction. Lastly, there is also adaptive planning which accounts for any anatomical changes that occur during the time of treatment by frequently reassessing the patient's anatomy through online imaging (e.g. cone-beam computed tomography (CBCT) [130]), while typical TP approaches simply use larger margins [131]. The advantage of this approach is that there is a reduced risk in terms of OAR overdosage and target underdose but it comes with the disadvantage that the patient is lying on the treatment couch while the TP is adapted online [25].

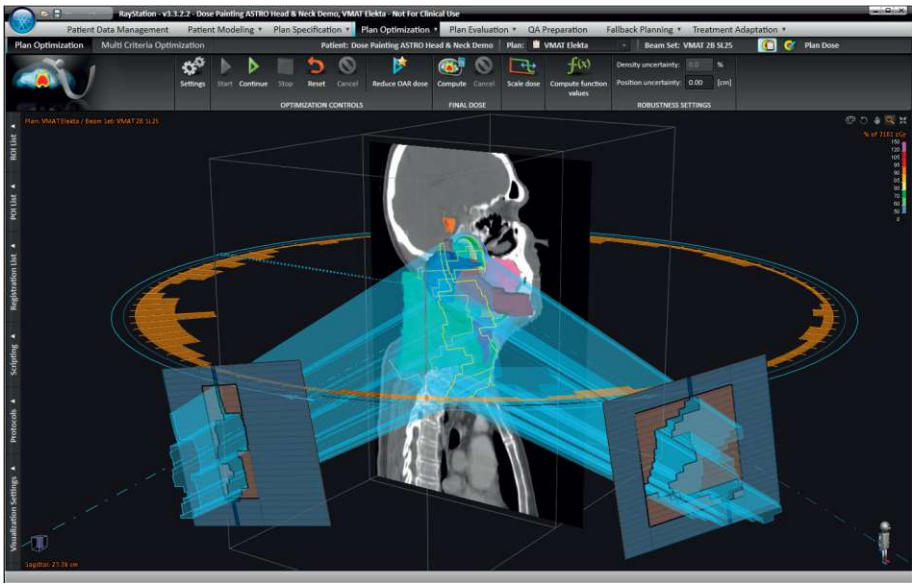

Fig. 1.15: VMAT plan optimization process in Raystation. Taken from [132]

In all the described TP approaches, a TPS is involved. The modern TPS refers to a computer system which consists of a beam model, a dose calculation engine and an optimization engine and optimizes the treatment settings to ensure a safe and effective dose distribution [133]. Evans [117] emphasized that dose calculation algorithms play the

most crucial part in the TPS due to their representation of the dose distribution within the patient, and his work will be the basis for discussing the various dose calculation algorithms in more detail in the following paragraph.

The first algorithm to be discussed is based on the principle of convolution and therefore, the dose at each position is given by the superposition of the primary and scatter components. In simple cases with non-divergent sources and homogeneous phantoms, integrals of convolution type can be employed. Another dose calculation algorithm uses MC or random sampling techniques which follow the trajectory of numerous particles beginning with their emission from the source up to multiple scattering interactions within and outside the patient. For statistical significance, MC algorithms require a large number of particle histories which leads to extended calculation time. Only recent advances in computational power made it possible for such calculation time to be reduced and thus MC are now becoming a part of clinical TP. A third dose calculation algorithm is given by the pencil beam algorithm, although this algorithm is only relevant for electrons (or carbon ions). Hereby, the sum of either the energy spread or the dose kernel along a line within the phantom represents a pencil-type beam or the dose distribution [117].

1.6 Metal implants in radiotherapy

Radiotherapy is a complex process involving various steps ranging from the immobilization and imaging of the patient, the target volume definition of the tumor and treatment planning (see Section 1.5) up to the treatment delivery with setup verification [8]. The continuous progress made in image-guided radiotherapy (IGRT) has led to increased accuracy in dose delivery at a smaller planning target volume (PTV) [134–136]. However, this also calls for high delineation accuracy regarding tumor volume and sensitive structures in the vicinity of the treatment area [137] as even the smallest deviations can leave OAR with higher or the target region with less radiation exposure [134].

Metallic implants present in the hip, spinal and tooth region can greatly impact the necessary image quality [136, 138–141]. During treatment planning, imaging of the patient is most often performed using CT [137] where the projection data is obtained from different angles and an image is reconstructed via filtered back projection (FBP) or an iterative method [136]. The HU then give insight into the electron density of the different tissues in the target region [142].

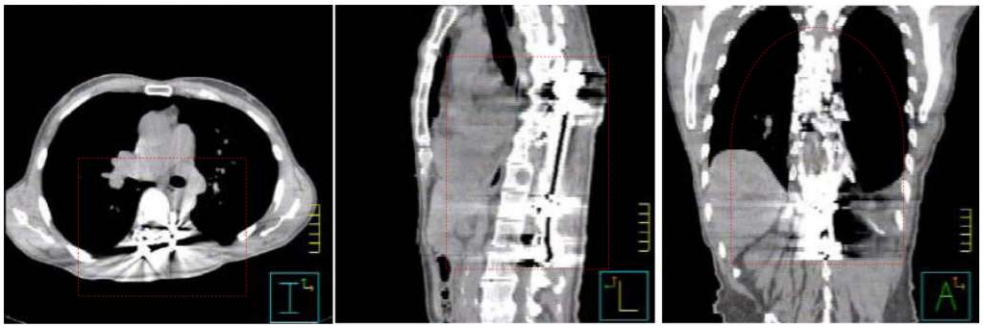

Fig. 1.16: Metal artifacts in a diagnostic kVCT scan of a patient with metal implants in the spine - transverse view (left), sagittal view (middle), coronal view (right). Adapted from [143].

When a metal implant is present, errors will occur in the projection data due to effects such as photon starvation, beam hardening, noise, scatter or non-linear partial volume effects [136]. As described by Giantsoudi [137], beam hardening results from the more likely absorption of lower energy photons by matter with high atomic number Z, thus shifting the average beam energy to higher energy levels. Since Compton scatter is the predominant interaction in CT, the combination with beam hardening will lead to dark streaks at the axis of greatest attenuation in the reconstructed image, while the metal object will appear as white. In extreme cases, the absorption will even result in photon starvation as the photons reaching the detector fall to or lower than the noise level. Such detected photons don't follow Poisson distribution and will increase statistical errors which appear as thin dark and bright streaks in the image [137].

A possible solution to reduce the problem metallic implants cause in CT images includes the manual pixel-by-pixel compensation where erroneous CT numbers from an artifact region are overwritten with ones according to the relative electron density of water or surrounding tissue [134, 136, 138, 144, 145]. However, this method is very time-consuming, operator-dependent, not always applicable, and bears the risk of systematic errors [136]. Further options are given by metal artifact reduction (MAR) algorithms [134, 137, 145–152] and dual energy computed tomography (DECT) virtual monochromatic (VM) extrapolations [134, 153] which have, in certain cases, shown reductions in beam hardening artifacts [134, 154–156], better contrast to noise ratios regarding soft tissues [134, 157, 158] and enhanced accuracy in dose calculation [134, 159].

Still, the streaking artifacts disrupt the accuracy of the acquired HU and thus lead to increased uncertainty regarding accurate delineation and dose calculation of OAR and tumors [134, 137–142, 160–164]. By extension, the imaging errors also affect the dose delivery which can cause insufficient irradiation of the tumor and radiation toxicity of OAR

[136, 137]. However, dose calculation is not just affected by imaging artifacts but also dose calculation algorithms such as pencil-beam algorithms which have difficulties modeling the tissue/metal interface effects accurately. [136, 165]. At present, the convolution/superposition (C/S) method is the standard for dose calculation in photon beam therapy, but unless the implant is well defined in its density and dimensional properties [165], there will be an underestimation of the backscatter dose enhancement at the proximal interface as well as an overestimation of the dose directly downstream of the implant [136, 165, 166]. Resulting dose errors only appear locally, but they can rise up to 30 % depending on the photon energy and metal [136, 165, 167, 168]. In this regard, MC simulations have shown to be more accurate in terms of dose estimation near metal implant [136].

Overall, these uncertainties have an even greater impact in proton therapy [136]. Here, the HU translate to the relative linear proton stopping powers which are used for dose and range calculations [137, 142, 145, 148, 169] and in case of streaking artifacts, the HU values can saturate [137]. Any inaccuracies in the proton range lead to a potential shift of the area the high dose is delivered to since proton beams deliver high doses in the Bragg peak [142]. Photon beam therapy is less affected by such a shift since the dose attenuates exponentially within the tissue [145]. Hence, irradiation in proton beam therapy should be planned so that beam paths do not pass metal implants, if possible [142].

1.7 Aims of this thesis

This thesis aims to improve our understanding of how the dose is deposited by photon and proton beams in tissue near a metal implant during radiotherapy treatment. The main tasks included photon and proton beam measurements using a polystyrene phantom with inserted metal implants and radiochromic films, and then analyzing any deviations from the calculated dose distribution using MC and collapsed cone (CC) algorithms. Additionally, for the photon beam experiments, a new film scanner was calibrated for better evaluation.

2 Materials and Methods

2.1 Beam sources

Photon beam experiments were carried out using the LINACs present at the Department of Radiation Oncology, Medical University of Vienna. Proton beam experiments took place with a particle accelerator at MedAustron, Wiener Neustadt.

2.1.1 Linear accelerator

The Department of Radiation Oncology, Medical University of Vienna is equipped with five LINACs from Elekta Versa HD which can produce X-rays at energies 6 MV, 6 MV FFF, 10 MV and 10 MV FFF, respectively. Depending on availability, measurements were conducted at LINACs D and E, and all energy options were explored in the photon beam experiments.

Fig. 2.1: Linear accelerator as a high energy photon source at the Department of Radiation Oncology, Medical University of Vienna.

2.1.2 Particle accelerator

At MedAustron, there are four irradiation rooms (see Figure 1.4) from which three are in clinical operation whereas one is used for non-clinical research (NCR) and provides proton energies up to 800 MeV [170]. The proton beam experiments were conducted in the non-clinical irradiation room with proton energies ranging from 75 to 138 MeV.

Fig. 2.2: NCR room at MedAustron with a fixed horizontal beamline emitting the desired protons from the particle accelerator.

2.2 Detectors

For the experiments, radiochromic films were placed either inside the metal phantom or between solid water layers to measure dose distributions, and an ionization chamber functioned as an absolute dosimeter for dose verifications.

2.2.1 Film dosimeter

The radiochromic films used in this work are GafChromic EBT3 films (Ashland, New Jersey, USA). They measure the absorbed doses of ionizing radiation and work very well for high-energy photons in the range of 0.2 to 10 Gy [171], which suited this work as most measurements were conducted with doses of 2 Gy. The advantage of EBT3 films compared to prior types is the symmetry in the layers to move the effective point of measurements to the center as well as the matte coating to avoid Newton-ring artifacts [172, 173].

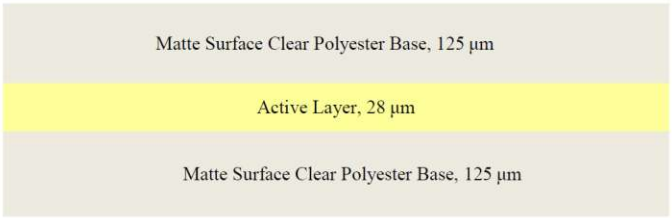

Fig. 2.3: Layers of GafChromic EBT3 films. Taken from [171].

GafChromic EBT3 films from two different lots (manufacturer identification numbers) were used in this work. For the photon beam experiments including the scanner calibration, films were taken from lot no. 11192002. Proton beam experiments were conducted using films from lot no. 03082203. Film cutting and labeling were performed by facing an upwards curvature of the film sheets towards the center and a downwards curvature towards the sides. After irradiation, films were stored to develop for 36 hours before scanning.

For film scanning, two different EPSON scanners were used. The proton beam experiments at MedAustron were evaluated with the available EPSON Expression 11000XL scanner. For photon beam experiments at the Department of Radiation Oncology, Medical University of Vienna, a newly operating EPSON Expression 12000XL scanner was calibrated and used to analyze the irradiated films. Both scanners have a DIN A3 scanner surface. All films were scanned in portrait orientation, aligning the film sheet's long edge to the scanner surface's long edge. The scanner settings included a 48-bit RGB color channel, a resolution of 150 dots per inch (DPI) and no color correction.

Fig. 2.4: EPSON scanner used at MedAustron.

One drawback of film scanners is that there are lateral scan artifacts, where the measured pixel value depends on the positioning of the film relative to the center of the scanner surface [171, 174–177]. The effect was examined in this work (see Section 2.4.3). To avoid such distortions, individual film scans were performed at the center of the scanner surface and templates were prepared to ensure identical positions of each film scan.

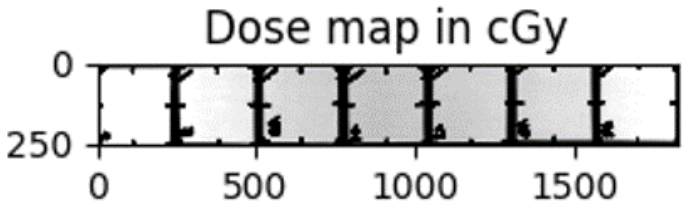

Fig. 2.5: Example of a lateral scan artifact in a scanned row of films.

GafChromic EBT3 films were used in many measurements throughout this thesis. Hence, Figure 2.6 gives an overview of the films' various applications described in Sections 2.4 and 2.5.

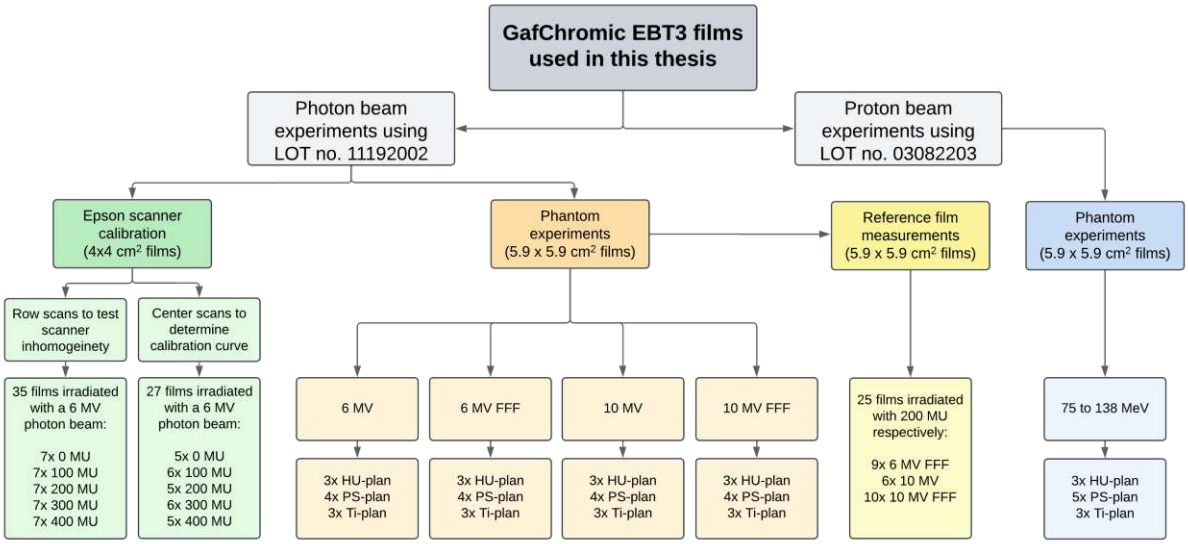

Fig. 2.6: Fields of application of the 138 irradiated GafChromic EBT3 films in this thesis. During the scanner calibration, the measurement had to be repeated once due to initial wrong positioning on the scanner, which is why 35 films were used in the row scans while 27 were scanned in the center.

2.2.2 Ionization chamber

For dose verification, PTW semiflex 0.125 cm^3 ionization chambers (type 31010, PTW, Freiburg, Germany) were used for dose verification in reference dosimetry (see Section 1.4.3). Serial no. 6012 was applied for the proton beam experiments and serial no. 5866 for the photon beam experiments. For charge collection (unit pC), the ionization chambers were connected to a PTW UNIDOS electrometer.

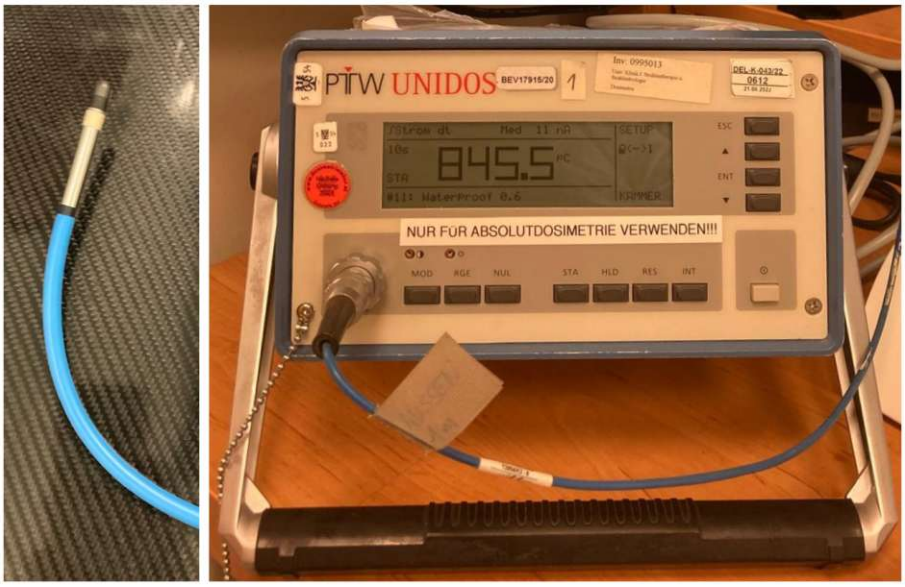

Fig. 2.7: Semiflex ionization chamber (left) and electrometer (right) used for reference dosimetry measurements at the Department of Radiation Oncology, Medical University of Vienna.

Type 31010 ionization chambers are watertight, air vented ionization chambers with an active volume of 0.125 cm^3, an aluminum electrode and a high energy range between 30 mGy and 6.6 Gy [178]. Cross-calibration was previously performed against a Farmer chamber calibrated at the Seibersdorf Laboratories. Thus a calibration factor N_{D,w,Q_0} in [Gy/nC] for the absorbed dose to water was applied. Before measurements were taken, temperature and pressure conditions were determined and accounted for through a calculated air density correction factor $k_{T,p}$. Further fixed correction factors are applied for the beam quality (k_{Q,Q_0}), polarity (k_p) and the lack of charge collection due to recombination (k_s).

2.3 Phantom

The phantom used in the experiments was made of four polystyrene slabs with four polystyrene screws holding them together. Central to the screws, two insertion units could be installed and the ionization chamber was inserted in the central rod. Between the two middle slabs, a radiochromic film was placed and fixated by two small pins. At the front and back of the film, either polystyrene inserts or titanium screw inserts were placed. A similar type of phantom, but with a different central part, had previously been developed and tested by Wesolowska et al. [179], while the exact same phantom was examined in the work of Lechner et al. [180].

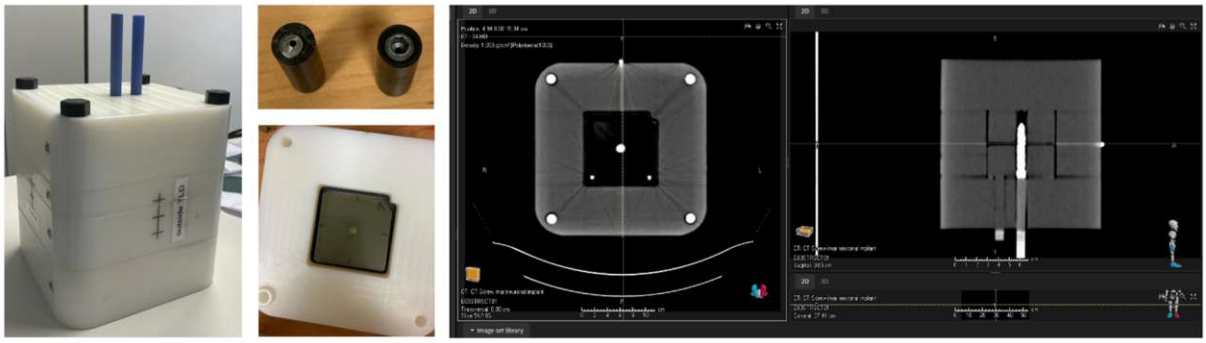

Fig. 2.8: Metal phantom used in photon and proton beam experiments - the phantom as a whole (left), metals screw inserts (upper center), film placement (lower center) and phantom CT scans (right).

The examined screw was a VERTAUX pedicle screw manufactured by Auxein Medical, India with a diameter of 6.5 mm and a length of 55 mm. It is typically used in surgeries on the vertebral body. For the purpose of this thesis, the screw was divided into two parts and enclosed in polystyrene (see Figure 2.8).

Fig. 2.9: Example for the VERTAUX pedicle screw used in this thesis. Taken from [181].

2.4 Film calibration

To evaluate the GafChromic EBT3 films for the photon beam experiments at the Department of Radiation Oncology, Medical University of Vienna, a EPSON Expression 12000XL was calibrated. The existing scanner protocol served as guidance for the calibration procedure and the evaluation of the scanner inhomogeneity. Since radiochromic films are relative dosimeters, reference dosimetry was performed to determine the calibration curve, and the semiflex ionization chamber (serial no. 5866) was used to relate the MU to the absorbed dose.

2.4.1 Setup for reference dosimetry and calibration measurements

For the setup, a 10×10 cm^2 field and solid water slabs were used to create reference conditions. First, the ionization chamber was placed at source-to-surface distance (SSD) 90 cm and 10 cm solid water depth, and measurements were taken for 6 MV photon energies and 100 MU. In the next step, the upper solid water slabs were replaced so that individual 4×4 cm^2 radiochromic films could be placed at the exact same position as the ionization chamber. Measurements were then performed for 0, 100, 200, 300 and 400 MU corresponding to 0, 1, 2, 3 and 4 Gy. For each setting, 5-7 films were irradiated.

Fig. 2.10: Setup for the reference dosimetry and calibration measurement. First, the ionization chamber was inserted in the center for absorbed dose to water dosimetry (left), then the solid water was replaced to fit the radiochromic film at the same position (middle) before placing 10 cm thick slabs on top of the film for the measurement (right).

2.4.2 Calibration procedure

To determine the calibration curve, a total of 27 4×4 cm^2 films were scanned in the center of the EPSON scanner surface after a 36-hour developing period. They were then evaluated using an in-house developed Python script where the background scans, which were taken before the measurement, and the scans after measurement were imported. When scanning radiochromic films, multichannel scanners provide the signal in RGB colors allowing obtaining the information either from a single color channel or all three color channels [100]. For most cases in dosimetry, the red channel is chosen as it contains the maximum wavelength of the absorption spectrum [108, 182–184]. The green and blue channels can be used to reach a higher dynamic range of the films in regards to doses [100, 185–189] as well as divide dose-dependent and dose-independent parts of a signal and compensate for artifacts, variations of active layer thickness, and so on [100]. For this calibration procedure, the pixel values (PV) were obtained by reading out the red channel. The calibration curve was obtained using the rational fit function

$$X(D) = \frac{a+b}{(D-c)} \tag{2.1}$$

where $X(D)$ gives the scanner response at dose D and constants a, b, c, as previously discussed by Lewis et al. [190] and Ashland [191].

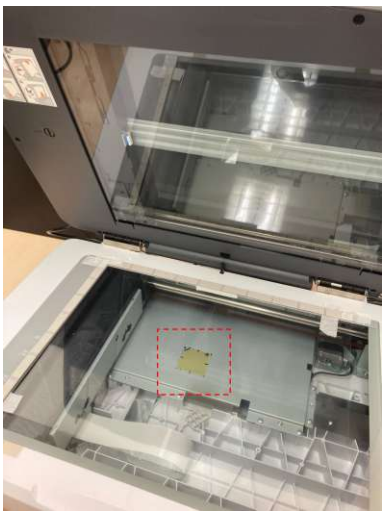

Fig. 2.11: Center scan for the determination of the calibration curve. To obtain the exact same scanning position throughout the calibration period and the photon beam measurements, the scanning area was first identified through the row scans (see Section 2.4.3) and marked. In the next step, overhead foils were cut out to fit the films at their center and fixated on the predetermined scanning area.

2.4.3 Evaluation of scanner inhomogeneity

Lateral scanner artifacts were determined by performing row scans with radiochromic films instead of placing each film at the center of the scanner. From the 35 4×49 cm^2 films, 7 were irradiated for each set of MU and thus used for one row of scans. Each row scan was repeated three times through the permutation of the films. Once a row scan was completed, the films were shifted to the next row to obtain scans of the entire scanning surface encompassing 10 rows. The process was then repeated for the next 7 films representing different MU.

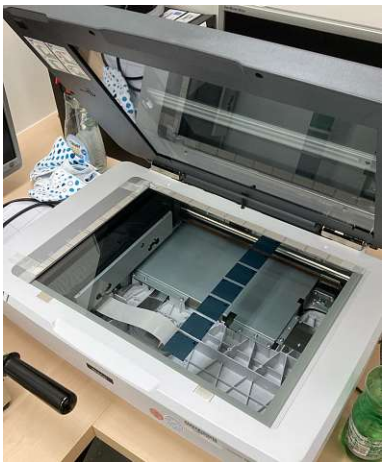

Fig. 2.12: Row scans for the evaluation of the lateral scanner artifacts. Films were placed in equal spaces across the scanning area.

In this calibration process, the films were evaluated by obtaining their dose from the pixel values in the red color channel within a ROI of 1×1 cm^2 in the center of each film as well as calculating the mean of the ROI for an $n \times n$ matrix using $\overline{PV_{ROI}} = \frac{1}{n^2} \sum_{i,j=1}^{n} PV_{ij}$. Since every film scan was assigned to a fixed position on the scanner surface and there were three permutations and thus scans for each position, another mean was calculated from the permutations for each position $\overline{PV_{pos}} = \frac{1}{3} \sum_{i=1}^{3} PV_{ROI,i}$. The resulting values were normalized to the central row (between row 5 and 6) and resulted in five matrices with 7×10 elements for each of the measured MU.

2.4.4 Uncertainty estimation

Bouchard et al. [99] discussed the many sources of uncertainty of GafChromic films during the calibration procedure, which have a significantly higher impact on measurement results than those of the ionization chambers, in their paper, thus serving as a guide for relevant countermeasures [99]. The following table provides an overview of the sources of uncertainties as well as the taken measures:

Source of uncertainty	Measures taken
Film manufacturing (Type B uncertainty)	
Emulsion homogeneity	All films within the same experiment are taken from the same lot; evaluation in photon beam experiment
Perturbation effects and energy dependence	6 MV considered, others neglected
Temperature and humidity dependence	Neglected due to hospital conditions
Sensitivity to polarized light	Short scanning periods
Stabilization of chemical reaction	Store for 36 h before scanning
LET dependency (Quenching)	Not considered
Film handling and characterization (Type B uncertainty)	
Foreign bodies (dust, scratches, fingerprints, folded edges)	Using gloves when handling films at all times, clean contact surfaces, use paper backing when cutting or storing
Storage environmental conditions	Wrapped in paper and kept in dark storage spaces with constant temperature conditions
Sensitometric curve uncertainty	use large number of points
Irradiation process (Type A/B uncertainty)	
Stochastic nature of dose deposition	Choose large enough ROI
Measurement setup uncertainty	4-eye-principle
Linac output reproducibility (Type A)	Use ionization chamber during film calibration; completing measurements within two hours to assume reproducibility
Dose variation within ROI	Using 6 MV beam with flattening filter, field size much larger than film and large enough ROI
Scanning process (Type A/B uncertainty)	
Stochastic nature of optical photon detection (shot noise)	Select ROI to analyse
Scanner homogeneity	Correct with polynomial fit (rowscans)
Scanner reproducibility and stability (Type A/B; dark noise, readout noise, scanner mechanics, lamp stability, Newton rings)	Warm-up scanner before use and scan each film 2-3 times
Numerical manipulation (rotation, registration)	Aligning films according to pinholes, neglected in scanner calibration

Tab. 2.1: Uncertainty sources and taken measures. Most sources are adapted from [99].

2.5 Phantom experiments

For the phantom experiments, three different treatment plans were created: a plan using the original CT numbers of the CT scan (HU), a polystyrene plan (PS) assigning polystyrene values to the phantom, and a titanium plan (Ti) assigning both polystyrene values to the phantom and titanium values to the titanium screw. For the original and titanium plan, a metal screw insert was placed in the front and back of the film inside the phantom. For the polystyrene plan, a polystyrene insert was used. For dosimetry, 5.9×5.9 cm^2 GafChromic EBT3 films were prepared, and a semiflex ionization chamber was used for dose verification in all measurements except photon beam energy 10 MV FFF due to failure of the dosimeter.

2.5.1 Reference dosimetry with the ionization chamber

At the start of each experiment, the room temperature and pressure conditions were determined with available measuring devices. The values were then entered into a pre-existing calculation tool to get correction factors for the pre-calibrated ionization chamber.

Temperatur:	23.9 °C	Luftdruck:	992.8 hPa	Kalibrierfaktor IAEA [Gy/nC]:	0.05322

Linac E - 6 MV		Linac E - 10 MV		Linac E - 6 MV FFF		Linac E - 10 MV FFF	
MU	200	MU	200	MU	200	MU	200
N_{D,w,Q_0} [Gy/nC]	0.05322	N_{D,w,Q_0} [Gy/nC]	0.05322	N_{D,w,Q_0} [Gy/nC]	0.05322	N_{D,w,Q_0} [Gy/nC]	0.05322
k_{Q,Q_0}	0.9903	k_{Q,Q_0}	0.9820	k_{Q,Q_0}	0.9909	k_{Q,Q_0}	0.9842
$k_{T,p}$	1.034	$k_{T,p}$	1.034	$k_{T,p}$	1.034	$k_{T,p}$	1.034
k_p	0.999	k_p	0.999	k_p	0.999	k_p	0.999
k_s	1.002	k_s	1.003	k_s	1.005	k_s	1.006
T [°C]	23.9	T [°C]	23.9	T [°C]	23.9	T [°C]	23.9
p [hPa]	992.8	p [hPa]	992.8	p [hPa]	992.8	p [hPa]	992.8
M [nC]	D [cGy]	M [nC]	D [cGy]	M [nC]	D [cGy]	M [nC]	D [cGy]
36.71	200.1					36.83	200.5
36.73	200.2					36.84	200.5
36.74	200.3					36.85	200.6
Mittelwert	200.2	Mittelwert	#DIV/0!	Mittelwert	#DIV/0!	Mittelwert	200.5
Std (%)	0.0%	Std (%)	#DIV/0!	Std (%)	#DIV/0!	Std (%)	0.0%
M [nC]	D [cGy]	M [nC]	D [cGy]	M [nC]	D [cGy]	M [nC]	D [cGy]
						6.90	37.6
Mittelwert	#DIV/0!	Mittelwert	#DIV/0!	Mittelwert	#DIV/0!	Mittelwert	37.6
Std (%)	#DIV/0!	Std (%)	#DIV/0!	Std (%)	#DIV/0!	Std (%)	#DIV/0!
Abweichung	#DIV/0!	Abweichung	#DIV/0!	Abweichung	#DIV/0!	Abweichung	-81.2%
Physiker							
Datum							

Fig. 2.13: Excerpt of the dose calculation tool for the ionization chamber used in the photon beam experiments.

In the next step, the ionization chamber was placed in the screw phantom and three measurements were performed with a 10×10 cm^2 field, 6 MV photon energy and 200 MU (=2 Gy) irradiation. The charges were translated to doses using the calculation tool. For the photon beam experiments, the resulting doses gave information on the LINAC

output on that day. During the film measurements in photon/proton beams, the ionization chamber measured the doses each film was irradiated with for dose verification. The temperature and pressure conditions were frequently adjusted to ensure the most accurate results.

2.5.2 Setup of the photon beam experiment

Photon beam experiments were conducted for energies 6 MV, 6 MV FFF, 10 MV and 10 MV FFF, each irradiating the phantom with a homogeneous dose of 2 Gy. Three VMAT treatment plans were developed for each energy and filter option, respectively. Gantry rotation around the phantom was set to be 200°, starting at 260° and rotating counterclockwise towards its end position at 100°. The phantom was placed at a 15° table angle, which ensured no collision with the gantry (compared with the 20° angle for the proton beam experiment in Section 2.5.3).

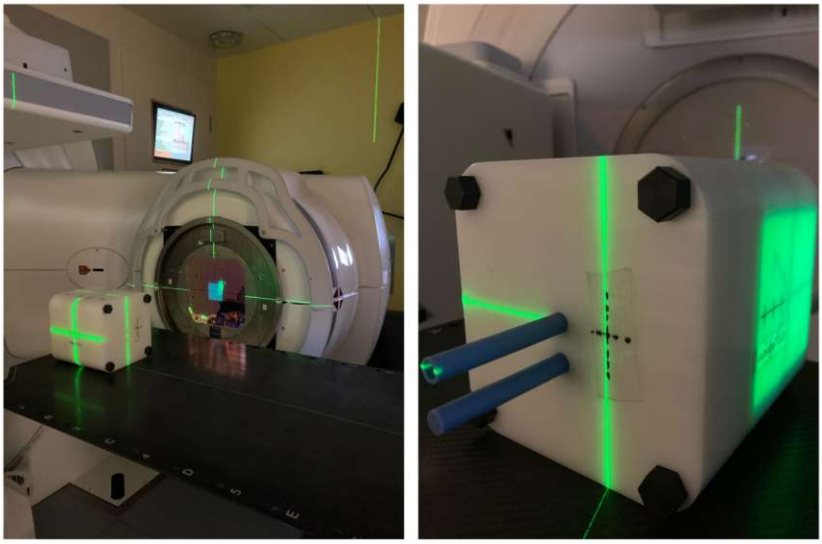

Fig. 2.14: Setup of the photon beam experiment (left) and phantom positioning (right) at the Department of Radiation Oncology, Medical University of Vienna.

2.5.2.1 Reference film measurement

In the course of the photon beam measurements, reference film measurements were conducted to test the homogeneity in the film thickness within one and over multiple sheets of the GafChromic EBT3 lot no. 11192002. 5.9×5.9 cm^2 films were used for the measurement. The setup for the reference measurements followed the one for the calibration measurements (see Section 2.4.1, where a 10×10 cm^2 reference field and solid water slabs were used. After dose verification, each film was placed at a 90 *cm* SSD and 10 cm solid water depth, and measurements were performed at energies 6 MV FFF, 10 MV, and 10 MV FFF, respectively, with 200 MU (= 2 Gy) irradiation.

2.5.3 Setup of the proton beam experiment

Proton beam experiments were carried out through a fixed horizontal beam line, from which protons irradiated the metal phantom with a homogeneous dose of 2 Gy and proton energies ranging from 75 to 138 MeV. The metal phantom was placed at a 20° table angle to ensure no protons could pass the phantom in possible air gaps between the slabs of the film and the phantom. This measure was executed by previous studies [192–194], as air gaps can cause artifacts in the dose distribution [192].

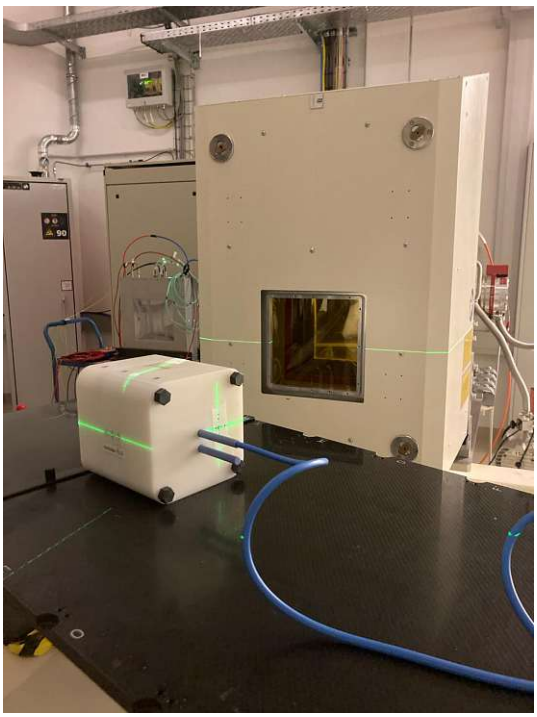

Fig. 2.15: Setup for the proton beam experiment with the metal phantom at MedAustron. The beamline at the NCR room was horizontal and fixed, while the table was moved to meet the requirements.

2.5.4 Film evaluation and data analysis

Depending on the beam modality (photon/proton) the irradiated radiochromic films were scanned by their respective scanners. Two python scripts were used for the film evaluation as the scanners were calibrated differently. Except for the dose determination (see Section 2.5.4.2), the irradiated films from the photon and proton beam experiments were processed and analyzed the same way.

2.5.4.1 Film alignment

Each treatment plan was irradiated to 3-5 films. For better evaluation and comparison, the radiochromic films had to be aligned with each other. When the films were inserted in the phantom, they were fixated by two small pins to stay in position. This fixation resulted in two pinholes at the bottom of the films, which were used for the alignment.

In the first step, the center position of each of the pinholes was determined for each film. Then, the angle Θ needed for bringing the pinholes into line was calculated using

$$\Theta = \tan^{-1}\left(\frac{perpenticular}{base}\right) \tag{2.2}$$

with the perpenticular being the y-distance between the pinholes and the base being the x-distance between the pinholes. The films were then rotated using an affine transform with the calculated angle. In the next step, the center positions of the rotated pinholes were once again determined. For each measurement setting, the two pinhole positions of one film served as reference for the translation of the other films. The x- and y-translation was determined as follows:

$$translation_{x,y} = \frac{[(pinhole^1_{x,y} - pinhole^1_{ref}) + (pinhole^2_{x,y} - pinhole^2_{ref})]}{2} \tag{2.3}$$

After obtaining the translation values, another affine transform was performed. The two transforms are depicted in Figure 2.16.

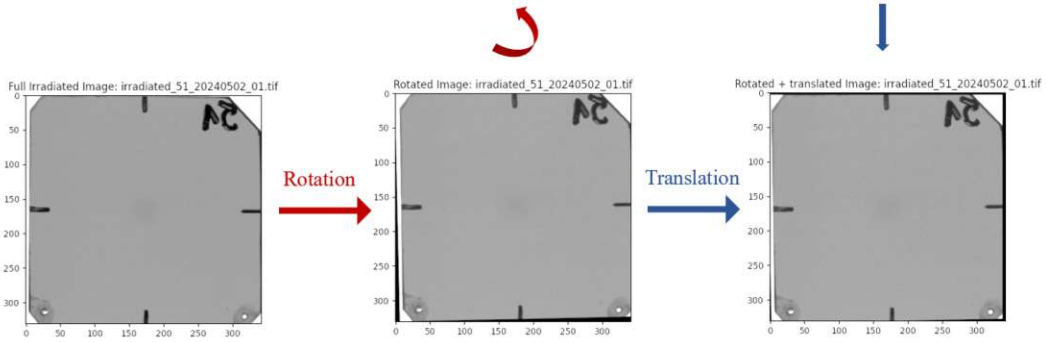

Fig. 2.16: Example for the alignment process of the GafChromic EBT3 films to align their positions in relation to their placement within the metal phantom.

2.5.4.2 Dose determination

Once the alignment was finished, the doses of the new matrices were calculated using the approaches discussed in Sections 2.4.2 and 2.5.4 and the films were individually saved as DICOM files. Dose profiles in the photon beam experiments were calculated using Equation 2.1 from the calibration procedure (see Section 2.4.2). For the proton beam experiments, a different approach was used. In accordance to Khachonkham et al. [173], one way to calculate optical density (OD) values from the mean PV of the red channel goes as follows:

$$OD_{irr,bg} = \log \frac{2^{16}}{PV_{irr,bg} + 1} \tag{2.4}$$

where 2^{16} are the maximum PV. Furthermore,

$$OD_{net} = OD_{irr} - OD_{bg} \tag{2.5}$$

gives the net OD through subtraction of the background film from the irradiated film [173, 195–197]. To obtain the calibration curve, a fitting function is used to convert the net optical density into absorbed dose, and for better accuracy, a higher degree polynomial with many fitting parameters can be chosen [184]. In this case, the quartic function

$$D(OD_{net}) = a \cdot OD_{net}^4 + b \cdot OD_{net}^3 + c \cdot OD_{net}^2 + d \cdot OD_{net} + e \tag{2.6}$$

with five constants a, b, c, d and e was applied to get the dose D.

2.5.4.3 Further alignment with the treatment plans in PTW VeriSoft

After aligning the films with each other, their DICOM files were uploaded in PTW VeriSoft together with their respective treatment plans. The isocenter of the treatment plans was determined and the center of the film's pinholes were once again used to align the film's isocenter with the isocenter of the treatment plans.

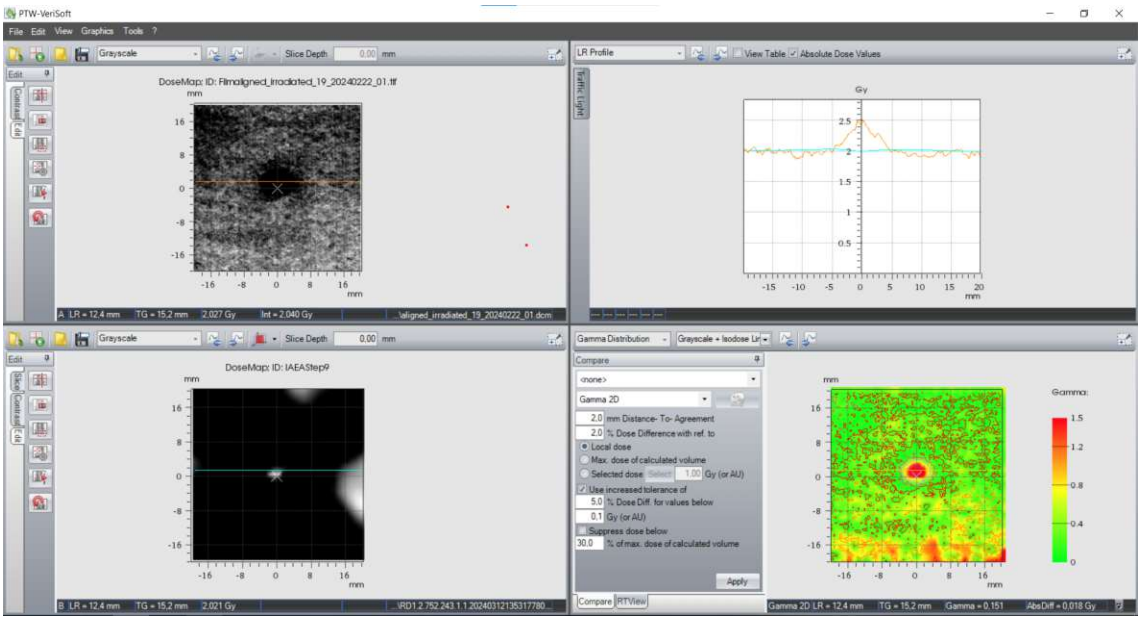

Fig. 2.17: Screenshot of the PTW VeriSoft software showing the dose map in the ROI of the GafChromic EBT3 film (upper right) and treatment plan (lower left), both left-right dose profiles (upper right) and their gamma distribution (lower right).

Once alignment between the radiochromic film and treatment plan was achieved, their dose profiles were normalized at a 10-20 mm distance away from the isocenter on the x-axis, and their doses were re-calibrated to 2 Gy in the area not affected by the metal screw. Subsequently, a ROI of 2×2 cm^2 for photon beam experiments and 2×1.6 cm^2 for proton beam experiments was cut out from both the radiochromic films and the treatment plans and their resulting dose matrices as well as gamma profiles were exported. According to Low et al. [198], γ is a quantitative measure to evaluate the dose calculation accuracy with $\gamma > 1$ being the criterion for a failed dose calculation. Therefore, the gamma profiles provide a visual representation of the divergence between the RayStation plan and the dose measurement. In some experiments, an additional MC simulation was performed using SciMoCa. The MC simulations were processed similarly to the radiochromic films and the treatment plans.

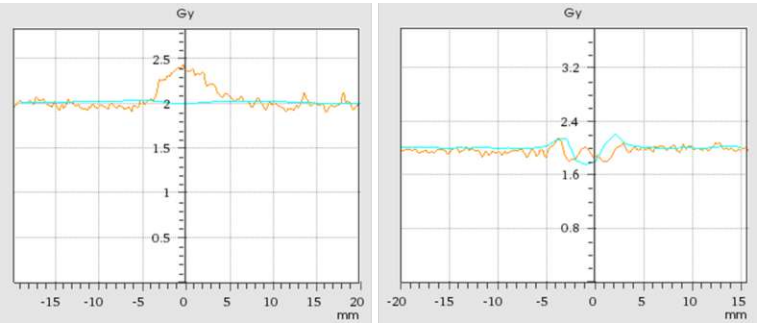

Fig. 2.18: Dose profiles within the ROI in PTW VeriSoft: Left-right profile of the photon measurement with the Ti-plan (left), target-gun profile of the proton measurement with the HU-plan (right).

2.5.4.4 Comparison of planned and actual line dose profiles

The last part of the film analysis consisted of calculating the means and standard deviations for each set of 3 to 5 films that were irradiated with the same treatment plan and extracting the desired horizontal and vertical line dose profiles. Hence, distinctive line doses were selected from the dose matrices of each of the set of films. In the photon beam experiments, the horizontal and vertical line doses were taken from as close to the isocenter of the ROI as possible.

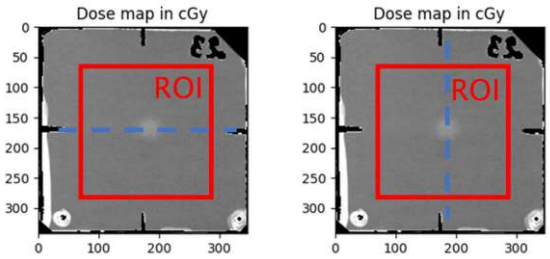

Fig. 2.19: Demonstration of the horizontal and vertical line dose profiles analyzed in the photon beam experiment.

For the proton beam experiment, the horizontal line was chosen to be as close to the isocenter as possible while the vertical line was placed slightly offset to the isocenter to look at the film region positioned behind the metal screw due to the chosen angle.
Once the positions of the line dose profiles were decided, the mean $\overline{D_{j,TP}}$ was determined by choosing the corresponding line and its two neighboring lines on both sides for each film and then calculating the mean over all the selected lines and films:

$$\overline{D_{j,TP}} = \frac{1}{5m} \sum_{k=1}^{m} \sum_{i=l-2}^{l+2} D_{ij,k} \tag{2.7}$$

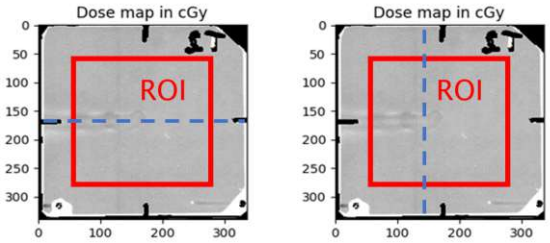

Fig. 2.20: Demonstration of the horizontal and vertical line dose profiles analyzed in the proton beam experiment.

with l being the index for the line of interest, $j = 1, ..., p$ the corresponding array (x-axis for the horizontal line, y-axis for the vertical line) and m the number of films irradiated with the selected treatment plan. In the next step, a sample standard deviation $\sigma_{j,TP}$ was calculated as follows:

$$\sigma_{j,TP} = \sqrt{\frac{\sum_{k=1}^{m} \sum_{i=l-2}^{l+2} (D_{ij,k} - \overline{D_{j,TP}})^2}{5m - 1}} \tag{2.8}$$

The result gives another array for the sample standard deviation for the m irradiatied films. Lastly, a CI of 95% was calculated for our small sample size ($n < 30$):

$$CI_j = D_j \pm 2.1 \cdot \frac{\sigma_j}{\sqrt{n}} \tag{2.9}$$

In this case, n is the sample size and varies between 15, 20 and 25 depending on the investigated number of radiochromic films (3, 4 or 5 films with 5 lines each).

For the treatment plans and MC simulations simply the lines of interest were selected since the resolutions of those plans were much lower than the resolutions of the radiochromic film measurements. However, the lines were interpolated to extend the 41 data points to 237 as present in the films. The results were compared graphically (see Sections 3.2.2 and 3.3.2). Furthermore, dose difference graphs between the treatment plans and measurements as well as MC simulations and measurements were calculated and plotted.

2.5.4.5 Dose verification

With the information of the planned doses from the planning system, the measured doses from the ionization chamber measurements, and the calculated reduced LINAC output on the measurement day (see Section 2.5.1), dose differences as well as corrected dose differences were calculated to compare the planned and measured doses.

The dose difference ΔD was calculated as follows:

$$\Delta D\ [\%] = \frac{(D_{plan} - D_{meas}) \cdot 100}{D_{plan}} \tag{2.10}$$

D_{plan} is the planned dose and $D_{measured}$ the measured dose. By considering the LINAC output dLO on the measurement day, the measured dose was corrected via

$$D_{meas,corr} = D_{meas} + D_{meas} \cdot dLO \tag{2.11}$$

A corrected dose difference ΔD_{corr} was then calculated using Equation 2.10 with the corrected measured dose $D_{meas,corr}$. Once all (corrected) dose differences were determined, the mean was then calculated from the irradiated films of each treatment plan (original, polystyrene, titanium) using $\bar{X} = \frac{1}{n}\sum_{i=1}^{n} X_i$ for n films. The results were presented in Table 3.1.

2.5.4.6 Evaluation of the reference film measurements

The reference film measurements from Section 2.5.2.1 were analyzed by first calculating the doses D of the individual films (as done in Section 2.5.4.2), then cutting out a ROI of 2.54×2.54 cm^2 in the center of each film and lastly calculating the mean

$$\overline{D} = \frac{1}{n^2} \sum_{i,j=1}^{n} D_{ij} \tag{2.12}$$

and the sample standard deviation

$$\sigma = \sqrt{\frac{\sum_{i,j=1}^{n}(D_{ij} - \overline{D})^2}{n^2 - 1}} \tag{2.13}$$

of an $n \times n$ matrix. The resulting mean and standard deviation at energies 6 MV FFF, 10 MV and 10 MV FFF were then graphically presented in Figure 3.10.

3 Results and Discussion

3.1 Scanner calibration

3.1.1 Calibration curve, residuals and calibration error

The results of the scanner calibration can be seen in Figs. 3.1 and 3.2 that show the calibration curve, residuals, and calibration errors of the scanned films from lot no. 11192002:

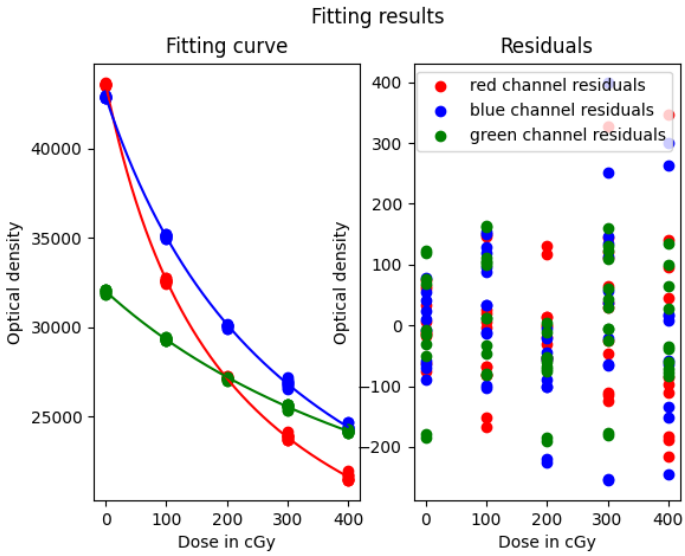

Fig. 3.1: Calibration curve with the three color channels red, green and blue calculated by using a rational function (left) and their residuals (right).

As indicated in Section 2.4.2, the red channel was chosen for dose conversion as it encompasses the maximum optical density range. The steepness of the function corresponds to enhanced sensitivity to irradiation [171], which is advantageous for measurements in the specified dose region. Deterministic functions of this nature may introduce systematic errors if the equation fails to accurately capture the physical characteristics of the film response or if an inadequate number of data points are utilized in the fitting process [99]. To mitigate this risk, a rational function coupled with many data points was used. The residuals appear to be randomly scattered without any discernible pattern, suggesting a satisfactory fit.

The calibration error plot in Fig. 3.2 shows the 10 to 12 data points per MU (each film was scanned twice):

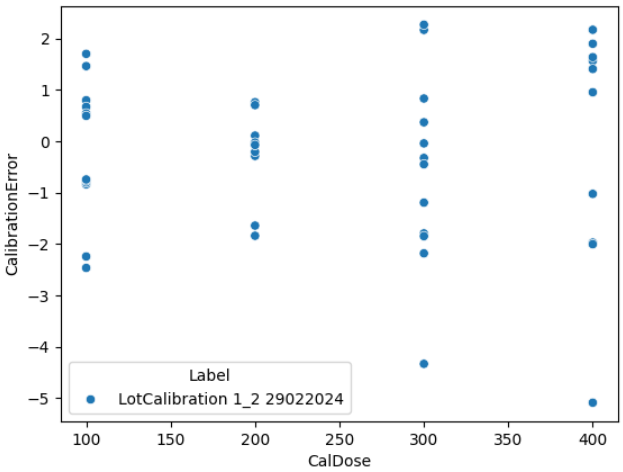

Fig. 3.2: Calibration error plot.

The mean calibration error lies at 0.3 % and the standard deviation at 1.7 %. The investigation conducted by Marroquin et al. [199] assessed the dose-response curves and the associated fitting procedure, identifying a dose uncertainty of 2.6 % when the red channel is utilized for reading EBT3 films within the irradiation range of 0 to 6 Gy. Similarly, Aldelaijan and Devic [200] confirmed a comparable outcome, indicating an uncertainty of less than 2 % for doses greater than 2 Gy. Consequently, the calibration procedure demonstrates fairly good results and indicates that the films do not vary strongly among each other. By obtaining the calibration curve, the relationship between the optical density (function of the wavelength at which the absorbance was sampled) and the dose was defined and used for the dose determination of all subsequent films of the same lot.

3.1.2 Lateral scanner artefacts

The row scans across the scanner surface are depicted in Fig. 3.3 for each MU. While the central line of the scanner surface shows hardly any deviation from the normalized pixel value 1, the scanner inhomogeneity increases in the lateral distance. The effect further intensifies with increasing MUs with the overall range lying between 0.87 and 1.01. These results coincide with previous studies that found deviations up to 15 % [201–209]. As all films in this thesis were scanned centrally in the same positions and only irradiated with 2 Gy (equaling 200 MUs), no correction was applied. However, if the effect plays a role in future scanning procedures correction matrices for different MUs can be calculated from the obtained data. One approach can be to interpolate the obtained normalized data

of the matrix and directly use it as a correction matrix where the corrected pixel data is the ratio of the scanned data and the correction factor at the given pixel position, as previously done by Ferreira et al. [201].

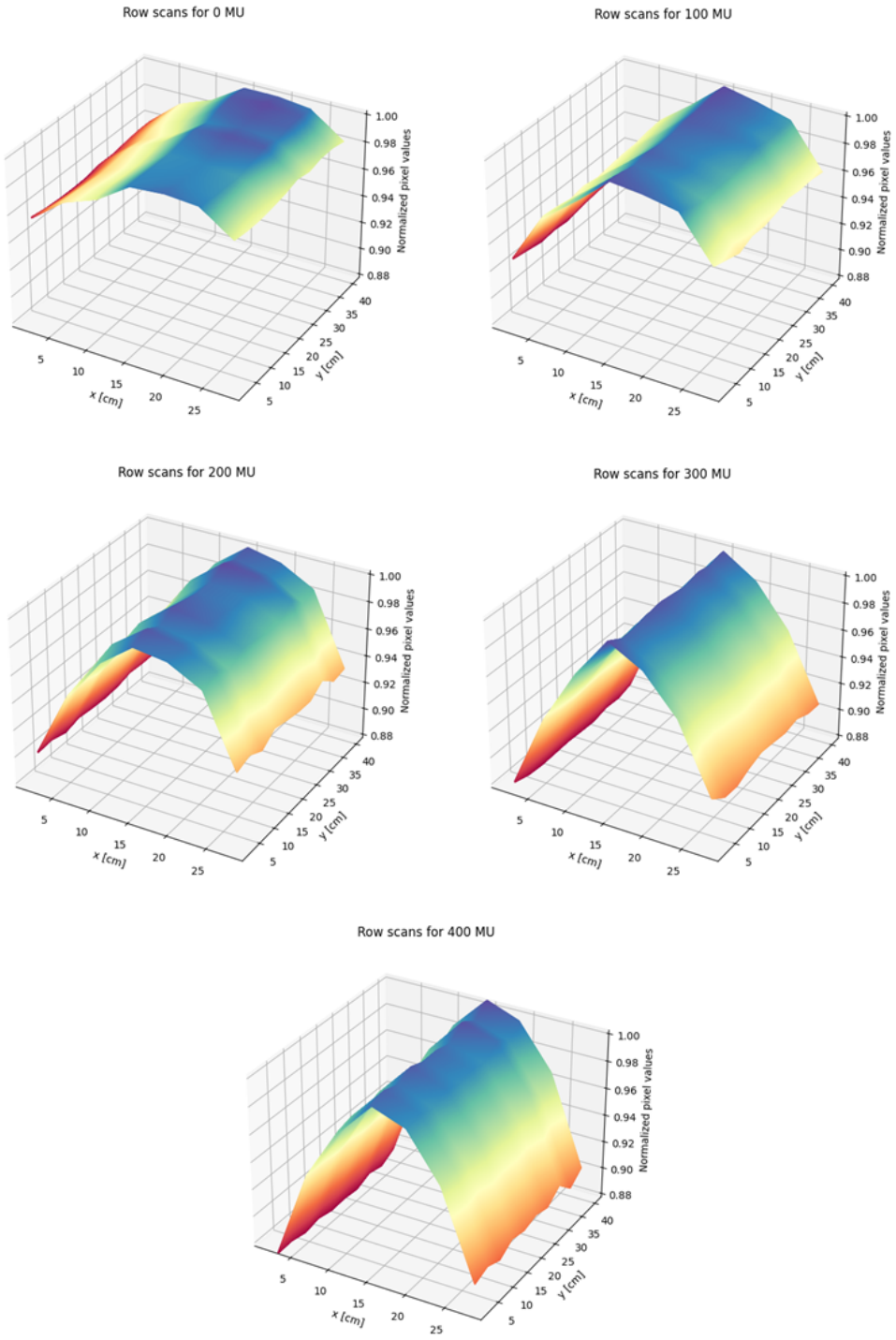

Fig. 3.3: Lateral scan artifacts seen in the row scans for 0 MU (top left), 100 MU (top right), 200 MU (middle left), 300 MU (middle right) and 400 MU (bottom).

3.2 Photon beam experiment

3.2.1 Film scans and gamma distributions

Graphic representations of the scanned radiochromic films after irradiation with the different RayStation plans can be viewed in Fig. 3.4. The film irradiated with the PS-plan is homogeneous, as a polystyrene insert was used here. Meanwhile, the films irradiated with the HU- and Ti-plans display a circular pattern in the center, which is where the film was sandwiched between the metal screw inserts. The pattern itself comes from the VMAT plan where the gantry rotates around the phantom during the irradiation process.

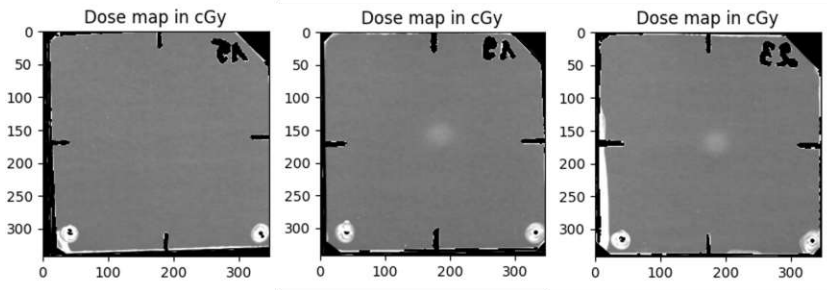

Fig. 3.4: Film scans of the photon beam experiments executed with the PS-plan (left), the HU-plan (middle) and the Ti-plan (right). The bottoms show the remaining holes, where the films were fixated in the phantom.

Gamma distributions can be seen in Fig. 3.5. The divergence of the actual dose deposition from the expected values of the RayStation plans is evident in the elevated gamma score observed at the location of the metallic screw. Additional deviations in the dose distribution can be identified at the base of the films. They are presumably due to damage sustained when fixating the films in the phantom.

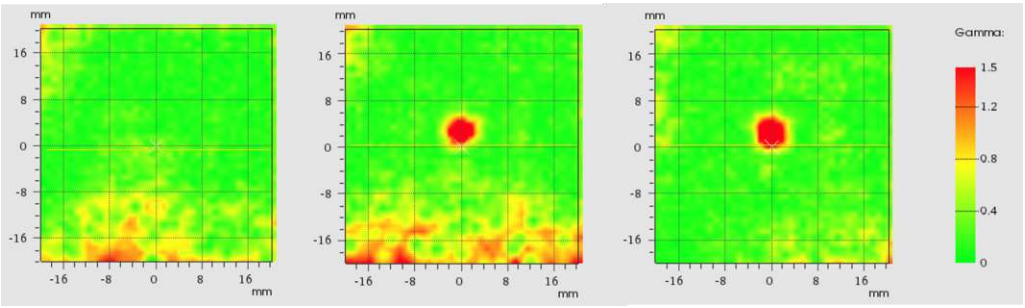

Fig. 3.5: Gamma distributions of the photon beam experiments executed with the PS-plan (left), the HU-plan (middle) and the Ti-plan (right) in the ROI and calculated in PTW VeriSoft.

3.2.2 Line dose profiles

All horizontal and vertical line dose profiles obtained from the 6 MV photon energy measurements are displayed in Fig. 3.6. Furthermore, a comparison of horizontal line dose profiles conducted at energies 6 MV, 6 MV FFF, 10 MV and 10 MV FFF can be found in Fig. 3.7.

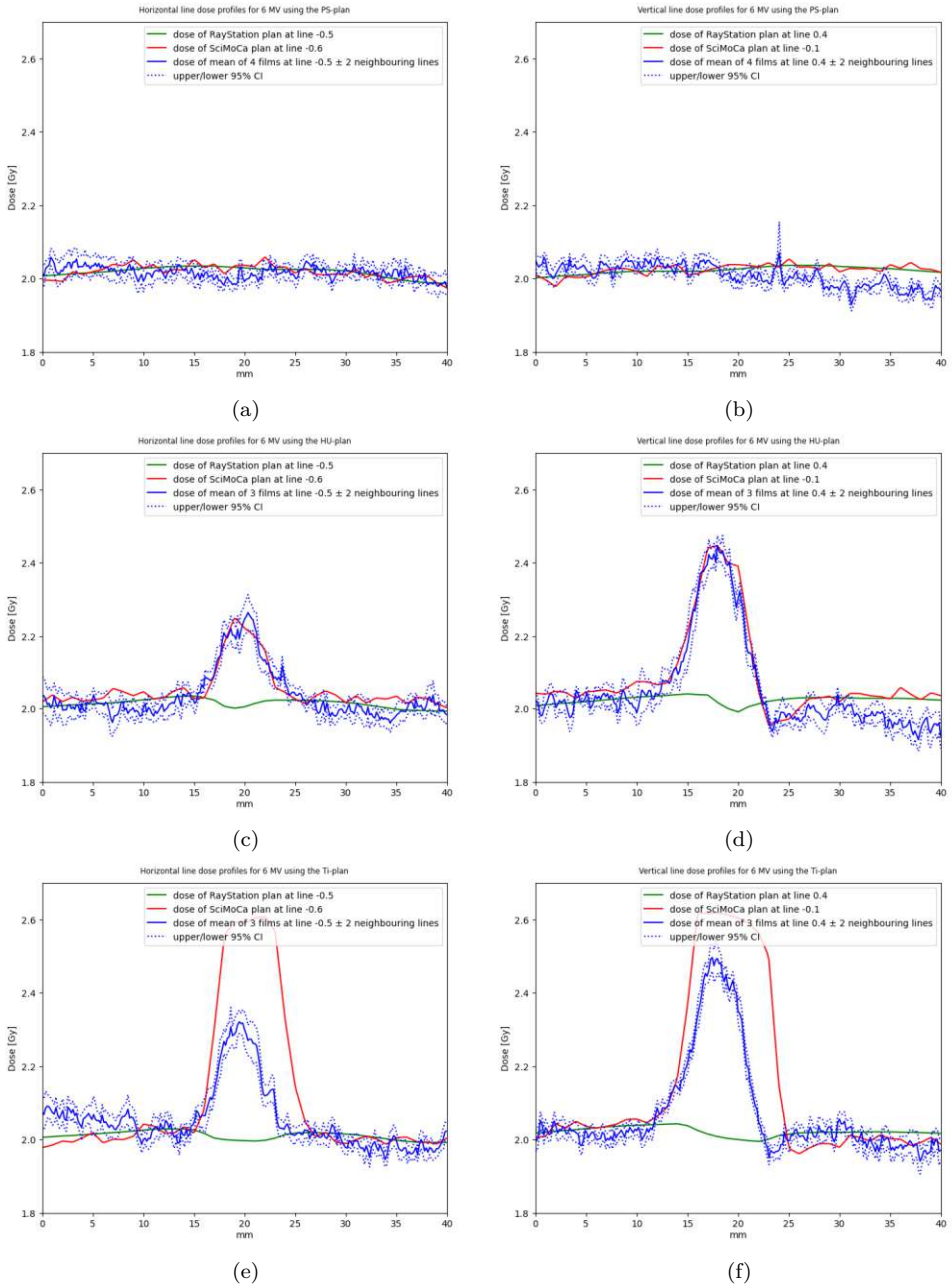

Fig. 3.6: Horizontal (left column) and vertical (right column) line dose profiles of the PS-plans ((a), (b)), the HU-plans ((c), (d)) and the Ti-plans ((e), (f)) at 6 MV energies with a 95 % CI.

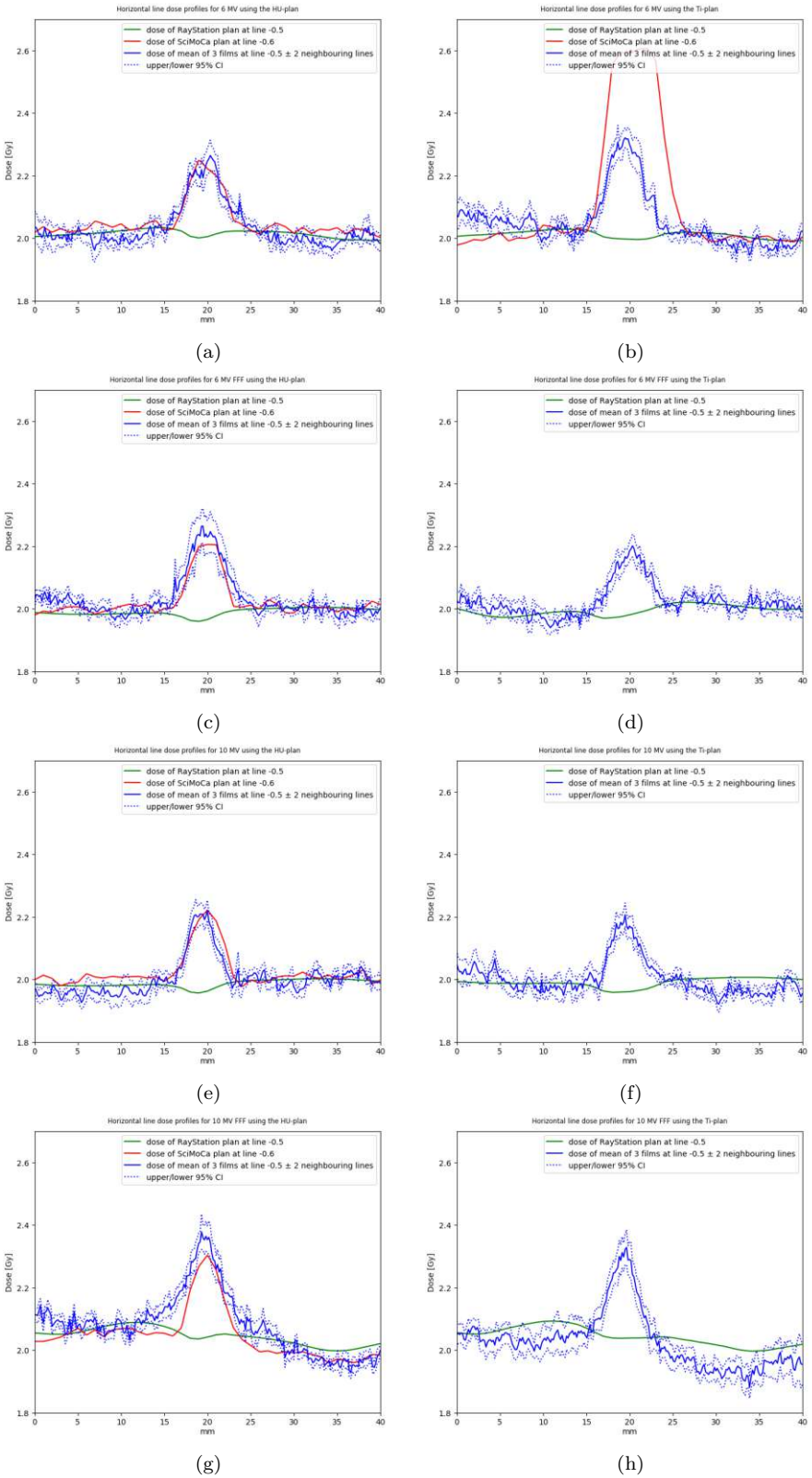

Fig. 3.7: Horizontal line dose profiles for the HU-plans (left column) and Ti-plans (right column) at energies 6 MV ((a), (b)), 6 MV FFF ((c), (d)), 10 MV ((e), (f)) and 10 MV FFF ((g), (h)).

The mean CI lies at 1.2 % for photon energies 6 MV, 6 MV FFF and 10 MV and at 1.4 % for 10 MV FFF. In Fig. 3.6 it can be seen that for the polystyrene measurements the measured doses (blue line) come very close to the doses predicted by the PS-plan (green line) and the MC simulations (red line). The slight deviations in the vertical line dose profiles of the PS and HU measurements are suspected to be subject to damages caused by the pins fixating the film at the bottom side. For the HU-plan, the influence of the titanium screw is very accurately simulated by the SciMoCa plan. Meanwhile, the RayStation plan assumes a rather homogeneous dose distribution. In case of the measurements conducted with the Ti-plan, MC simulations deviate again. This can be explained due to the fact, that for the HU-plan, the MC simulations perform independent calculations to ascertain the densities, while for the Ti-plan, the position and density of the metal screw is manually overwritten leading to erroneous predictions. Overall, the influence of the metal screw on the dose profile appears slightly stronger in the vertical line dose profiles than in the horizontal line dose profiles, due to the fact that the inserts are placed slightly above the isocenter from which the profiles where extracted. As for the horizontal line dose profile of the Ti-plan in Fig. 3.6, an underestimation of the dose was observed on the left side of the profile.

In Fig. 3.7, similar results were obtained independently of the energy and flattening filter settings. The slightly differing shapes of the horizontal line dose profiles observed exclusively at 10 MV FFF may be attributed to the stronger fluctuations in the LINAC at this particular energy setting.

In comparison with existing literature, analogous dose increases have been identified at the metal/tissue interface proximal to the beam source [138, 165, 180, 210, 211]. Pawalowski et al. [138] also analyzed dose distributions within various metal screws, including one composed of titanium, utilizing 6 MV photon beams with doses up to 5 Gy, and observed dose enhancements [138, 180]. Furthermore, Pawalowski et al. [138] and Ojala et al. [211] tested MC models in their studies and found high agreement between measurements with GafChromic EBT3 films and MC simulations, thus coinciding with the findings in this thesis.

3.2.3 Dose difference graphs

Dose differences between the three different plans calculated in RayStation and SciMoCa and the actual measurements are show. in Fig. 3.8 for 6 MV photon energies. Further comparison between the four energy settings is presented in Fig. 3.9.

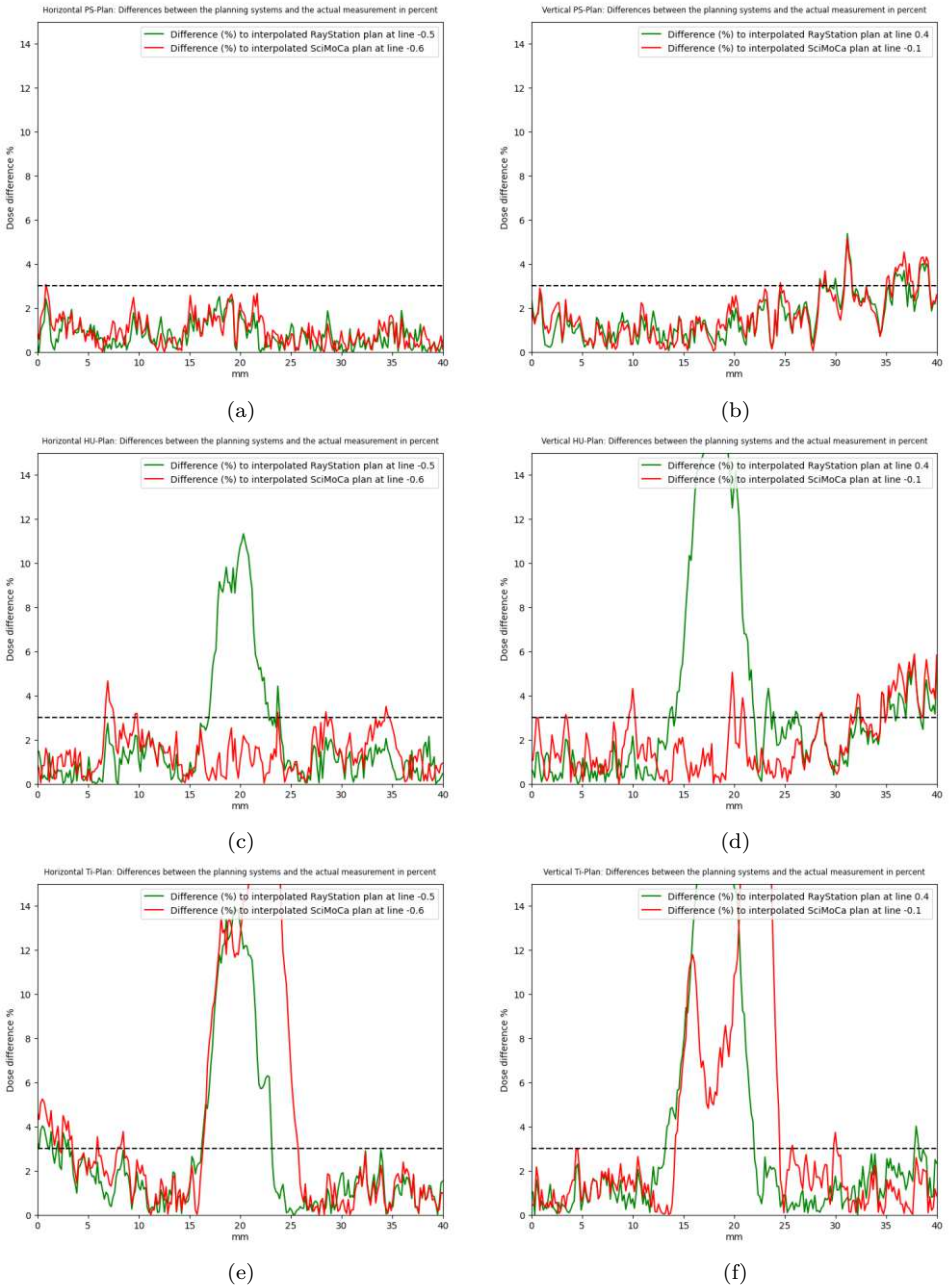

Fig. 3.8: Dose differences (%) between the RayStation and SciMoCa plans and the actual measurements for the horizontal line dose profiles (left column) and the vertical line dose profiles (right column) displaying the PS-plan ((a), (b)), HU-plan ((c), (d)) and Ti-plan ((e), (f)) in the 6 MV photon beam experiments.

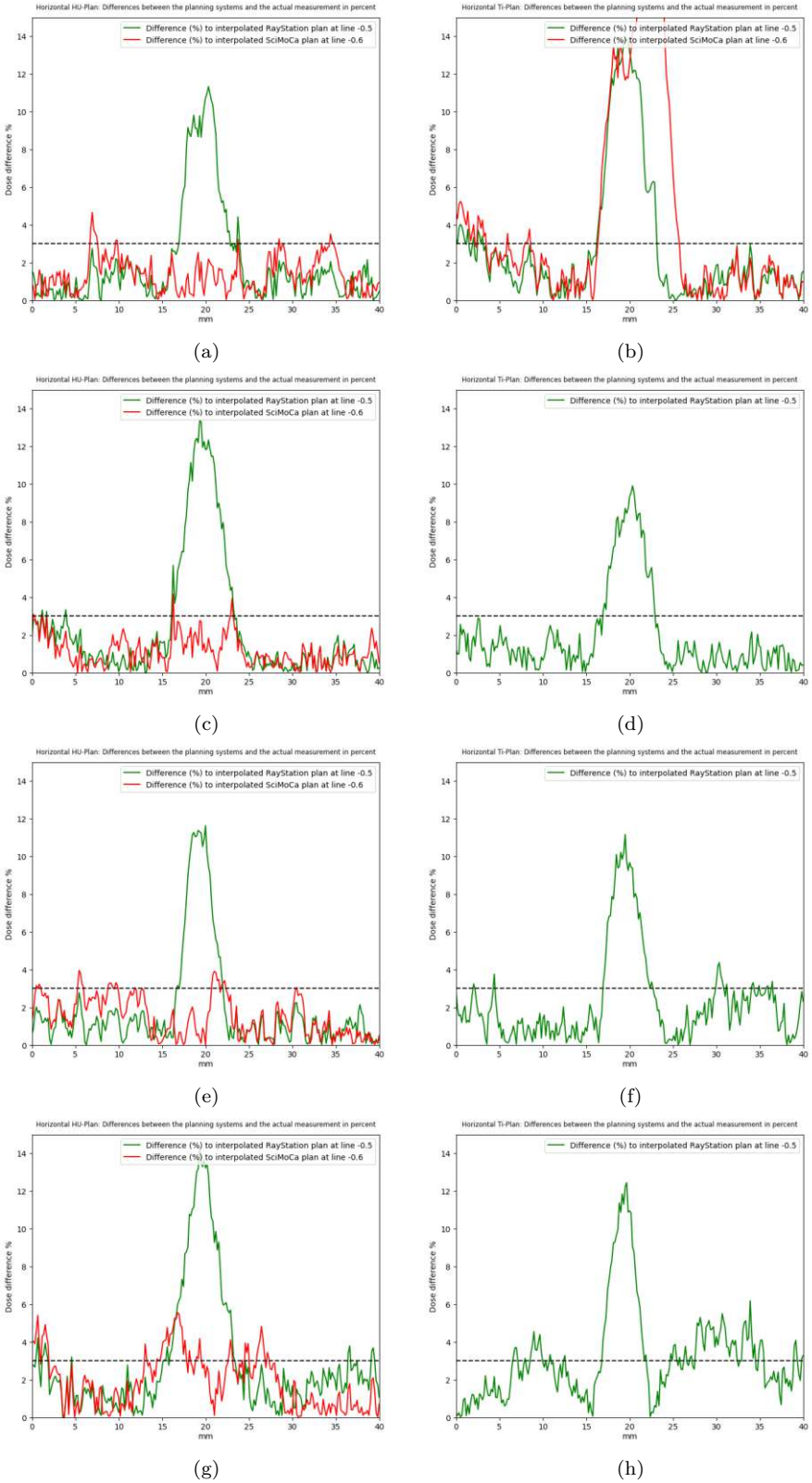

Fig. 3.9: Dose difference graphs for the HU-plan (left column) and Ti-plan (right column) at energies 6 MV ((a), (b)), 6 MV FFF ((c), (d)), 10 MV ((e), (f)) and 10 MV FFF ((g), (h)). The SciMoCa-plans (red lines) are partly included.

The graphs show a dashed line at the 3 % threshold, indicating minimal dose discrepancies and consequently positive outcomes. Exceedances may result from the titanium screw's impact, film defects caused during phantom fixation or beam fluctuations as discussed in the line dose profiles (see Section 3.2.2). For comparison, Kamomae et al. [210] reported dose enhancements of 10.4 % ± 8.1 % compared to the calculated dose when investigating a dental metallic crown with VMAT [180, 210]. The polystyrene measurements demonstrate substantial conformity within the horizontal line dose profile, suggesting that the planning systems accurately compute dose distributions. Near the titanium screw, RayStation plans and EBT3 film measurements show significant dose differences exceeding 10 %, as do SciMoCa plans in the Ti-plan experiments. In contrast, HU-plan MC simulations demonstrate close alignment with the film measurements with only an average dose difference of 1.7 %. By comparison, Ojala et al. [211] found even smaller differences between the measurements and the MC model of about 0.5 %.

3.2.4 Dose verification and reproducibility

Results for the dose verification conducted with the PTW semiflex 0.125 cm^3 ionization chamber (type 31010, serial no. 5866) during the photon beam experiments at energies 6 MV, 6 MV FFF and 10 MV are listed in Tab. 3.1:

Energy	Plan	Planned dose [Gy]	Measured dose [Gy]	Diff. [%]	Corr. dose [Gy]	Corr. diff. [%]
6 MV:	PS	2.031	2.017	0.7 %	2.025	0.3 %
0.4 % less	HU	2.038	2.011	1.3 %	2.019	1.0 %
LINAC output	Ti	2.032	2.014	0.9 %	2.022	0.5 %
6 MV FFF:	PS	2.058	2.049	0.4 %	2.055	0.1 %
0.3 % less	HU	2.052	2.036	0.8 %	2.042	0.5 %
LINAC output	Ti	2.060	2.040	1.0 %	2.046	0.7 %
10 MV:	PS	2.018	2.009	0.5 %	2.011	0.4 %
0.1 % less	HU	2.018	2.000	0.9 %	2.002	0.8 %
LINAC output	Ti	2.012	2.003	0.4 %	2.005	0.3 %

Tab. 3.1: (Corrected) dose differences [%] between the planned and measured doses, measured with the ionization chamber.

While uncorrected dose differences lie between 0.43 and 1.34 %, corrected differences only range from 0.14 to 0.95 %. As specified in the International Atomic Energy Agency (IAEA) TRS-398 [212], a standard uncertainty of approximately 1 % is anticipated under reference conditions when quantifying the absorbed dose in water. Despite the measurements being conducted under non-reference conditions, the results exhibit comparable accuracy. Consequently, the measurements obtained using the ionization chamber show a close

approximation to the planned doses, thereby facilitating effective verification. This is particularly significant given that the previously discussed line dose profiles were derived from normalized dose distributions. Lastly, the repeatedly successful verification measurements indicate great reproducibility for the experiments.

3.2.5 Reference film measurements

The doses resulting from the reference film measurements performed prior to the photon beam measurements can be seen in Fig. 3.10:

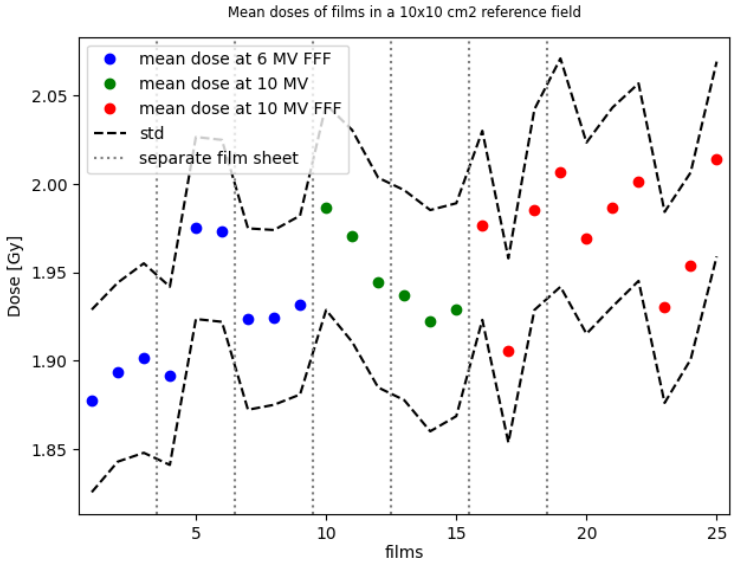

Fig. 3.10: Reference film measurements performed with films from different film sheets (dotted line) as well as various photon beam energies (different colors).

The measurements of the reference films exhibit a standard deviation of 2.8 %, indicated by the dashed line in Fig. 3.10. One interesting aspect of these measurements is that according to the user manual [171] slight variations in the active layer of the GafChromic EBT3 films are to be expected among different production lots. Yet, here all films were taken from the same lot and they still appear to have variability in the thickness of the active layer. Furthermore, even films cut out from the same film sheet show discrepancies in the measured dose. For the purpose of this thesis, this effect can be neglected as the dose distributions were normalized and re-calibrated in order to allow comparison with the TPS. However, in scenarios where normalization is not implemented or more sensitive experiments, such as those involving measurements in small fields where electronic disequilibrium occurs [213–215], are performed, these variations should not be disregarded. A viable approach to account for such non-uniformities would be to perform multichannel dosimetry incorporating all three color channels as previously performed by Micke et al. [100] with GafChromic EBT2 films.

3.3 Proton beam experiment

3.3.1 Film scans and gamma distributions

The scanning results of the radiochromic films irradiated with proton beams can be seen in Fig. 3.11. Here, the titanium screw left an imprint on the left side of the films irradiated with the HU- and Ti-plans as the proton beam came through a fixed beamline and the phantom was placed at a 20° table angle. Hence, the left part of the radiochromic film was positioned behind the screw causing the tail in the dose distribution.

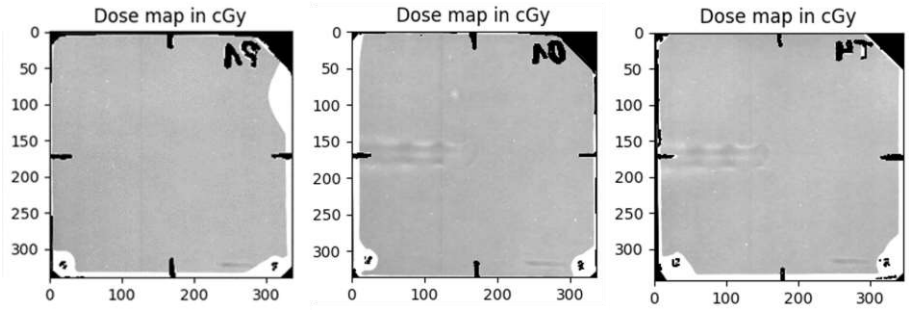

Fig. 3.11: Film scans of the proton beam experiment executed with the PS-plan (left), the HU-plan (middle) and the Ti-plan (right).

Examples for the gamma distributions of the proton beam experiments can be seen in Fig. 3.12. In case of the HU- and Ti-plan, isodose lines were added to better depict the influence of the titanium screw.

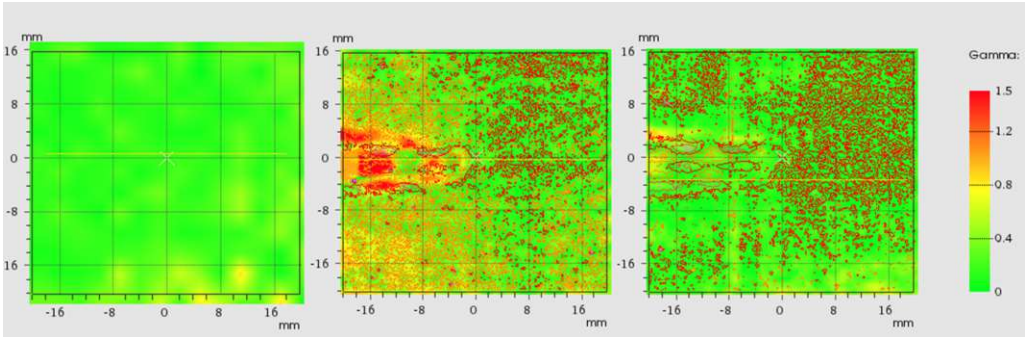

Fig. 3.12: Gamma distributions of the proton beam experiments executed with the PS-plan (left), the HU-plan (middle) and the Ti-plan (right) in the ROI and calculated in PTW VeriSoft. For the HU- and Ti-plan isodose lines were added.

3.3.2 Line dose profiles

Results for the horizontal and vertical line dose profiles with 95 % CI can be found in Fig. 3.13:

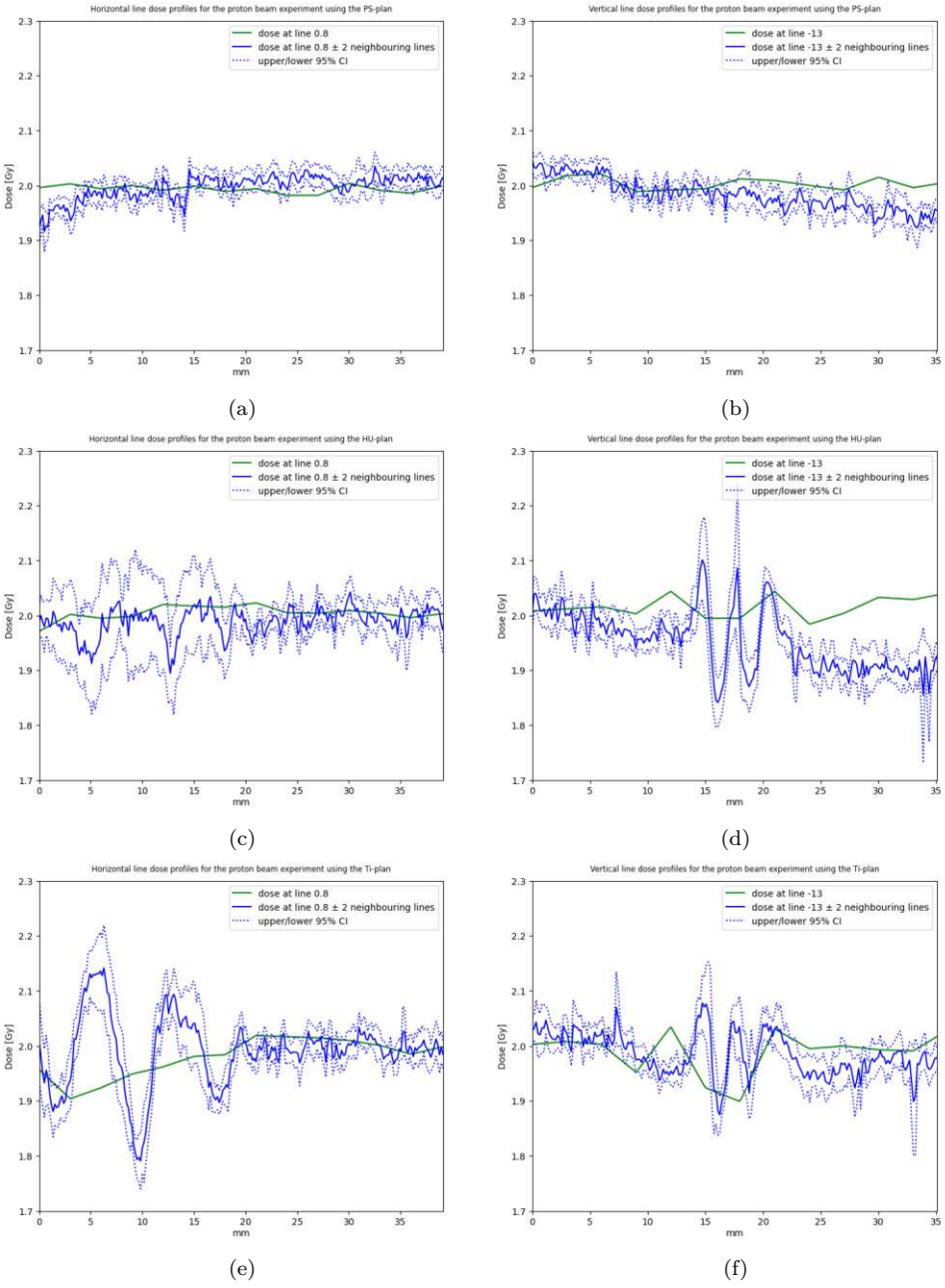

Fig. 3.13: Horizontal (left column) and vertical (right column) line dose profiles of the PS-plans ((a), (b), HU-plans ((c), (d)) and Ti-plans ((e), (f)) in the ROI for the proton beam experiments with a 95% CI.

Proton beam experiments exhibit an average CI of 1.6 %, which is slightly higher than in the photon beam experiments (see Section 3.2.2). The main differences in regards to the photon beam experiments are the fluctuations in the line dose profiles instead of dose

increases in the vicinity of the titanium screw. These fluctuations also stand in contrast with the study conducted by Jia et al. [216], who investigated a titanium spinal implant in a perpendicular beam setup. There, similarly to the vertical lines dose profiles in Fig. 2.20 ((d), (f)), the TPS estimated a dose reduction at the metal/tissue interface while expecting dose enhancements slightly outside the lateral edges. However, the measurements presented the opposite effect with dose enhancements of 8 % only at the interface, presumably due to secondary electron fluence perturbation [180, 216, 217]. Another study executed by Lin et al. [218] also reported dose enhancements of about 1 % in their study of a 0.6 mm titanium mesh implant, while at the same time exhibiting visible fluctuations caused by the mesh. Meanwhile, Oancea et al. [219] has reported additional dose enhancements at the edge [180, 219]. One possible explanation for the occuring fluctuations in this work is that, since the exact geometrical design of the screw thread was not implemented in the planning system [180], and , in contrast to the photon beam experiment, the proton beam exited a fixed horizontal beam line rather than rotating around the phantom, the geometrical influence is enhanced in the proton beam experiments, thus leading to this visible effect.

In the horizontal line dose profile of the experiments using the PS-plan, a decrease in dose can be found on the left side which represents the distal part of the film in the angular placement of the phantom. Lechner et al. [180] previously pointed out that this phenomenon coincides with existing reports (such as [173, 220, 221]) on quenching effects in GafChromic EBT3 films due to an increased LET in the distal area [180].

Interestingly, all the vertical line dose profiles exhibit a decrease of dose of approx. 5 %. This phenomenon was also previously examined by Lechner et al. [180], who referenced the research of Oancea et al. [219], indicating that when a proton beam interacts with a titanium target, it induces an angular distribution of nuclear interactions, consequently leading to a variance in dose orthogonal to the beam's trajectory [180, 219]. The effect could have further been pronounced by possible damages in the films due to the fixation process, as previously discussed in the photon beam experiments (see Section 3.2.2). In case of the fixation leading to a tilted insertion of the film into the phantom, the previously mentioned quenching effects might have also played a role in the vertical line dose profiles.

Lastly, Wang et al. [222] analyzed line dose profiles of the TPS at various depths both with and without material override. Their findings indicated that pronounced over- or underdosing occurred when material override was applied. Comparing the results to this work, a similar pattern is observed whereby the dose distribution derived from the RayStation planning with the Ti-plans demonstrates more significant over- or underdosing than when compared to the HU-plans.

3.3.3 Dose difference graphs

Dose difference graphs for the proton beam measurements are displayed in Fig. 3.14.

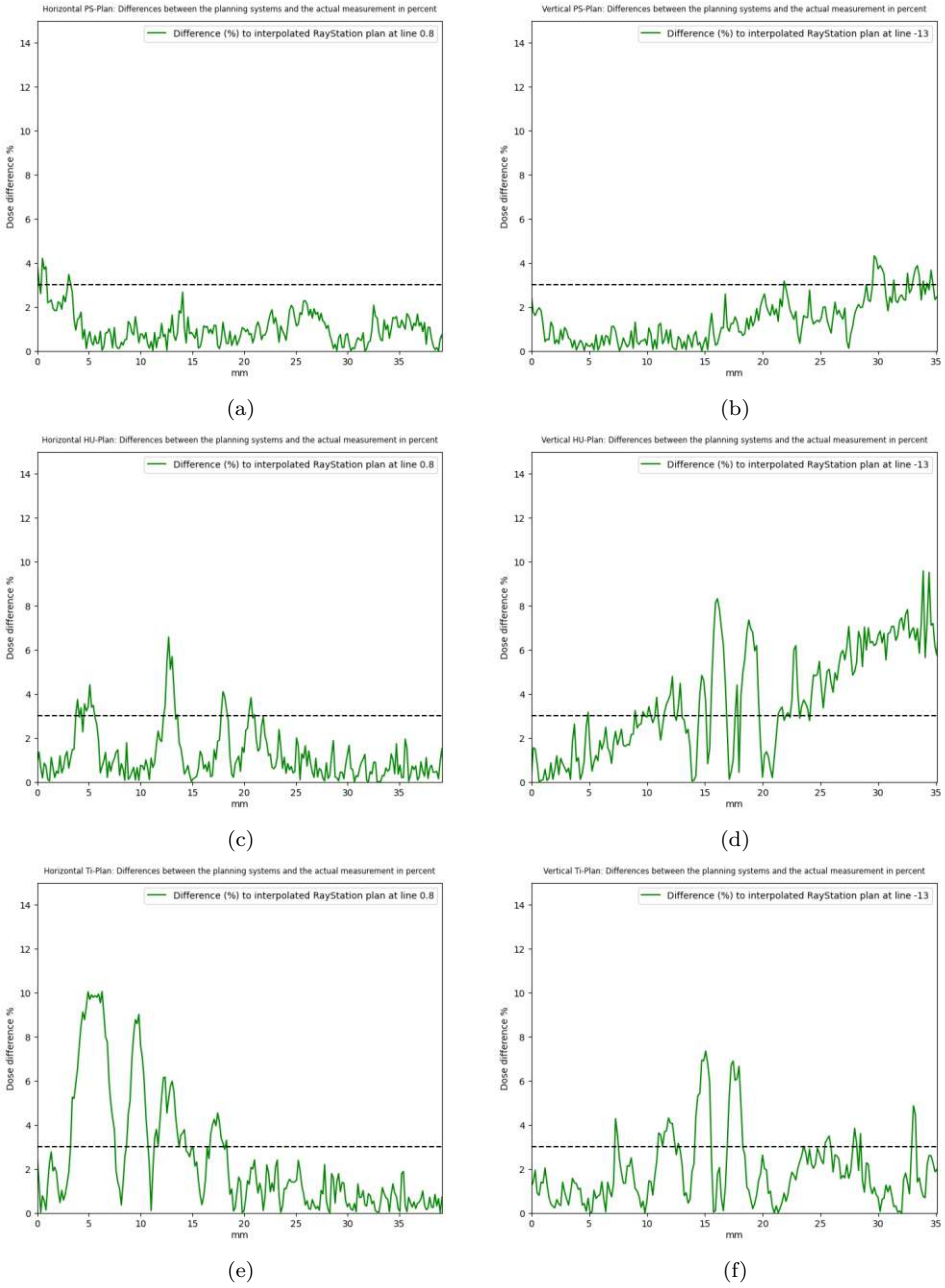

Fig. 3.14: Dose differences (%) between the RayStation plans and the actual measurements for the horizontal line dose profiles (left column) and the vertical line dose profiles (right column) displaying the PS-plan ((a), (b), HU-plan ((c), (d)) and Ti-plan ((e), (f) in the proton beam experiments.

Dose differences for the horizontal line dose profiles of the experiments conducted with the PS-plan show good results except for the areas where quenching effects are possible. Regions where the titanium screw was in close proximity to the film or sandwiched between the incident beam and film due to the angle of the phantom, dose fluctuations occur up to 10 %. Gradual divergence of the vertical dose differences across the film is particularly evident in the films irradiated with the HU-plan.

3.3.4 Dose verification

Dose verifications performed with the PTW semiflex 0.125 cm^3 ionization chamber (type 31010, serial no. 6012) are listed in Tab. 3.2:

Energy range	**Plan**	**Planned dose [Gy]**	**Measured dose [Gy]**	**Diff. [%]**
75-138 MeV	PS	2.018	2.038	-1.00%
	HU	2.013	2.019	-0.30%
	Ti	1.992	2.012	-1.00%

Tab. 3.2: Dose differences [%] between the planned doses and the doses measured with the PTW semiflex 0.125 cm^3 ionization chamber (type 31010, serial no. 6012).

In case of the proton beam experiments, the output of the beamline was not determined. Therefore, the resulting dose differences are not yet corrected for discrepancies in the particle beam output of the measurement day. Nevertheless, doses only deviate between 0.3 to 1.0 % from the planned dose, despite not being corrected. When Wang et al. [222] investigated neurosurgical cranial titanium mesh and screws, measurements with the ionization chamber also resulted in a maximum of 1.0 % dose differences between the measurements and the TPS calculation. Furthermore, according to the IAEA TRS-398 [212], a comparison with ionization chamber measurements at the reference depth in water for a clinical proton beam are estimated to exhibit an overall relative standard uncertainties of 1.7 to 2 % depending on the calibration, revealing that the observed measurements under non-reference conditions consistently demonstrate commendable accuracy. In contrast to the photon beam experiments, the planned doses in the proton beam experiments resulted in an underestimation of the dose. As mentioned in Section 3.2.4, the dose verification with an ionization chamber was an important step to compensate for the normalization of the line dose profiles and validate the experiments.

3.4 Limitations

This thesis notes several experimental limitations. Film calibration was completed for the current film lot, but future experiments with a new lot will require re-calibration. In the photon and proton beam experiments, the limited measurement time at MedAustron led to few measurements using only 3 to 5 films per treatment plan. An equivalent quantity of films was applied in the photon beam experiments. The higher resolution of the scanned films, relative to the treatment plans, was leveraged to attempt an increase in the data points available, thereby mitigating the impact of the small sample size. This methodology primarily affects the CI and it is acknowledged that an increased sample size would present a more optimal solution. Another constraint arose from conducting the proton beam experiments initially with a 20° table angle, which, upon subsequent photon beam experiments, was determined to pose a collision risk between the gantry and table. Consequently, the table angle was adjusted to 15° for the photon beam experiments, resulting in a slightly altered setup. Finally, this work examined only one configuration of pedicle screws. Given the variety of diameters, lengths, and thread geometries available for pedicle screws, further investigations are required to arrive at more comprehensive conclusions.

4 Conclusion and Outlook

This thesis examined the deposition of radiation doses at the interface of tissue and metal implants during a radiotherapy treatment. The experiments were conducted with three different RayStation treatment plans for photon and proton beams, respectively. The analysis employed radiochromic films, a phantom, and two film scanners, one of which underwent calibration specifically for this application.

The scanner calibration was successful. With the knowledge gained from the reference film measurements, it is advised to incorporate all color channels with multichannel dosimetry when investigating small fields to compensate for the non-uniformity of films in the same lot. Furthermore, a correction matrix can be calculated with the data obtained from the row scans to account for lateral scan artifacts in future scanning processes.

Photon beam experiments were verified with dose differences in the range of 0.1 to 1.0 % after LINAC output correction, while proton beam experiment verifications lay at 0.3 to 1.0 % dose differences (no output correction). The experimental results clearly exhibited the influence of the titanium screw. Strong fluctuations in the dose profiles may have their origins in the insufficient incorporation of the geometry of the screw thread in the planning process as well as the bottom of the radiochromic films being imbedded in the phantom using small screws, thus causing damage in that area. In terms of the polystyrene measurements conducted with the PS-plan, both the RayStation plans and the MC simulations show similarly good results giving validity to the execution of the experiment. When the metal screw is present, MC simulations come much closer to the actual dose profile than the RayStation planning system. This was especially seen in the HU-plan, where the MC simulation accounts for the titanium screw very accurately. Hence, MC showed to be a very reliable source in dose estimation.

With these results, the aim of this diploma thesis to improve our understanding of how the dose is deposited by photon and proton beams in tissue near a metal implant during radiotherapy treatment was met. In the future, this information will hopefully enhance radiotherapy treatments for patients with metal implants in clinical settings and serve as a stepping stone for further research with various constellations of metal implants.

Bibliography

[1] H.-Y. Lin and J. Y. Park. "Epidemiology of Cancer". In: *Anesthesia for Oncological Surgery*. Springer, 2024, pp. 11–16.

[2] F. Bray, M. Laversanne, H. Sung, J. Ferlay, R. L. Siegel, I. Soerjomataram, and A. Jemal. "Global cancer statistics 2022: GLOBOCAN estimates of incidence and mortality worldwide for 36 cancers in 185 countries". In: *CA: a cancer journal for clinicians* 74.3 (2024), pp. 229–263.

[3] F. Bray, M. Laversanne, E. Weiderpass, and I. Soerjomataram. "The ever-increasing importance of cancer as a leading cause of premature death worldwide". In: *Cancer* 127.16 (2021), pp. 3029–3030.

[4] F. Levi, F. Lucchini, E. Negri, P. Boyle, and C. La Vecchia. "Cancer mortality in Europe, 1990–1994, and an overview of trends from 1955 to 1994". In: *European Journal of Cancer* 35.10 (1999), pp. 1477–1516.

[5] J. E. Bennett, V. Kontis, C. D. Mathers, M. Guillot, J. Rehm, K. Chalkidou, A. P. Kengne, R. M. Carrillo-Larco, A. A. Bawah, K. Dain, et al. "NCD Countdown 2030: pathways to achieving Sustainable Development Goal target 3.4". In: *The Lancet* 396.10255 (2020), pp. 918–934.

[6] C. M. Siamof, S. Goel, and W. Cai. "Moving beyond the pillars of cancer treatment: perspectives from nanotechnology". In: *Frontiers in Chemistry* 8 (2020), p. 598100.

[7] L. Wang, C. Lynch, S. P. Pitroda, A. Piffkó, K. Yang, A. K. Huser, H. L. Liang, and R. R. Weichselbaum. "Radiotherapy and immunology". In: *Journal of Experimental Medicine* 221.7 (2024), e20232101.

[8] E. Evans and J. Staffurth. "Principles of cancer treatment by radiotherapy". In: *Surgery (Oxford)* 36.3 (2018), pp. 111–116.

[9] C. F. Dunne-Daly. "Principles of radiotherapy and radiobiology". In: *Seminars in oncology nursing*. Vol. 15. 4. Elsevier. 1999, pp. 250–259.

[10] D. A. Jaffray. "Image-guided radiotherapy: from current concept to future perspectives". In: *Nature reviews Clinical oncology* 9.12 (2012), pp. 688–699.

[11] V. Vassiliou and H. Charalambous. "Curative intent versus palliative intent radiation oncology". In: *Radiation Oncology in Palliative Cancer Care* (2013), pp. 31–42.

[12] W. R. Hendee and F. M. Edwards. “ALARA and an integrated approach to radiation protection”. In: *Seminars in nuclear medicine*. Vol. 16. 2. Elsevier. 1986, pp. 142–150.

[13] D. A. Jaffray, F. Knaul, M. Baumann, and M. Gospodarowicz. “Harnessing progress in radiotherapy for global cancer control”. In: *Nature Cancer* 4.9 (2023), pp. 1228–1238.

[14] J. Thariat, J.-M. Hannoun-Levi, A. Sun Myint, T. Vuong, and J.-P. Gérard. “Past, present, and future of radiotherapy for the benefit of patients”. In: *Nature reviews Clinical oncology* 10.1 (2013), pp. 52–60.

[15] W. Schäfer. “Uber eine neue Korperhohlenrontgenrohre zur Bestrahlung von Uterustumoren”. In: *Strahlentherapie* 44 (1932), pp. 283–292.

[16] E. B. Podgorsak. *Radiation oncology physics: a handbook for teachers and students*. 2005.

[17] C. Chargari, E. Deutsch, P. Blanchard, S. Gouy, H. Martelli, F. Guérin, I. Dumas, A. Bossi, P. Morice, A. N. Viswanathan, et al. “Brachytherapy: An overview for clinicians”. In: *CA: a cancer journal for clinicians* 69.5 (2019), pp. 386–401.

[18] D. G. Petereit, S. J. Frank, A. N. Viswanathan, B. Erickson, P. Eifel, P. L. Nguyen, and D. E. Wazer. “Brachytherapy: where has it gone?” In: *Journal of Clinical Oncology* 33.9 (2015), p. 980.

[19] N. F. Z. M. Khairi, N. F. Roszaini, and S. A. Othman. “Principles and Techniques in Handling Brachytherapy-A Short Review”. In: *Journal of Advanced Industrial Technology and Application* 4.1 (2023), pp. 75–79.

[20] M. F. L’Annunziata. “Introduction: radioactivity and our well-being”. In: *Radioactivity* (2007), pp. 1–45.

[21] H. Kim, C. J. Houser, R. Kalash, C. A. Maceil, B. Palestra, D. Malush, and S. Beriwal. “Workflow and efficiency in MRI-based high-dose-rate brachytherapy for cervical cancer in a high-volume brachytherapy center”. In: *Brachytherapy* 17.5 (2018), pp. 753–760.

[22] F. S. H. Abd, Z. A. Kadhum, F. A.-Z. H. Abd-Zaid, A. H. Aziz, and N. H. M. Murjan. “Radiation Therapy of Cancers, X-Ray Beams, Therapeutic Photon Beams, and Brachytherapy Application Techniques”. In: *Journal of Current Medical Research and Opinion* 7.06 (2024).

[23] A. C. Begg, F. A. Stewart, and C. Vens. “Strategies to improve radiotherapy with targeted drugs”. In: *Nature Reviews Cancer* 11.4 (2011), pp. 239–253.

[24] S. Bhide and C. Nutting. "Recent advances in radiotherapy". In: *BMC medicine* 8 (2010), pp. 1–5.

[25] C. R. Hansen, M. Hussein, U. Bernchou, R. Zukauskaite, and D. Thwaites. "Plan quality in radiotherapy treatment planning–Review of the factors and challenges". In: *Journal of Medical Imaging and Radiation Oncology* 66.2 (2022), pp. 267–278.

[26] A. Bertelsen, C. R. Hansen, J. Johansen, and C. Brink. "Single arc volumetric modulated arc therapy of head and neck cancer". In: *Radiotherapy and Oncology* 95.2 (2010), pp. 142–148.

[27] T. Wiezorek, T. Brachwitz, D. Georg, E. Blank, I. Fotina, G. Habl, M. Kretschmer, G. Lutters, H. Salz, K. Schubert, et al. "Rotational IMRT techniques compared to fixed gantry IMRT and tomotherapy: multi-institutional planning study for head-and-neck cases". In: *Radiation oncology* 6 (2011), pp. 1–10.

[28] F. M. Khan and J. P. Gibbons. *Khan's the physics of radiation therapy*. Lippincott Williams & Wilkins, 2014.

[29] S. Mehta, V. Suhag, M. Semwal, and N. Sharma. "Radiotherapy: basic concepts and recent advances". In: *Medical Journal Armed Forces India* 66.2 (2010), pp. 158–162.

[30] A. Joubert and N. Foray. "Intrinsic radiosensitivity and DNA double-strand breaks in human cells". In: *Cancer radiotherapie: journal de la Societe francaise de radiotherapie oncologique* 11.3 (2007), pp. 129–142.

[31] D. Y. Breitkreutz, M. D. Weil, and M. Bazalova-Carter. "External beam radiation therapy with kilovoltage x-rays". In: *Physica Medica* 79 (2020), pp. 103–112.

[32] W. Yeung, N. Luk, and K. Yu. "Current tools of radiation therapy in treatment of skin cancer". In: *Hong Kong J Dermatol Venereol* 17.2 (2009), pp. 79–86.

[33] D. De Ruysscher, G. Niedermann, N. G. Burnet, S. Siva, A. W. Lee, and F. Hegi-Johnson. "Radiotherapy toxicity". In: *Nature Reviews Disease Primers* 5.1 (2019), p. 13.

[34] S. Falk. "Principles of cancer treatment by radiotherapy". In: *Surgery (Oxford)* 27.4 (2009), pp. 169–172.

[35] O. M. P. LLC. *Introduction to Clinical Linear Accelerators*. `https://oncologymedicalphysics.com/introduction-to-clinical-linear-accelerators/`. accessed July 23, 2024.

[36] M. K. Tyler, P. Z. Liu, C. Lee, D. R. McKenzie, and N. Suchowerska. "Small field detector correction factors: effects of the flattening filter for Elekta and Varian linear accelerators". In: *Journal of Applied Clinical Medical Physics* 17.3 (2016), pp. 223–235.

[37] M. Dalaryd, G. Kragl, C. Ceberg, D. Georg, B. McClean, S. af Wetterstedt, E. Wieslander, and T. Knöös. "A Monte Carlo study of a flattening filter-free linear accelerator verified with measurements". In: *Physics in Medicine & Biology* 55.23 (2010), p. 7333.

[38] D. Georg, T. Knöös, and B. McClean. "Current status and future perspective of flattening filter free photon beams". In: *Medical physics* 38.3 (2011), pp. 1280–1293.

[39] P. O'Brien, B. Gillies, M. Schwartz, C. Young, and P. Davey. "Radiosurgery with unflattened 6-MV photon beams". In: *Medical physics* 18.3 (1991), pp. 519–521.

[40] O. N. Vassiliev, U. Titt, S. F. Kry, F. Pönisch, M. T. Gillin, and R. Mohan. "Monte Carlo study of photon fields from a flattening filter-free clinical accelerator". In: *Medical physics* 33.4 (2006), pp. 820–827.

[41] A. Ahnesjö and M. M. Aspradakis. "Dose calculations for external photon beams in radiotherapy". In: *Physics in Medicine & Biology* 44.11 (1999), R99.

[42] A. Ahnesjö, T. Knöös, and A. Montelius. "Application of the convolution method for calculation of output factors for therapy photon beams". In: *Medical physics* 19.2 (1992), pp. 295–301.

[43] M. Fippel, F. Haryanto, O. Dohm, F. Nüsslin, and S. Kriesen. "A virtual photon energy fluence model for Monte Carlo dose calculation". In: *Medical Physics* 30.3 (2003), pp. 301–311.

[44] D. Jaffray, J. Battista, A. Fenster, and P. Munro. "X-ray sources of medical linear accelerators: focal and extra-focal radiation". In: *Medical physics* 20.5 (1993), pp. 1417–1427.

[45] J. Olofsson, D. Georg, and M. Karlsson. "A widely tested model for head scatter influence on photon beam output". In: *Radiotherapy and oncology* 67.2 (2003), pp. 225–238.

[46] Y. Xiao, S. F. Kry, R. Popple, E. Yorke, N. Papanikolaou, S. Stathakis, P. Xia, S. Huq, J. Bayouth, J. Galvin, et al. "Flattening filter-free accelerators: a report from the AAPM Therapy Emerging Technology Assessment Work Group". In: *Journal of applied clinical medical physics* 16.3 (2015), pp. 12–29.

[47] E. Chaney, T. Cullip, and T. Gabriel. "A Monte Carlo study of accelerator head scatter". In: *Medical physics* 21.9 (1994), pp. 1383–1390.

[48] M. K. Fix, M. Stampanoni, P. Manser, E. J. Born, R. Mini, and P. Rüegsegger. "A multiple source model for 6 MV photon beam dose calculations using Monte Carlo". In: *Physics in Medicine & Biology* 46.5 (2001), p. 1407.

[49] S. Almberg, J. Frengen, and T. Lindmo. "Monte Carlo study of in-field and out-of-field dose distributions from a linear accelerator operating with and without a flattening-filter". In: *Medical physics* 39.8 (2012), pp. 5194–5203.

[50] S. F. Kry, O. N. Vassiliev, and R. Mohan. "Out-of-field photon dose following removal of the flattening filter from a medical accelerator". In: *Physics in Medicine & Biology* 55.8 (2010), p. 2155.

[51] J. Cashmore. "The characterization of unflattened photon beams from a 6 MV linear accelerator". In: *Physics in Medicine & Biology* 53.7 (2008), p. 1933.

[52] G. Kragl, S. af Wetterstedt, B. Knäusl, M. Lind, P. McCavana, T. Knöös, B. McClean, and D. Georg. "Dosimetric characteristics of 6 and 10 MV unflattened photon beams". In: *Radiotherapy and Oncology* 93.1 (2009), pp. 141–146.

[53] F. Pönisch, U. Titt, O. N. Vassiliev, S. F. Kry, and R. Mohan. "Properties of unflattened photon beams shaped by a multileaf collimator". In: *Medical physics* 33.6Part1 (2006), pp. 1738–1746.

[54] U. Titt, O. Vassiliev, F. Pönisch, L. Dong, H. Liu, and R. Mohan. "A flattening filter free photon treatment concept evaluation with Monte Carlo". In: *Medical physics* 33.6Part1 (2006), pp. 1595–1602.

[55] S. Stathakis, C. Esquivel, A. Gutierrez, C. R. Buckey, and N. Papanikolaou. "Treatment planning and delivery of IMRT using 6 and 18 MV photon beams without flattening filter". In: *Applied Radiation and Isotopes* 67.9 (2009), pp. 1629–1637.

[56] H. Tsujii, J. Mizoe, T. Kamada, M. Baba, H. Tsuji, H. Kato, S. Kato, S. Yamada, S. Yasuda, T. Ohno, et al. "Clinical results of carbon ion radiotherapy at NIRS". In: *Journal of radiation research* 48.Suppl_A (2007), A1–A13.

[57] H. Suit, M. Goitein, J. Munzenrider, L. Verhey, M. Urie, E. Gragoudas, A. Koehler, B. Gottschalk, J. Sisterson, and H. Tatsuzaki. "Increased efficacy of radiation therapy by use of proton beam." In: *Strahlentherapie und Onkologie: Organ der Deutschen Rontgengesellschaft...[et al]* 166.1 (1990), pp. 40–44.

[58] R. R. Wilson. "Radiological use of fast protons". In: *Radiology* 47.5 (1946), pp. 487–491.

[59] T. D. Malouff and D. M. Trifiletti. *Principles and practice of particle therapy*. John Wiley & Sons, 2022.

[60] V. I. Veksler. "New method for the acceleration of relativistic particles". In: *Doklady Akademii Nauk USSR*. Vol. 43. 8. 1944, pp. 346–348.

[61] E. M. McMillan. “The synchrotron—a proposed high energy particle accelerator”. In: *Physical Review* 68.5-6 (1945), p. 143.

[62] K. Endo, S. Fukumoro, K. Muto, T. Kitagawa, T. Inada, Y. Takada, A. Maruhashi, Y. Hayakawa, T. Arimoto, J. Tada, et al. “Medical Synchrotron for Proton Therapy”. In: *PROCEEDINGS OF EPAC*. Vol. 88. 1988, pp. 1459–1461.

[63] Z. Chen, M. M. Dominello, M. C. Joiner, and J. W. Burmeister. “Proton versus photon radiation therapy: A clinical review”. In: *Frontiers in Oncology* 13 (2023), p. 1133909.

[64] P. T. C.-O. G. (PTCOG). *Particle therapy facilities in operation*. https://www.ptcog.ch/index.php in-operation. accessed February 3, 2025.

[65] F. Noda, F. Ebina, H. Nishiuchi, T. Hae, M. Umezawa, S. Fujitaka, K. Saito, H. Akiyama, K. Hiramoto, and H. Works. “Conceptual design of carbon/proton synchrotron for particle beam therapy”. In: *Proceedings of the Particle Accelerator Conference,(Vancouver, Canada)*. 2009.

[66] M. Benedikt, J. Gutleber, U. Dorda, A. Fabich, M. Palm, and W. Pirkl. *Overview of the MedAustron design and technology choices*. Tech. rep. 2010.

[67] R. Mohan and D. Grosshans. “Proton therapy–present and future”. In: *Advanced drug delivery reviews* 109 (2017), pp. 26–44.

[68] M. Stock, D. Georg, A. Ableitinger, A. Zechner, A. Utz, M. Mumot, G. Kragl, J. Hopfgartner, J. Gora, T. Böhlen, et al. “The technological basis for adaptive ion beam therapy at MedAustron: status and outlook”. In: *Zeitschrift für Medizinische Physik* 28.3 (2018), pp. 196–210.

[69] J. Winiecki. “Principles of radiation therapy”. In: *Physical Sciences Reviews* 7.12 (2022), pp. 1501–1528.

[70] H. Krieger. *Grundlagen der Strahlungsphysik und des Strahlenschutzes*. Vol. 2. Springer, 2007.

[71] B. Gottschalk. “Radiotherapy proton interactions in matter”. In: *arXiv preprint arXiv:1804.00022* (2018).

[72] J. F. Janni. “Proton range-energy tables, 1 keV-10 GeV, energy loss, range, path length, time-of-flight, straggling, multiple scattering, and nuclear interaction probability. Part I. For 63 compounds”. In: *Atomic data and nuclear data tables* 27 (1982), p. 147.

[73] A. Hanson, L. Lanzl, E. Lyman, and M. Scott. “Measurement of multiple scattering of 15.7-MeV electrons”. In: *Physical Review* 84.4 (1951), p. 634.

[74] E. Pedroni, S. Scheib, T. Böhringer, A. Coray, M. Grossmann, S. Lin, and A. Lomax. "Experimental characterization and physical modelling of the dose distribution of scanned proton pencil beams". In: *Physics in Medicine & Biology* 50.3 (2005), p. 541.

[75] B. Gottschalk, E. W. Cascio, J. Daartz, and M. S. Wagner. "On the nuclear halo of a proton pencil beam stopping in water". In: *Physics in Medicine & Biology* 60.14 (2015), p. 5627.

[76] H. Suit. "Protons to replace photons in external beam radiation therapy?" In: *Clinical Oncology* 15.1 (2003), S29–S31.

[77] A. T. Berman, S. St. James, and R. Rengan. "Proton beam therapy for non-small cell lung cancer: current clinical evidence and future directions". In: *Cancers* 7.3 (2015), pp. 1178–1190.

[78] H. Paganetti and P. Van Luijk. "Biological considerations when comparing proton therapy with photon therapy". In: *Seminars in radiation oncology*. Vol. 23. 2. Elsevier. 2013, pp. 77–87.

[79] P. ICRU. "Recording, and ReportingProton-Beam Therapy (ICRU Report 78)". In: *Journal of the ICRU* 7 (2007).

[80] S. Gulliford and K. Prise. "Relative biological effect/linear energy transfer in proton beam therapy: a primer". In: *Clinical Oncology* (2019).

[81] T. Rivera-Montalvo. "Radiation therapy dosimetry system". In: *Applied Radiation and Isotopes* 83 (2014), pp. 204–209.

[82] S. Mishra and T. P. Selvam. "Radiation Dosimetry". In: *Handbook of Metrology and Applications*. Springer, 2023, pp. 1–26.

[83] C. E. De Almeida and C. Salata. "Absolute, reference, and relative dosimetry in radiotherapy". In: *Dosimetry*. IntechOpen, 2022.

[84] International Commission on Radiation Units and Measurements (ICRU). "Report 85: Fundamental Quantities and Units for Ionizing Radiation, 5. Dosimetry". In: *Journal of the ICRU* 11 (Apr. 2011), pp. 23–28. ISSN: 1473-6691, 1742-3422. DOI: 10.1093/jicru_ndr003. URL: https://dx.doi.org/10.1093/jicru_ndr003.

[85] W. H. Bragg. *Studies in radioactivity*. Macmillan, New York, 1910.

[86] L. H. Gray. "The absorption of penetrating radiation". In: *Proceedings of the Royal Society of London. Series A, Containing Papers of a Mathematical and Physical Character* 122.790 (1929), pp. 647–668.

[87] L. H. Gray. "An ionization method for the absolute measurement of γ-ray energy". In: *Proceedings of the Royal Society of London. Series A-Mathematical and Physical Sciences* 156.889 (1936), pp. 578–596.

[88] T. P. Selvam, V. Shrivastava, and A. Bakshi. "Monte Carlo calculation of Spencer-Attix and Bragg-Gray stopping-power ratios of tissue-to-air for ISO reference beta sources—an EGSnrc study". In: *Journal of Instrumentation* 16.03 (2021), P03006.

[89] F. H. Attix. *Introduction to radiological physics and radiation dosimetry*. Wiley, 1986.

[90] L. Spencer and F. H. Attix. "A theory of cavity ionization". In: *Radiation research* 3.3 (1955), pp. 239–254.

[91] F. H. Attix, L. DeLa Vergne, and V. H. Ritz. "Cavity ionization as a function of wall material". In: *Journal of Research of the National Bureau of Standards* 60.3 (1958), pp. 235–243.

[92] G. Pitchford. *Radiation Dosimetry: Electron Beams with Energies Between 1 and 50 MeV, in: ICRU Report 35, International Commission on Radiation Units and Measurements, Bethesda, Md.(1984)*. 1986.

[93] A. Nahum. "Water/air mass stopping power ratios for megavoltage photon and electron beams". In: *Physics in Medicine & Biology* 23.1 (1978), p. 24.

[94] R. Tino, A. Yeo, M. Leary, M. Brandt, and T. Kron. "A systematic review on 3D-printed imaging and dosimetry phantoms in radiation therapy". In: *Technology in cancer research & treatment* 18 (2019), p. 1533033819870208.

[95] P. Homolka, A. Gahleitner, M. Prokop, and R. Nowotny. "Optimization of the composition of phantom materials for computed tomography". In: *Physics in Medicine & Biology* 47.16 (2002), p. 2907.

[96] Y. Choi, K. J. Chun, J. Bahng, S. H. Choi, G. S. Cho, T. H. Kim, H. J. Yang, Y. C. Seo, and H.-T. Chung. "Development of a polystyrene phantom for quality assurance of a Gamma Knife®". In: *Nuclear Engineering and Technology* 55.8 (2023), pp. 2935–2940.

[97] H. Palmans, P. Andreo, M. S. Huq, J. Seuntjens, K. E. Christaki, and A. Meghzifene. "Dosimetry of small static fields used in external photon beam radiotherapy: summary of TRS-483, the IAEA–AAPM international Code of Practice for reference and relative dose determination". In: *Medical physics* 45.11 (2018), e1123–e1145.

[98] J. Seco, B. Clasie, and M. Partridge. "Review on the characteristics of radiation detectors for dosimetry and imaging". In: *Physics in Medicine & Biology* 59.20 (2014), R303.

[99] H. Bouchard, F. Lacroix, G. Beaudoin, J.-F. Carrier, and I. Kawrakow. "On the characterization and uncertainty analysis of radiochromic film dosimetry". In: *Medical physics* 36.6Part1 (2009), pp. 1931–1946.

[100] A. Micke, D. F. Lewis, and X. Yu. "Multichannel film dosimetry with nonuniformity correction". In: *Medical physics* 38.5 (2011), pp. 2523–2534.

[101] A. Niroomand-Rad, C. R. Blackwell, B. M. Coursey, K. P. Gall, J. M. Galvin, W. L. McLaughlin, A. S. Meigooni, R. Nath, J. E. Rodgers, and C. G. Soares. "Radiochromic film dosimetry: recommendations of AAPM radiation therapy committee task group 55". In: *Medical physics* 25.11 (1998), pp. 2093–2115.

[102] M. J. Butson, T. Cheung, and K. Peter. "Weak energy dependence of EBT gafchromic film dose response in the 50ákVp–10áMVp X-ray range". In: *Applied Radiation and Isotopes* 64.1 (2006), pp. 60–62.

[103] S.-T. Chiu-Tsao, Y. Ho, R. Shankar, L. Wang, and L. B. Harrison. "Energy dependence of response of new high sensitivity radiochromic films for megavoltage and kilovoltage radiation energies". In: *Medical Physics* 32.11 (2005), pp. 3350–3354.

[104] P. Lindsay, A. Rink, M. Ruschin, and D. Jaffray. "Investigation of energy dependence of EBT and EBT-2 Gafchromic film". In: *Medical physics* 37.2 (2010), pp. 571–576.

[105] P. Casolaro. "Radiochromic films for the two-dimensional dose distribution assessment". In: *Applied Sciences* 11.5 (2021), p. 2132.

[106] G. Gambarini, V. Regazzoni, E. Artuso, D. Giove, A. Mirandola, and M. Ciocca. "Measurements of 2D distributions of absorbed dose in protontherapy with Gafchromic EBT3 films". In: *Applied Radiation and Isotopes* 104 (2015), pp. 192–196.

[107] P. Sipilä, J. Ojala, S. Kaijaluoto, I. Jokelainen, and A. Kosunen. "Gafchromic EBT3 film dosimetry in electron beams—energy dependence and improved film read-out". In: *Journal of applied clinical medical physics* 17.1 (2016), pp. 360–373.

[108] V. C. Borca, M. Pasquino, G. Russo, P. Grosso, D. Cante, P. Sciacero, G. Girelli, M. R. L. Porta, and S. Tofani. "Dosimetric characterization and use of GAFCHROMIC EBT3 film for IMRT dose verification". In: *Journal of applied clinical medical physics* 14.2 (2013), pp. 158–171.

[109] A. Nobah, S. Aldelaijan, S. Devic, N. Tomic, J. Seuntjens, M. Al-Shabanah, and B. Moftah. "Radiochromic film based dosimetry of image-guidance procedures on different radiotherapy modalities". In: *Journal of applied clinical medical physics* 15.6 (2014), pp. 229–239.

[110] L. B. Leybovich, A. Sethi, and N. Dogan. “Comparison of ionization chambers of various volumes for IMRT absolute dose verification”. In: *Medical physics* 30.2 (2003), pp. 119–123.

[111] D. Verellen, N. Linthout, D. Van Den Berge, A. Bel, and G. Storme. “Initial experience with intensity-modulated conformal radiation therapy for treatment of the head and neck region”. In: *International Journal of Radiation Oncology* Biology* Physics* 39.1 (1997), pp. 99–114.

[112] D. Jen-San Tsai Ph, D. E. Wazer, M. N. Ling, J. K. Wu, M. Fagundes, T. DiPetrillo, B. Kramer, M. Koistinen, and M. J. Engler. “Dosimetric verification of the dynamic intensity-modulated radiation therapy of 92 patients”. In: *International Journal of Radiation Oncology* Biology* Physics* 40.5 (1998), pp. 1213–1230.

[113] D. A. Low, R. L. Gerber, S. Mutic, and J. A. Purdy. “Phantoms for IMRT dose distribution measurement and treatment verification”. In: *International Journal of Radiation Oncology* Biology* Physics* 40.5 (1998), pp. 1231–1235.

[114] D. A. Low, K. C. Chao, S. Mutic, R. L. Gerber, C. A. Perez, and J. A. Purdy. “Quality assurance of serial tomotherapy for head and neck patient treatments”. In: *International Journal of Radiation Oncology* Biology* Physics* 42.3 (1998), pp. 681–692.

[115] D. A. Low, S. Mutic, J. F. Dempsey, R. L. Gerber, W. R. Bosch, C. A. Perez, and J. A. Purdy. “Quantitative dosimetric verification of an IMRT planning and delivery system”. In: *Radiotherapy and oncology* 49.3 (1998), pp. 305–316.

[116] A. Solimanian and M. Ghafoori. “Standard calibration of ionization chambers used in radiation therapy dosimetry and evaluation of uncertainties”. In: (2010).

[117] M. D. Evans et al. “Computerized treatment planning systems for external photon beam radiotherapy”. In: *International Atomic Energy Agency Publication. Montreal, Quebec, Canada* (2006), pp. 387–406.

[118] R. S. Khandpur. *Compendium of Biomedical Instrumentation, 3 Volume Set*. John Wiley & Sons, 2020.

[119] K. Balaji, B. Subramanian, P. Yadav, C. A. Radha, and V. Ramasubramanian. “Radiation therapy for breast cancer: Literature review”. In: *Medical Dosimetry* 41.3 (2016), pp. 253–257.

[120] J. Van der Veen and S. Nuyts. “Can intensity-modulated-radiotherapy reduce toxicity in head and neck squamous cell carcinoma?” In: *Cancers* 9.10 (2017), p. 135.

[121] A. P. Abernethy, L. M. Etheredge, P. A. Ganz, P. Wallace, R. R. German, C. Neti, P. B. Bach, and S. B. Murphy. "Rapid-learning system for cancer care". In: *Journal of Clinical Oncology* 28.27 (2010), pp. 4268–4274.

[122] J. P. Tol, M. Dahele, A. R. Delaney, B. J. Slotman, and W. F. Verbakel. "Can knowledge-based DVH predictions be used for automated, individualized quality assurance of radiotherapy treatment plans?" In: *Radiation Oncology* 10 (2015), pp. 1–14.

[123] J. P. Tol, A. R. Delaney, M. Dahele, B. J. Slotman, and W. F. Verbakel. "Evaluation of a knowledge-based planning solution for head and neck cancer". In: *International Journal of Radiation Oncology* Biology* Physics* 91.3 (2015), pp. 612–620.

[124] A. Fogliata, F. Belosi, A. Clivio, P. Navarria, G. Nicolini, M. Scorsetti, E. Vanetti, and L. Cozzi. "On the pre-clinical validation of a commercial model-based optimisation engine: application to volumetric modulated arc therapy for patients with lung or prostate cancer". In: *Radiotherapy and Oncology* 113.3 (2014), pp. 385–391.

[125] C. R. Hansen, A. Bertelsen, I. Hazell, R. Zukauskaite, N. Gyldenkerne, J. Johansen, J. G. Eriksen, and C. Brink. "Automatic treatment planning improves the clinical quality of head and neck cancer treatment plans". In: *Clinical and translational radiation oncology* 1 (2016), pp. 2–8.

[126] I. Hazell, K. Bzdusek, P. Kumar, C. R. Hansen, A. Bertelsen, J. G. Eriksen, J. Johansen, and C. Brink. "Automatic planning of head and neck treatment plans". In: *Journal of applied clinical medical physics* 17.1 (2016), pp. 272–282.

[127] R. N. Kandalan, D. Nguyen, N. H. Rezaeian, A. M. Barragán-Montero, S. Breedveld, K. Namuduri, S. Jiang, and M.-H. Lin. "Dose prediction with deep learning for prostate cancer radiation therapy: model adaptation to different treatment planning practices". In: *Radiotherapy and Oncology* 153 (2020), pp. 228–235.

[128] X. Bai, B. Wang, S. Wang, Z. Wu, C. Gou, and Q. Hou. "Radiotherapy dose distribution prediction for breast cancer using deformable image registration". In: *BioMedical Engineering OnLine* 19.1 (2020), p. 39.

[129] S. Ahmed, B. Nelms, D. Gintz, J. Caudell, G. Zhang, E. G. Moros, and V. Feygelman. "A method for a priori estimation of best feasible DVH for organs-at-risk: validation for head and neck VMAT planning". In: *Medical physics* 44.10 (2017), pp. 5486–5497.

[130] D. Jaffray and J. Siewerdsen. "Cone-beam computed tomography with a flat-panel imager: initial performance characterization". In: *Medical physics* 27.6 (2000), pp. 1311–1323.

[131] "Prescribing, recording, and reporting photon-beam intensity-modulated radiation therapy (IMRT)". en. In: *J. ICRU* 10.1 (Apr. 2010), pp. 1–3.

[132] R. L. AB. *VMAT OPTIMIZATION IN RAYSTATION*. "https://www.raysearchlabs.com/siteassets/about-overview/media-center/wp-re-ev-n-pdfs/white-papers/white-paper-3---vmat-aug-20152.pdf". accessed October 31, 2024.

[133] O. M. P. LLC. *Treatment Planning System Basics*. https://oncologymedicalphysics.com/introduction-to-treatment-planning-systems/. accessed October 31, 2024.

[134] D. G. Kovacs, L. A. Rechner, A. L. Appelt, A. K. Berthelsen, J. C. Costa, J. Friborg, G. F. Persson, J. P. Bangsgaard, L. Specht, and M. C. Aznar. "Metal artefact reduction for accurate tumour delineation in radiotherapy". In: *Radiotherapy and Oncology* 126.3 (2018), pp. 479–486.

[135] A. Bujold, T. Craig, D. Jaffray, and L. A. Dawson. "Image-guided radiotherapy: has it influenced patient outcomes?" In: *Seminars in radiation oncology*. Vol. 22. 1. Elsevier. 2012, pp. 50–61.

[136] A. Rousselle, A. Amelot, J. Thariat, J. Jacob, G. Mercy, L. De Marzi, and L. Feuvret. "Metallic implants and CT artefacts in the CTV area: Where are we in 2020?" In: *Cancer/Radiothérapie* 24.6-7 (2020), pp. 658–666.

[137] D. Giantsoudi, B. De Man, J. Verburg, A. Trofimov, Y. Jin, G. Wang, L. Gjesteby, and H. Paganetti. "Metal artifacts in computed tomography for radiation therapy planning: dosimetric effects and impact of metal artifact reduction". In: *Physics in Medicine & Biology* 62.8 (2017), R49.

[138] B. Pawałowski, A. Ryczkowski, R. Panek, U. Sobocka-Kurdyk, K. Graczyk, and T. Piotrowski. "Accuracy of the doses computed by the Eclipse treatment planning system near and inside metal elements". In: *Scientific reports* 12.1 (2022), p. 5974.

[139] J. F. Barrett and N. Keat. "Artifacts in CT: recognition and avoidance". In: *Radiographics* 24.6 (2004), pp. 1679–1691.

[140] M. N. Bongers, C. Schabel, C. Thomas, R. Raupach, M. Notohamiprodjo, K. Nikolaou, and F. Bamberg. "Comparison and combination of dual-energy-and iterative-based metal artefact reduction on hip prosthesis and dental implants". In: *PLoS One* 10.11 (2015), e0143584.

[141] M.-J. Lee, S. Kim, S.-A. Lee, H.-T. Song, Y.-M. Huh, D.-H. Kim, S. H. Han, and J.-S. Suh. "Overcoming artifacts from metallic orthopedic implants at high-field-strength MR imaging and multi-detector CT". In: *Radiographics* 27.3 (2007), pp. 791–803.

[142] O. Jäkel and P. Reiss. "The influence of metal artefacts on the range of ion beams". In: *Physics in Medicine & Biology* 52.3 (2007), p. 635.

[143] Y. Rong, P. Yadav, B. Paliwal, L. Shang, and J. S. Welsh. "A planning study for palliative spine treatment using StatRT and megavoltage CT simulation". In: *Journal of applied clinical medical physics* 12.1 (2011), pp. 97–107.

[144] S. Hernandez, C. Sjogreen, S. S. Gay, C. Nguyen, T. Netherton, A. Olanrewaju, L. J. Zhang, D. J. Rhee, J. D. Méndez, L. E. Court, et al. "Development and dosimetric assessment of an automatic dental artifact classification tool to guide artifact management techniques in a fully automated treatment planning workflow". In: *Computerized Medical Imaging and Graphics* 90 (2021), p. 101907.

[145] W. D. Newhauser, A. Giebeler, K. M. Langen, D. Mirkovic, and R. Mohan. "Can megavoltage computed tomography reduce proton range uncertainties in treatment plans for patients with large metal implants?" In: *Physics in Medicine & Biology* 53.9 (2008), p. 2327.

[146] G. Wang, T. Frei, and M. W. Vannier. "Fast iterative algorithm for metal artifact reduction in X-ray CT". In: *Academic radiology* 7.8 (2000), pp. 607–614.

[147] B. De Man, J. Nuyts, P. Dupont, G. Marchal, and P. Suetens. "An iterative maximum-likelihood polychromatic algorithm for CT". In: *IEEE transactions on medical imaging* 20.10 (2001), pp. 999–1008.

[148] J. Wei, G. A. Sandison, W.-C. Hsi, M. Ringor, and X. Lu. "Dosimetric impact of a CT metal artefact suppression algorithm for proton, electron and photon therapies". In: *Physics in Medicine & Biology* 51.20 (2006), p. 5183.

[149] Y. Zhang, L. Zhang, X. R. Zhu, A. K. Lee, M. Chambers, and L. Dong. "Reducing metal artifacts in cone-beam CT images by preprocessing projection data". In: *International Journal of Radiation Oncology* Biology* Physics* 67.3 (2007), pp. 924–932.

[150] E. Meyer, R. Raupach, M. Lell, B. Schmidt, and M. Kachelrieß. "Normalized metal artifact reduction (NMAR) in computed tomography". In: *Medical physics* 37.10 (2010), pp. 5482–5493.

[151] E. Meyer, R. Raupach, M. Lell, B. Schmidt, and M. Kachelrieß. "Frequency split metal artifact reduction (FSMAR) in computed tomography". In: *Medical physics* 39.4 (2012), pp. 1904–1916.

[152] M. Lell, E. Meyer, M. Schmid, R. Raupach, M. May, M. Uder, and M. Kachelriess. "Frequency split metal artefact reduction in pelvic computed tomography". In: *European radiology* 23 (2013), pp. 2137–2145.

[153] F. Bamberg, A. Dierks, K. Nikolaou, M. F. Reiser, C. R. Becker, and T. R. Johnson. "Metal artifact reduction by dual energy computed tomography using monoenergetic extrapolation". In: *European radiology* 21 (2011), pp. 1424–1429.

[154] Y. Wang, B. Qian, B. Li, G. Qin, Z. Zhou, Y. Qiu, X. Sun, and B. Zhu. "Metal artifacts reduction using monochromatic images from spectral CT: evaluation of pedicle screws in patients with scoliosis". In: *European journal of radiology* 82.8 (2013), e360–e366.

[155] C. Zhou, Y. E. Zhao, S. Luo, H. Shi, L. Zheng, L. J. Zhang, G. Lu, et al. "Monoenergetic imaging of dual-energy CT reduces artifacts from implanted metal orthopedic devices in patients with factures". In: *Academic radiology* 18.10 (2011), pp. 1252–1257.

[156] L. Yu, S. Leng, and C. H. McCollough. "Dual-energy CT–based monochromatic imaging". In: *American journal of Roentgenology* 199.5_supplement (2012), S9–S15.

[157] Y.-l. He, D.-m. Zhang, H.-d. Xue, and Z.-y. Jin. "Clinical value of dual-energy CT in detection of pancreatic adenocarcinoma: investigation of the best pancreatic tumor contrast to noise ratio". In: *Chinese Medical Sciences Journal* 27.4 (2012), pp. 207–212.

[158] M. H. Albrecht, J.-E. Scholtz, J. Kraft, R. W. Bauer, M. Kaup, P. Dewes, A. M. Bucher, I. Burck, J. Wagenblast, T. Lehnert, et al. "Assessment of an advanced monoenergetic reconstruction technique in dual-energy computed tomography of head and neck cancer". In: *European radiology* 25 (2015), pp. 2493–2501.

[159] M. Maerz, P. Mittermair, A. Krauss, O. Koelbl, and B. Dobler. "Iterative metal artifact reduction improves dose calculation accuracy : Phantom study with dental implants". en. In: *Strahlenther. Onkol.* 192.6 (June 2016), pp. 403–413.

[160] Y. Kim, W. A. Tomé, M. Bal, T. R. McNutt, and L. Spies. "The impact of dental metal artifacts on head and neck IMRT dose distributions". In: *Radiotherapy and oncology* 79.2 (2006), pp. 198–202.

[161] M. Maerz, O. Koelbl, and B. Dobler. "Influence of metallic dental implants and metal artefacts on dose calculation accuracy". In: *Strahlentherapie und Onkologie* 191.3 (Oct. 2014), pp. 234–241. ISSN: 1439-099X. DOI: 10.1007/s00066-014-0774-2. URL: http://dx.doi.org/10.1007/s00066-014-0774-2.

[162] M. F. Spadea, J. M. Verburg, G. Baroni, and J. Seco. "The impact of low-Z and high-Z metal implants in IMRT: a Monte Carlo study of dose inaccuracies in commercial dose algorithms". In: *Medical physics* 41.1 (2014), p. 011702.

[163] G. J. Webster, C. G. Rowbottom, and R. I. Mackay. "Evaluation of the impact of dental artefacts on intensity-modulated radiotherapy planning for the head and neck". In: *Radiotherapy and Oncology* 93.3 (2009), pp. 553–558.

[164] N. Mail, Y. Albarakati, M. Ahmad Khan, F. Saeedi, N. Safadi, S. Al-Ghamdi, and A. Saoudi. "The impacts of dental filling materials on RapidArc treatment planning and dose delivery: challenges and solution". In: *Medical physics* 40.8 (2013), p. 081714.

[165] J. Y. Huang, D. S. Followill, R. M. Howell, X. Liu, D. Mirkovic, F. C. Stingo, and S. F. Kry. "Approaches to reducing photon dose calculation errors near metal implants". In: *Medical physics* 43.9 (2016), pp. 5117–5130.

[166] C. Reft, R. Alecu, I. J. Das, B. J. Gerbi, P. Keall, E. Lief, B. J. Mijnheer, N. Papanikolaou, C. Sibata, and J. Van Dyk. "Dosimetric considerations for patients with HIP prostheses undergoing pelvic irradiation. Report of the AAPM Radiation Therapy Committee Task Group 63". In: *Medical physics* 30.6 (2003), pp. 1162–1182.

[167] E. Wieslander and T. Knöös. "Dose perturbation in the presence of metallic implants: treatment planning system versus Monte Carlo simulations". In: *Physics in Medicine & Biology* 48.20 (2003), p. 3295.

[168] S. Spirydovich, L. Papiez, M. Langer, G. Sandison, and V. Thai. "High density dental materials and radiotherapy planning: comparison of the dose predictions using superposition algorithm and fluence map Monte Carlo method with radiochromic film measurements". In: *Radiotherapy and oncology* 81.3 (2006), pp. 309–314.

[169] O. Jäkel, C. Jacob, D. Schardt, C. P. Karger, and G. Hartmann. "Relation between carbon ion ranges and x-ray CT numbers". In: *Medical physics* 28.4 (2001), pp. 701–703.

[170] F. Ulrich-Pur, L. Adler, T. Bergauer, A. Burker, A. De Franco, G. Guidoboni, A. Hirtl, C. Irmler, S. Kaser, S. Nowak, et al. "Commissioning of low particle flux for proton beams at MedAustron". In: *Nuclear Instruments and Methods in Physics Research Section A: Accelerators, Spectrometers, Detectors and Associated Equipment* 1010 (2021), p. 165570.

[171] Ashland. *GAFCHROMIC™ DOSIMETRY MEDIA, TYPE EBT-3*. accessed September 20, 2024.

[172] J. Sorriaux, A. Kacperek, S. Rossomme, J. A. Lee, D. Bertrand, S. Vynckier, and E. Sterpin. "Evaluation of Gafchromic® EBT3 films characteristics in therapy photon, electron and proton beams". In: *Physica Medica* 29.6 (2013), pp. 599–606.

[173] S. Khachonkham, R. Dreindl, G. Heilemann, W. Lechner, H. Fuchs, H. Palmans, D. Georg, and P. Kuess. "Characteristic of EBT-XD and EBT3 radiochromic film dosimetry for photon and proton beams". In: *Physics in Medicine & Biology* 63.6 (2018), p. 065007.

[174] M. Mathot, S. Sobczak, and M.-T. Hoornaert. "Gafchromic film dosimetry: four years experience using FilmQA Pro software and Epson flatbed scanners". In: *Physica Medica* 30.8 (2014), pp. 871–877.

[175] A. A. Schoenfeld, D. Poppinga, D. Harder, K.-J. Doerner, and B. Poppe. "The artefacts of radiochromic film dosimetry with flatbed scanners and their causation by light scattering from radiation-induced polymers". In: *Physics in Medicine & Biology* 59.13 (2014), p. 3575.

[176] D. Lewis and M. F. Chan. "Correcting lateral response artifacts from flatbed scanners for radiochromic film dosimetry". In: *Medical physics* 42.1 (2015), pp. 416–429.

[177] L. Van Battum, H. Huizenga, R. Verdaasdonk, and S. Heukelom. "How flatbed scanners upset accurate film dosimetry". In: *Physics in Medicine & Biology* 61.2 (2015), p. 625.

[178] PTW. *User Manual Ionization Chambers Type 31010, 31011, 31012, Type 31013 from serial number 1000 (Semi-flexible Chambers)*. 2013.

[179] P. Wesolowska, D. Georg, W. Lechner, P. Kazantsev, T. Bokulic, A. C. Tedgren, E. Adolfsson, A. M. Campos, V. G. L. Alves, L. Suming, et al. "Testing the methodology for a dosimetric end-to-end audit of IMRT/VMAT: results of IAEA multicentre and national studies". In: *Acta Oncologica* 58.12 (2019), pp. 1731–1739.

[180] W. Lechner, B. Knäusl, J. Brunner, D. Georg, and P. Kuess. "A phantom for 2D dose measurements in the vicinity of metal implants for photon and proton beams". In: *Frontiers in Physics* 12 (2024), p. 1433208.

[181] A. Medical. *VERTAUX 5.5mm Pedicle Screws System. In Surgical Technique.* accessed October 16, 2024.

[182] J. F. P. Azorin, L. I. R. Garcia, D. M. Ozcoidi, and J. F. Almansa. "Polarized dosimetry method for Gafchromic EBT3". In: *Physica Medica* 32.8 (2016), pp. 972–980.

[183] B. Arjomandy, R. Tailor, A. Anand, N. Sahoo, M. Gillin, K. Prado, and M. Vicic. "Energy dependence and dose response of Gafchromic EBT2 film over a wide range of photon, electron, and proton beam energies". In: *Medical physics* 37.5 (2010), pp. 1942–1947.

[184] S. Devic. "Radiochromic film dosimetry: past, present, and future". In: *Physica medica* 27.3 (2011), pp. 122–134.

[185] S. Devic, J. Seuntjens, G. Hegyi, E. B. Podgorsak, C. G. Soares, A. S. Kirov, I. Ali, J. F. Williamson, and A. Elizondo. "Dosimetric properties of improved GafChromic films for seven different digitizers". In: *Medical physics* 31.9 (2004), pp. 2392–2401.

[186] S. Devic, N. Tomic, C. G. Soares, and E. B. Podgorsak. "Optimizing the dynamic range extension of a radiochromic film dosimetry system". In: *Medical physics* 36.2 (2009), pp. 429–437.

[187] E. GafchromicVR. "Self-developing film for radiotherapy dosimetry". In: *ISP White Paper* (2010).

[188] E. Wilcox, G. Daskalov, and L. Nedialkova. "Comparison of the epson expression 1680 flatbed and the Vidar VXR-16 Dosimetry PRO™ film scanners for use in IMRT dosimetry using gafchromic and radiographic film". In: *Medical physics* 34.1 (2007), pp. 41–48.

[189] *ISP presentation*. URL: `www.FilmQAPro.com/Micke_Lewis_Yu_Triple_Channel_Technique_201001.pdf`.

[190] D. Lewis, A. Micke, X. Yu, and M. F. Chan. "An efficient protocol for radiochromic film dosimetry combining calibration and measurement in a single scan". In: *Medical physics* 39.10 (2012), pp. 6339–6350.

[191] Ashland. *Efficient Protocols for Accurate Radiochromic Film Calibration and Dosimetry*. accessed September 25, 2024.

[192] L. Zhao and I. J. Das. "Gafchromic EBT film dosimetry in proton beams". In: *Physics in medicine & biology* 55.10 (2010), N291.

[193] A. Piermattei, R. Miceli, L. Azario, A. Fidanzio, S. Delle Canne, C. De Angelis, S. Onori, M. Pacilio, E. Petetti, L. Raffaele, et al. "Radiochromic film dosimetry of a low energy proton beam". In: *Medical physics* 27.7 (2000), pp. 1655–1660.

[194] S. M. Vatnitsky. "Radiochromic film dosimetry for clinical proton beams". In: *Applied radiation and isotopes* 48.5 (1997), pp. 643–651.

[195] S. Devic, J. Seuntjens, E. Sham, E. B. Podgorsak, C. R. Schmidtlein, A. S. Kirov, and C. G. Soares. "Precise radiochromic film dosimetry using a flat-bed document scanner". In: *Medical physics* 32.7Part1 (2005), pp. 2245–2253.

[196] M. Fuss, E. Sturtewagen, C. De Wagter, and D. Georg. "Dosimetric characterization of GafChromic EBT film and its implication on film dosimetry quality assurance". In: *Physics in Medicine & Biology* 52.14 (2007), p. 4211.

[197] R. Dreindl, D. Georg, and M. Stock. "Radiochromic film dosimetry: considerations on precision and accuracy for EBT2 and EBT3 type films". In: *Zeitschrift für Medizinische Physik* 24.2 (2014), pp. 153–163.

[198] D. A. Low, W. B. Harms, S. Mutic, and J. A. Purdy. "A technique for the quantitative evaluation of dose distributions". In: *Medical physics* 25.5 (1998), pp. 656–661.

[199] E. Y. L. Marroquin, J. A. Herrera Gonzalez, M. A. Camacho Lopez, J. E. V. Barajas, and O. A. García-Garduño. "Evaluation of the uncertainty in an EBT3 film dosimetry system utilizing net optical density". In: *Journal of applied clinical medical physics* 17.5 (2016), pp. 466–481.

[200] S. Aldelaijan and S. Devic. "Comparison of dose response functions for EBT3 model GafChromic™ film dosimetry system". In: *Physica Medica* 49 (2018), pp. 112–118.

[201] B. Ferreira, M. Lopes, and M. Capela. "Evaluation of an Epson flatbed scanner to read Gafchromic EBT films for radiation dosimetry". In: *Physics in Medicine & Biology* 54.4 (2009), p. 1073.

[202] B. D. Lynch, J. Kozelka, M. K. Ranade, J. G. Li, W. E. Simon, and J. F. Dempsey. "Important considerations for radiochromic film dosimetry with flatbed CCD scanners and EBT film". In: *Medical physics* 33.12 (2006), pp. 4551–4556.

[203] S. Devic, Y.-Z. Wang, N. Tomic, and E. B. Podgorsak. "Sensitivity of linear CCD array based film scanners used for film dosimetry". In: *Medical physics* 33.11 (2006), pp. 3993–3996.

[204] C. Fiandra, U. Ricardi, R. Ragona, S. Anglesio, F. Romana Giglioli, E. Calamia, and F. Lucio. "Clinical use of EBT model Gafchromic™ film in radiotherapy". In: *Medical physics* 33.11 (2006), pp. 4314–4319.

[205] L. Paelinck, W. De Neve, and C. De Wagter. "Precautions and strategies in using a commercial flatbed scanner for radiochromic film dosimetry". In: *Physics in Medicine & Biology* 52.1 (2006), p. 231.

[206] L. Menegotti, A. Delana, and A. Martignano. "Radiochromic film dosimetry with flatbed scanners: a fast and accurate method for dose calibration and uniformity correction with single film exposure". In: *Medical physics* 35.7Part1 (2008), pp. 3078–3085.

[207] M. Martišíková, B. Ackermann, S. Klemm, and O. Jäkel. "Use of Gafchromic® EBT films in heavy ion therapy". In: *Nuclear Instruments and Methods in Physics Research Section A: Accelerators, Spectrometers, Detectors and Associated Equipment* 591.1 (2008), pp. 171–173.

[208] L. Van Battum, D. Hoffmans, H. Piersma, and S. Heukelom. "Accurate dosimetry with GafChromic™ EBT film of a photon beam in water: what level is achievable?" In: *Medical physics* 35.2 (2008), pp. 704–716.

[209] S. Saur and J. Frengen. "GafChromic EBT film dosimetry with flatbed CCD scanner: a novel background correction method and full dose uncertainty analysis". In: *Medical physics* 35.7Part1 (2008), pp. 3094–3101.

[210] T. Kamomae, Y. Itoh, K. Okudaira, T. Nakaya, M. Tomida, Y. Miyake, H. Oguchi, T. Shiinoki, M. Kawamura, N. Yamamoto, et al. "Dosimetric impact of dental metallic crown on intensity-modulated radiotherapy and volumetric-modulated arc therapy for head and neck cancer". In: *Journal of applied clinical medical physics* 17.1 (2016), pp. 234–245.

[211] J. Ojala, M. Kapanen, P. Sipilä, S. Hyödynmaa, and M. Pitkänen. "The accuracy of Acuros XB algorithm for radiation beams traversing a metallic hip implant—comparison with measurements and Monte Carlo calculations". In: *Journal of applied clinical medical physics* 15.5 (2014), pp. 162–176.

[212] T. R. S. N. 3. International Atomic Energy Agency (IAEA). *Absorbed Dose Determination in External Beam Radiotherapy*. `https://www-pub.iaea.org/MTCD/Publications/PDF/p15048-DOC-010-398-Rev1_web.pdf`. [Accessed 24-01-2025]. 2024.

[213] I. J. Das, G. X. Ding, and A. Ahnesjö. "Small fields: nonequilibrium radiation dosimetry". In: *Medical physics* 35.1 (2008), pp. 206–215.

[214] A. Mesbahi. "The effect of electronic disequilibrium on the received dose by lung in small fields with photon beams: Measurements and Monte Carlo study". In: (2008).

[215] H. Bagheri, A. Soleimani, N. Gharehaghaji, A. Mesbahi, F. Manouchehri, B. Shekarchi, B. Dormanesh, and H. A. Dadgar. "An overview on small-field dosimetry in photon beam radiotherapy: Developments and challenges". In: *Journal of cancer research and therapeutics* 13.2 (2017), pp. 175–185.

[216] Y. Jia, L. Zhao, C.-W. Cheng, M. W. McDonald, and I. J. Das. "Dose perturbation effect of metallic spinal implants in proton beam therapy". In: *Journal of applied clinical medical physics* 16.5 (2015), pp. 333–343.

[217] F. Verhaegen and H. Palmans. "Secondary electron fluence perturbation by high-Z interfaces in clinical proton beams: a Monte Carlo study". In: *Physics in Medicine & Biology* 44.1 (1999), p. 167.

[218] H. Lin, X. Ding, L. Yin, H. Zhai, H. Liu, A. Kassaee, C. Hill-Kayser, R. Lustig, J. McDonough, and S. Both. "The effects of titanium mesh on passive-scattering proton dose". In: *Physics in Medicine & Biology* 59.10 (2014), N81.

[219] C. Oancea, A. Luu, I. Ambrožová, G. Mytsin, V. Vondráček, and M. Davídková. "Perturbations of radiation field caused by titanium dental implants in pencil proton beam therapy". In: *Physics in Medicine & Biology* 63.21 (2018), p. 215020.

[220] A. Niroomand-Rad, S.-T. Chiu-Tsao, M. P. Grams, D. F. Lewis, C. G. Soares, L. J. Van Battum, I. J. Das, S. Trichter, M. W. Kissick, G. Massillon-JL, et al. "Report of AAPM task group 235 radiochromic film dosimetry: an update to TG-55". In: *Medical physics* 47.12 (2020), pp. 5986–6025.

[221] A. F. Resch, P. D. Heyes, H. Fuchs, N. Bassler, D. Georg, and H. Palmans. "Dose- rather than fluence-averaged LET should be used as a single-parameter descriptor of proton beam quality for radiochromic film dosimetry". In: *Medical Physics* 47.5 (2020), pp. 2289–2299.

[222] P. Wang, F. T. O'Grady, M. Janson, D. Kim, K. S. Choe, M. Grayden, C. K. Bamberger, and J. Fan. "The impact of the titanium cranial hardware in proton single-field uniform dose plans". In: *Journal of Applied Clinical Medical Physics* (2024), e14374.